DISSERTATION

MICROFLUIDICS FOR ENVIRONMENTAL ANALYSIS

Submitted by

Chase T. Gerold

Department of Chemistry

In partial fulfillment of the requirements

For the Degree of Doctor of Philosophy

Colorado State University

Fort Collins, Colorado

Summer 2018

Doctoral Committee:

Advisor: Charles S. Henry

Amber Krummel
Nancy Levinger
Richard Finke
David Dandy

ABSTRACT

MICROFLUIDICS FOR ENVIRONMENTAL ANALYSIS

During my graduate dissertation work I designed and utilized microfluidic devices to study, model, and assess environmental systems. Investigation of environmental systems is important for areas of industry, agriculture, and human health. While effective and well-established, traditional methods to perform environmental assessment typically involve instrumentation that is expensive and has limited portability. Because of this, analysis of environmental systems can have considerable financial burden and be limited to laboratory settings. To overcome the limitations of traditional methods researchers have turned to microfluidic devices to perform environmental analyses. Microfluidics function as a versatile, inexpensive, and rapidly prototyped analytical tool that can achieve analysis in field setting with limited infrastructure; furthermore, microfluidic devices can also be used to study fundamental chemistry or model complex environmental systems. Given the advantages of microfluidic devices, the research presented herein was accomplished using this alternative to traditional instrumentation. The research projects described in this dissertation involve: 1) the study of fundamental chemistry associated with surfactant surface fouling facilitated by divalent metal cations; 2) the creation of a microfluidic device to study fluid interactions within an oil reservoir; and 3) the fabrication of a paper-based microfluidic to selectively quantify K^+ in complex samples.

The first research topic discussed involves observation of dynamic evidence that supports the hypothesized cation bridging phenomenon. Experimental results were acquired by pairing traditional microfluidics with the current monitoring method to observe relative changes to a charged surface's zeta potential. Divalent metal cations were found to increase surfactant adsorption, and cations of increasing charge density were found to have a greater effect on surface charge. Analysis of the experimental data further supports theoretical cation bridging models and expands on knowledge relating to the mechanism by which surfactant adsorption occurs. This work was published in the ACS journal *Langmuir* (**2018**, *34* (4), pp 1550–1556).

The second project discussed herein focuses on the development of the microfluidic Flow On Rock Device (FORD) that was designed to study fluid interactions within complex media. The FORD was designed to be an alternative to existing fluid modeling methods and microfluidic devices that test oil recovery strategies. Fabrication of the FORD was accomplished by incorporating real reservoir rock core samples into the device. The novelty of this device is due to the simplicity and accuracy by which the physical and chemical characteristics are represented. This project has been accepted for publication pending minor revisions in *Microfluidics and Nanofluidics*.

The final project discussed the creation of the first non-electrochemical microfluidic paper-based analytical device (μPAD) capable of quantitatively measuring alkali or alkaline earth metals using K^+ as a model analyte. This device was fabricated by combining distance-based analytical quantification in μPADs with optode nanosensors. Experimental results were obtained using the naked eye without the requirement of a power source or external hardware. The resulting distance-based

μPAD showed high selectivity and the capacity to quantify K^+ in real undiluted human serum samples. This work has been published in the ACS journal *Analytical Chemistry* (**2018**, *90* (7), pp 4894–4900).

The research projects briefly described above and thoroughly discussed later within this dissertation were made possible by the utilization of microfluidic devices. These projects investigated various aspects of environmental chemistry without the use of traditional instrumentation or methods. The experimental results that were obtained further the fundamental understanding of surfactant adsorption, provide an inexpensive and accurate model to observe fluid interactions within reservoir rock material, and allow for the selective quantification of K^+ in a paper-based device without the use of a power source. The funding for each of these projects was supplied by BP plc and Global Good, as is mentioned accordingly within this dissertation.

ACKNOWLEDGMENTS

First, I would like to thank my advisor Dr. Charles “Chuck” Henry for his critical role in my graduate career. His scientific insight, perspective on life, and unwavering patience are largely responsible for my academic success in graduate school. Not only is he an outstanding scientist and boss, but also an incredible person. Under his mentorship, I became a better scientist while being reminded that I am also a human being; he instilled in me that science should be a part of life, not all consuming. Chuck’s intellect and humanity made my graduate education as pleasant as it could possible be, and for that I owe him immensely.

Secondly, I would like to express my gratitude towards my fellow Henry group members who have shared their advice, wisdom, and friendship that has helped me get to this point in my graduate career. I would like to specifically thank Dr. Scott Noblitt for his contribution to my research and for the quantity of time he spent answering my many questions. I would also like to thank Dr. Jaclyn Adkins for her insightfulness, ability to quell my many instances of anxiety, and for her nurturing persona. It would be a mistake to not also thank Kate Berg who kept the laboratory running smoothly as the unofficial laboratory manager, and also who possesses a general wealth of information and kindness. I would also like to thank the many “temporary” members of the Henry group that have been part of my graduate career for varying quantities of time; they have helped to deepen my overall graduate school experience through their generous sharing of culture and worldly understanding.

Next, I would like to thank my family and friends who supported me throughout my academic journey. Earning my Ph.D. would have seemed much more insurmountable had it not been for the outpouring of love, support, and care packages I received when preparing for various aspects of my degree. I would like to specifically thank my Mom and Dad for their emotional support, as well as for their belief in me that I could become a first-generation Ph.D. Without you two I could not see myself getting to this point in my career; I am so incredibly lucky to have had you guys having my back. I love you both.

Finally, I would like to thank Brie Beberman for her immense role in my graduate career. She provided intellectual conversation and fresh perspective, as well as challenging me to step outside of my comfort zone and become the best version of myself, as a scientist and as a human. Furthermore, when graduate school caused turmoil in my life, she supported me and found a way to keep me pushing forward. I am truly thankful for her because I honestly think I would not have gotten to this point without her.

TABLE OF CONTENTS

CHAPTER 1. INTRODUCTION

Preface

During my graduate student research career at Colorado State University I have utilized microfluidic devices in several aspects related to the environment: investigation of fundamental chemical properties, physical modeling of complex systems, and quantification of environmentally relevant analytes. My first project involved the investigation of the fundamental surface chemistry properties of complex oil reservoir systems via traditional microfluidics. The perceived need for new analytical tools to study oil reservoir dynamics led to my second project involving the design and creation of a novel microfluidic device to study fluid dynamics in oil reservoirs where reservoir rock was incorporated into the device. Finally, the lack of portable and inexpensive analytical devices capable of quantifying alkali earth metals prompted me to develop the first microfluidic paper-based analytical device that successfully integrated optode nanosensors to quantify K^+. This later work was applied to human serum samples but is ultimately targeted at soil applications. Due to the analogous “environmental” theme but diverse application of microfluidics in my research, I have provided a brief introductory overview of relevant topics, including oil reservoir chemistry, polymeric microfluidics, and paper-based microfluidic devices.

Oil Reservoir Chemistry

To recover oil from underground reservoirs, a complex process involving “primary” and “secondary” oil recovery techniques is utilized. Primary and secondary

techniques make use of pumps to maintain pressure and to inject immiscible fluids respectively. Despite the recent technological advances in these techniques, 50–60% of the original oil in place (OOIP) remains unrecovered from mature underground reservoirs, due to physical and chemical interactions that are competing within a reservoir.[1,2] The physical interactions are the result of an underground reservoirs' porous rock structure that can contain a wide range of pore-throat sizes, shapes, distributions and connectivity.[3,4] The varying pore-throat sizes and structure exhibited by reservoirs are dependent on the geology of the siliciclastic rock that forms the reservoir.[5-7] Conventional reservoir rocks and tight-gas reservoirs, composed primarily of sandstone, contain pore-throat sizes between 2–160 μm and 0.03–2 μm respectively.[8,9] Globally, sandstone accounts for 50–60% of oil containing reservoirs.[10] The remaining 40% of reservoirs, that hold approximately 60% of the planet's oil, are formed from carbonate rocks that do not contain a well-defined range of pore-throat sizes. Carbonate reservoirs can be composed of many different sedimentary rocks from shale-like to sandstone, which gives carbonate rocks a range of pore-throat sizes from 0.005 to 150 μm.[6,8,10,11] The range of pore-throat sizes and general structure of reservoirs has a considerable effect on whether capillary or viscous forces dominate fluid flow in porous reservoirs. Competition of capillary and viscous forces during oil recovery is a fundamental component of reservoirs that governs the ability of a reservoir to produce oil and at what efficiency recovery can occur.[8,12-15]

Impact of Capillary Number on Oil Recovery

A reservoir's microporous structure is a critical component to understanding the mobilization and recovery of oil; however, the immiscible fluid-fluid and fluid-mineral interactions within a reservoir must also be considered.[16,17] Immiscible fluid-fluid interactions arise when aqueous displacement fluid is pumped underground to force the oil out of its reservoir. Fluid-mineral interactions occur when either the displacement fluid or oil interact with the surrounding reservoir rock structure. To account for these interactions and determine the domination of flow by either capillary or viscous forces, the capillary number of a reservoir system is calculated using the equation provided in Figure 1.1.[17]

$$C_N = \frac{\mu q}{\gamma \phi}$$

C_N = capillary number (dimensionless)
μ = invading phase viscosity
q = darcy flow rate (m/s)
γ = interfacial tension (IFT)
ϕ = porosity

Figure 1.1

Capillary forces dominate flow for capillary numbers (C_N) less than 1 x 10^{-5} and viscous forces dominate flow when C_N is greater than 1 x 10^{-5}.[16,17] When capillary forces dominate flow in a reservoir, portions of continuous oil ganglia are likely to become permanently immobilized in a reservoir's pore-throat space, which is termed capillary trapping.[16-19] Capillary trapping reduces the efficiency of oil recovery and is responsible for the majority of unrecoverable OOIP that remains in porous reservoirs. In a reservoir during oil recovery the dynamic viscosity of water, interstitial flow rate ($v = q / \phi$) and interfacial tension (oil-water) are ~ 2.4 x 10^{-4} Pa*s, 1 x 10^{-5} m*s^{-1} and 70 mN*m^{-1},

respectively.[16,20] Calculation of the capillary number using the previously discussed values gives a dimensionless value of 3.4×10^{-8}. Flow within a reservoir that has a capillary number of 10^{-8} is dominated by capillary forces and capillary trapping is likely to occur. Reducing capillary trapping events by having $C_N > 10^{-5}$ can increase the efficiency of oil recovery.

To achieve capillary numbers greater than 10^{-5}, the viscosity or flow rate of the displacement fluid would need to be significantly increased. Achieving displacement fluid viscosities or flow rates that would result in capillary numbers greater than 10^{-5} would require an insurmountable pressure gradient between well outlets.[16,21] Since it is improbable to increase the invading phase's viscosity and flow rate to values that would allow for flow dominated by viscous forces, and porosity is unchangeable, investigation of the equation in Figure 1.1 reveals interfacial tension to be the only significantly modifiable variable when viscous forces are concerned. Acquiring capillary numbers greater than 10^{-5} requires values of interfacial tension to be less than 0.24 mN m^{-1} if calculated using the aforementioned values; this lower limit of interfacial tension needs to be reached for preferable viscous force dominated flow to occur. Many oil recovery techniques use surfactants that are designed to lower interfacial tension so as to prevent conditions that would promote capillary trapping; these techniques have shown to increase the recovery of OOIP by 10–20%.[16,21-23] Although decreasing the value of interfacial tension between the oil and the displacement fluid will promote flow dominated by viscous forces, capillary trapping will still occur unless the value of interfacial tension is zero.[15-17,24,25] Alongside decreasing interfacial tension, capillary

forces that promote capillary trapping must also be addressed to optimize the percentage of OOIP recovered.

Impact of Capillary Forces on Oil Recovery

Decreasing the capillary forces that cause capillary trapping can be accomplished by modifying the wetting conditions of pore-throat surfaces in reservoirs. In oil reservoir systems, surfaces that display contact angles less than 40° are said to be “water-wet.” Equivalently, surfaces that display contact angles greater than 140° are said to be “oil-wet.” Contact angles that fall between 40–140° are used to describe wettability that is intermediate, or “mixed wet.”[17,24-26] Oil recovery from water-wet reservoirs results in relatively low OOIP recovery efficiencies and a high saturation of residual oil that permanently remains due to the capillary trapping of pores. High saturation of residual oil is caused by the injection of aqueous displacement fluid that stimulates the growth of water films on the water-wet pore-throat surfaces. Water film growth results in water bridging at the pore-throat interface that leads to undesirable “snap-off” events that occur when a portion of the oil phase ganglia is pinched by the water phase until the continuity of the oil phase is broken.[16,27] Compared to water-wet reservoirs, recovery efficiencies of OOIP from oil-wet reservoirs are generally higher.[2,15,16,25] However, a larger injection volume is required for recovery from oil-wet reservoirs because the oil film on the pore-throat surfaces leads to breakthrough of the aqueous displacement fluid occurring early on in the recovery process.[16,24] When pore-throat surfaces are oil-wet, the oil phase tends to remain continuous and the quantity of permanently trapped residual oil, due to capillary forces, is considerably less than in the

case of the water-wet reservoir.[14-16,24-26] Reservoirs that contain mixed-wet wettability afford the highest OOIP recovery efficiencies and the lowest quantity of residual oil saturation.[24,25] Under mixed-wet conditions pore-throat spaces possess both water-wet and oil-wet surfaces, which allows the oil phase to remain continuous and snap-off events are minimized as water and oil drain concurrently from the reservoir.[16,24,25] Mixed-wet pore-throat spaces provide the optimal wettability conditions for OOIP recovery and need to be controlled alongside interfacial tension to maximize efficiency during recovery.

Wettability and Ion Binding

Altering the interactions between the oil phase and pore-throat walls can control the wettability of pore-throat spaces. The four mechanisms that govern a reservoir's wettability are the: **1)** rock surface's adsorption of polar functional groups from oil, [28-30] **2)** surface precipitation of asphaltenes,[4,31-33] **3)** acid-base reactions,[34-39] and **4)** ion binding caused be brine present in the reservoir.[40-48] Of these four mechanisms, researchers have suggested that control of ion binding should be targeted since it is the most easily manipulated during oil recovery.[44] Furthermore, ion binding should be controlled since it has also been shown to dominate over the impacts of acid-base interactions, the adhesion of asphaltenes, and pH effects.[28,35,43,44,49,50]

Ion binding, or cation bridging (Fig 1.2), is likely to arise between charged sites on pore-throat surfaces and the oil's polar hydrocarbon functional groups, which is potentially facilitated by divalent or multivalent ions found in the connate water that shares the pore-throat space with oil.[26,30,32,34,40-43] Binding interactions that are likely to

happen in the presence of di/multivalent ions include oil–ion–oil, mineral–ion–mineral, and oil–ion–mineral interactions.[30,44,45] Specifically, the presence of divalent calcium ions (Ca^{2+}) in connate brine water give rise to relatively strong ion binding interactions between the oil phase and pore-throat mineral surfaces, this ion binding promotes both the oil phase's wettability and resistance to desorption (Figure 1.2). The degree to which

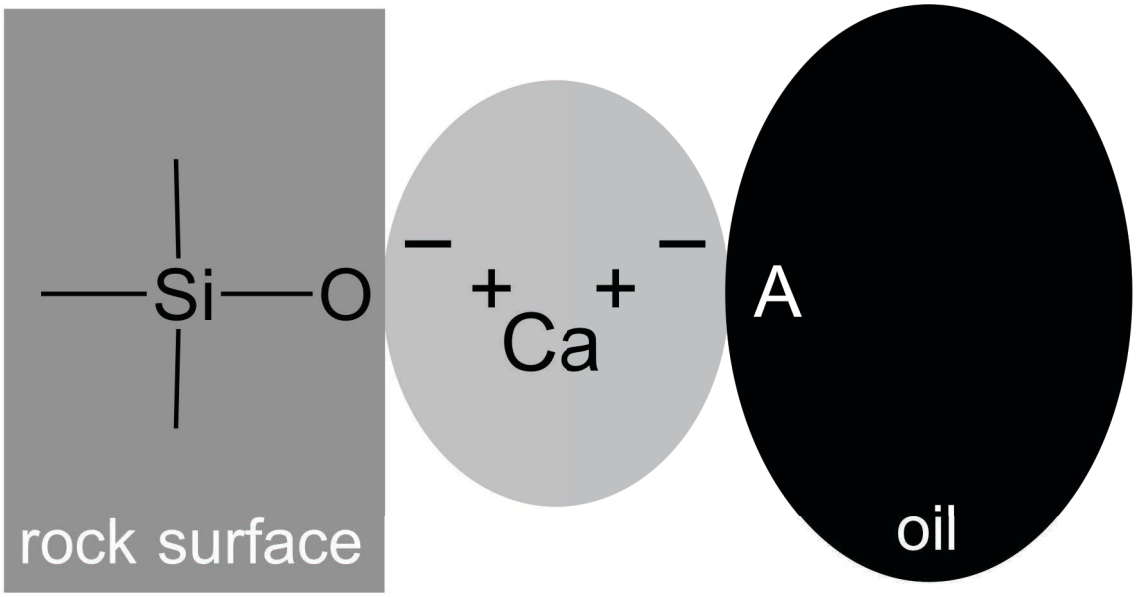

Figure 1.2. An example of ion binding between the rock surface and the oil phase. Divalent cations, prevalently Ca^{2+}, facilitate the adsorption of negatively charged polar functionalities found in the oil phase

the ions present in the connate brine affect wettability and ion binding of the oil phase is dependent on both the brine's and crude oil's composition.[46-48,51] Thus, improving the efficiency of oil recovery, by modification of pore-throat surface wettability, should be accomplished by altering ionic components found in reservoir connate water.

Brine Control to Increase Oil Recovery Efficiency

To successfully increase recovery efficiency and the quantity of recoverable OOIP, the oil industry has pursued the use of enhanced oil recovery (EOR) techniques using brine displacement fluids to affect ion binding. A commercial example of the brine solutions used in EOR is LoSal™ that has shown to increase the quantity of recoverable OOIP in some cases by 40%.[44,52] LoSal™ is a dilute brine solution that has ion concentrations that are ~30 times lower than what is found in reservoir connate water.[44] It is suspected that a lower concentration brine causes desorption of adsorbed ions on pore-throat surfaces, helping to decrease oil–ion–mineral interactions and increase oil recovery efficiency.[28,44] Although LoSal™ has been shown to increase the efficiency of oil recovery, the specific desorption mechanism that occurs between mono/divalent ions and oil's polar functional groups, that have a diverse variation in structure, is not entirely understood.

Investigating Zeta Potential

To optimize the quantity of OOIP that can be recovered from oil reservoirs, the specific interactions of ionized salts (from brine and connate water) and reservoir relevant molecules (surfactant-like species found in oil) at a charged surface must be studied; these interactions can be described by the effective surface charge. This charge is often referred to as the "zeta potential," which describes the interactive electric potential of a surface relative to the bulk solution surrounding a charged surface. Measurement and quantification of a surface's zeta potential can be used to help explain representative changes in the adsorbed molecular species. Zeta potential

measurements can consequentially correlate with the effects that occur upon the addition of metal ions and surfactants to the solution surrounding the surface. During my dissertation research, zeta potential values were measured by monitoring the mobility of the electroosmotic flow (μEOF, thoroughly defined in Chapter 2) using traditional polydimethylsiloxane (PDMS) microfluidic devices. PDMS was chosen for its well-studied properties, and chemical similarities that it shares with reservoir rock.[28,53-55] Microfluidic devices were chosen to study zeta potential for their microscale channel dimensions that are comparable to the size of pore-throat structures in oil reservoirs and for their capacity to perform μEOF studies. Reservoir relevant surfactants and cations were used to model the overall system to better understand the dynamics of the interactions and how they impacted zeta potential.

Assessing EOR Using Traditional Microfluidics

In addition to studying surface chemistry processes relevant to oil recovery, I also developed a microfluidic device that incorporated reservoir rock to help understand processes that occur in systems that are chemically and physically identical to oil reservoirs. Typically, oil reservoir processes and new EOR techniques are investigated using small-scale studies.[1,44,56-59] While valuable information has been obtained from small-scale studies, the success of specific EOR strategies is best predicted by real field studies; unfortunately, these studies come at significant financial and time costs.[56,60] An alternative to large field studies are laboratory-scale “core flooding” experiments that involve the injection of fluid into cylindrical reservoir rock samples.[58,61] When compared to field studies, laboratory-scale core flooding experiments express

reduced operational costs, increased rates at which results are obtained, and the capacity to test multiple EOR strategies. Since the reservoir rock core samples must be obtained from real oil reservoirs using specialized drilling equipment these experiments are still relatively expensive; additionally, they require long equilibration times, and necessitate specialized instrumentation for flow imaging due to the opaque nature of the rock cores. Despite the advantages of laboratory-scale core flooding experiments, if more effective EOR strategies are to be rapidly developed, then the cost and time associated with experimental studies must be reduced further. In pursuit of a more cost/time effective method to assess EOR methods, part of my graduate research career was spent developing an analytical tool based on traditional microfluidics that incorporated real reservoir rock samples.

Traditional microfluidic devices are typically categorized as fluid handling devices that contain structural geometries smaller than the millimeter scale, which have been created via molding, engraving, or extrusion. These sub-millimeter features can be fabricated using a variety of polymer-based materials: polyamide,[62] polycarbonate,[63] polyethylene,[64] polymethylmethacrylate,[65,66] polypropylene,[67] polystyrene,[68,69] polydimethylsiloxane,[70-72] and other polymer materials have been used.[73] Furthermore, many different methods can be used to create the sub-millimeter scale features in the polymer material such as hot embossing,[62] injection molding,[74] casting,[75] laser-ablation,[66] direct patterning using optical lithography[76] and stereolithography,[77] and indirect patterning using soft lithography.[73,78] Of these methods, soft lithography has become a popular method for fabricating microfluidics due to its capacity for rapid prototyping, relatively inexpensive nature, and high-resolution characteristics.[78]

Soft lithography is a collective term describing fabrication of microfluidic devices using an elastomeric stamp.[78] Most commonly the elastomeric stamp is created by depositing a sub-millimeter layer of photoactive polymer (SU-8) on a substrate (typically a Si wafer) via spin coating, covering the polymer with an opaque mask that contains translucent sub-millimeter features, then exposing the polymer to ultraviolet light that permanently crosslinks the polymer only in the areas where the mask is translucent.[78] Uncrosslinked polymer is removed by soaking the substrate in solvent leaving behind embossed features that make up the master elastomeric stamp (Figure 1.3). A portion of the microfluidic device is then fabricated by pouring a curable polymer (typically polydimethylsiloxane, PDMS) over the stamp, curing the polymer, then pealing the cured polymer off the stamp leaving behind a negative replica of the stamp's features. Next, the cured PDMS that contains sub-millimeter features, and either another piece of cured PDMS sans features or a piece of glass have their surfaces oxidized via plasma treatment. Both portions of the device are brought into conformal contact after having been sufficiently oxidized forming a permanently sealed microfluidic device (Figure 1.4). The resulting traditional microfluidics can be used to study fundamental properties of chemical systems and as an analytical tool to quantify analytes of interest.[78,79]

Although many traditional microfluidic devices are created using the soft lithography method and PDMS, microfluidic devices can be produced using a variety of different fabrication methods, materials, and can contain a varying degree of complexity. Since microfluidics exist as a diverse assortment of devices, they can be paired with a diverse assortment of analytical methods. Microfluidics have been previously paired with infrared detection,[80-84] Raman spectroscopy,[85-87] nuclear magnetic resonance

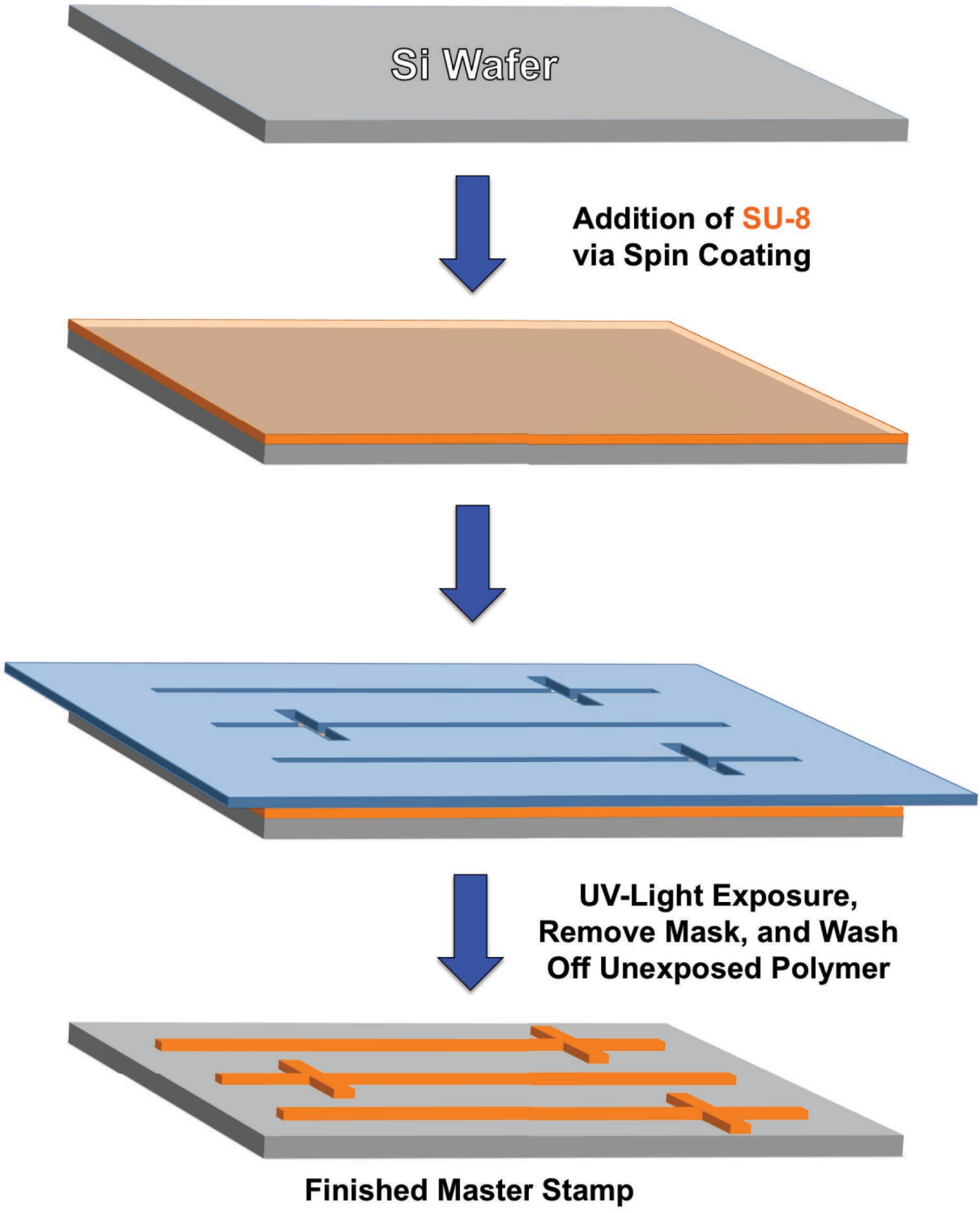

Figure 1.3. Creation of an elastomeric master stamp. Photoactive SU-8 polymer is poured on a Si wafer that is then spun at high speed to acquire a layer of polymer with desired thickness. A patterned mask is placed on the wafer/polymer, exposed to UV-light, and then washed to remove any unexposed SU-8. Embossed features are retained on the Si wafer creating the finished master stamp

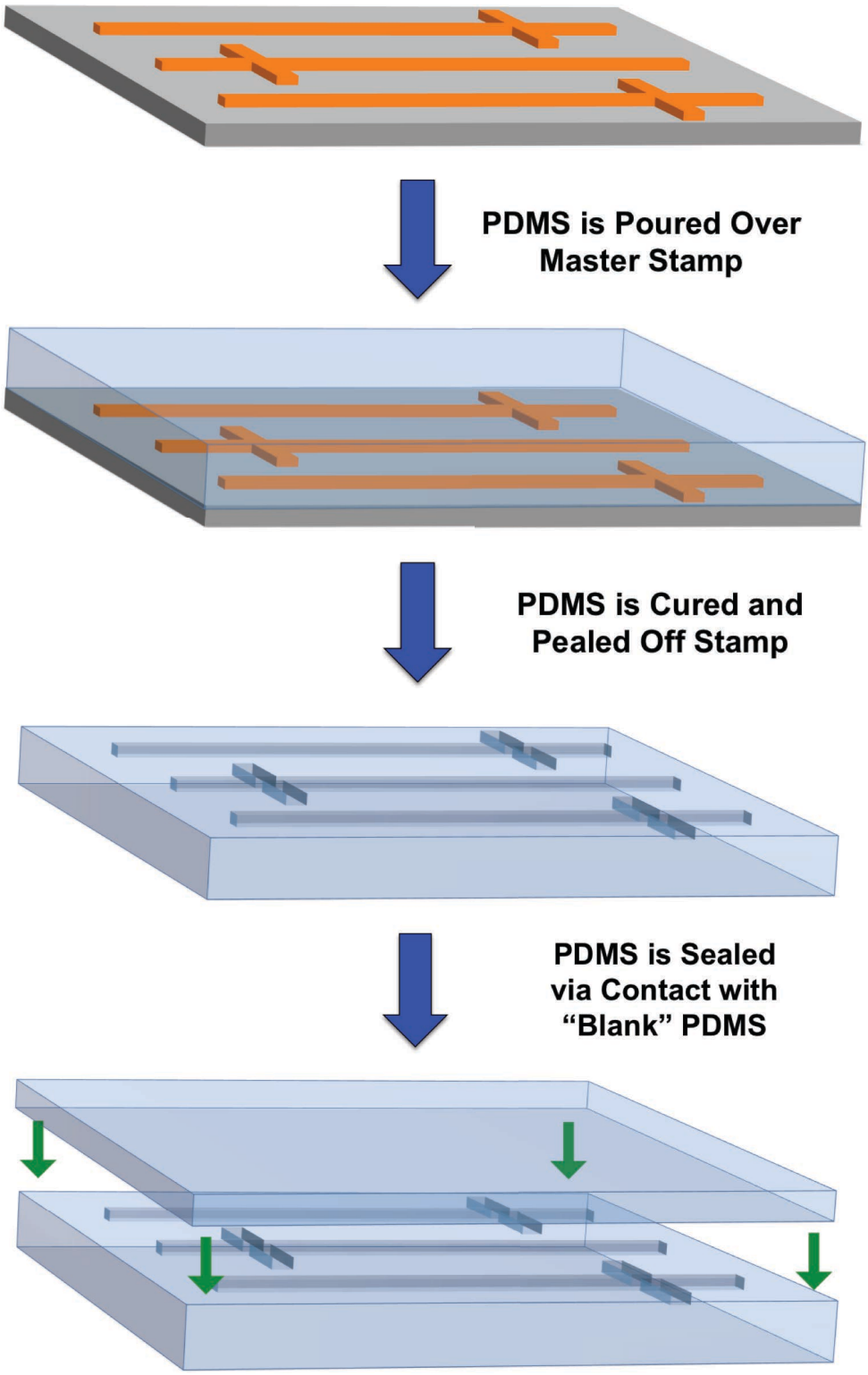

Figure 1.4. Creation of a PDMS microfluidic device. Uncured PDMS is poured on the elastomeric master stamp and cured. Cured PDMS is pealed off the stamp, oxidized via plasma treatment, and brought into conformal contact with a piece of “blank” PDMS to form a permanently sealed microfluidic device

(NMR),[88-90] surface plasmon resonance (SPR),[91-93] absorbance detection,[94-97] chemiluminescence and electrochemiluminescence detection,[98-101] fluorescence detection,[102-104] electrochemical detection,[105-110] mass spectrometry,[111-113] electrophoretic separation,[114-117] current monitoring,[118-120] and other detection methods.[121-123] Pairing of various microfluidic devices with many different analytical methods has led to the rapid exploration of environmental systems and the on-site quantification of analytes that would typically be not be able to be performed using traditional instrumentation.

While traditional microfluidics are capable of quantifying environmental analytes and modeling various systems, their inherent ability to be as sensitive or selective as their traditional counterparts is somewhat limited by their inherent design characteristics. By design, microfluidic devices are fabricated using inexpensive materials and limited usage of large technological components. To improve the sensing properties of traditional microfluidics researchers have employed analyte preconcentration,[124] nanoparticles,[125] combined UV/fluorescence detection,[102] photodiodes,[126] droplet generators,[127] low-cost printed circuit boards,[128] cooling devices,[129] and other specifically designed technologies.[130-132] Despite their intrinsic limitations, improvement to device designs and protocols has helped traditional microfluidic devices achieve limit of detections (LODs), selectivity, and physical dimensionality that are appropriate for many applications.

When trying to utilize traditional microfluidics to assess EOR methods one of the most challenging aspects of generating these devices is replicating the physical and chemical complexity found in natural rock. To recreate reservoir structures in

microfluidics researchers have employed digital scanning, computational structure generation, and devices with channels packed with granular material or mineral crystals.[14,18,133,134] Even if the structure or reservoir rock is successfully recreated the device may not be chemically representative of real reservoir samples, which limits the experimental accuracy. With aspects of traditional microfluidics and current microfluidics available for EOR research in mind, part of my graduate research career was spent developing a tabletop-scale alternative to the current core flooding method by using a traditional microfluidic device coupled with thin sections of reservoir rock samples. The resulting microfluidic device, named herein as the Flow On Rock Device (FORD), did not require that physical or chemical features be recreated since real reservoir rock samples were utilized in the device.

Microfluidic Paper-Based Analytical Devices

In my final work as a Ph.D. candidate I deviated from studies of oil recovery to develop a microfluidic device for measuring K^+ that could be applied to both human health and environmental samples. In many cases evaluation of analytes pertaining to human and environmental health must be accomplished outside the laboratory in regions exhibiting limited resources. To further increase microfluidic device portability another variety of microfluidic devices called microfluidic paper-based analytical devices (μPADs) can be employed. Much like their traditional microfluidic counterparts, μPADS process microliter scale volumes of sample solution. μPADs are primarily composed of a paper-based substrate (analytical grade filter paper) that have a hydrophobic barrier deposited on the paper. The hydrophobic barrier determines where aqueous samples

can travel in the μPAD and can be created using various methods: photolithography,[135] plotting with an analogue plotter,[136] ink jet etching,[137] plasma treatment,[138] paper cutting,[139] ink jet printing,[140] flexography printing,[141] screen printing,[142] laser treatment,[143] wax printing,[144] and others.[121,145,146] All patterning methods provide the capacity to cheaply pattern a paper substrate with the highest financial burden being ~$0.10 (for 100 cm^2, photolithography using SU-8 photoresist) down to the most inexpensive patterning technique costing ~$0.00001 (for 100 cm^2, ink jet printing using alkyl ketene dimer).[140,145,147] Patterning μPADs using the wax printing method has gained popularity since a wax printer can be purchased and used without modification to produce 100 cm^2 of devices for ~$0.01.[144] These relatively inexpensive devices are easily produced by first printing a hydrophobic design on a paper substrate (Figure 1.5.A) followed by subsequent heating of the wax design with a hotplate (Figure 1.5.B).[142] Applying heat to the patterned device causes migration of the wax through the layer of paper creating a complete hydrophobic cross section. Migration of melted wax causes the overall size of the designed features to shrink and the color of the deposited wax to appear as a lighter shade. Chemical reagents are deposited after the hydrophobic barrier is completed and the resulting device is sealed using hot lamination or adhesive tapes. It should be noted that a new wax printer (the Xerox ColorQube is commonly used in this area of research) can cost an upwards of ~$900. Despite the initial wax printer expense, wax patterning is a simple, quick, and reproducible method for mass-producing devices with sufficient resolution. These reasons have made wax printing a common method for patterning μPADs.

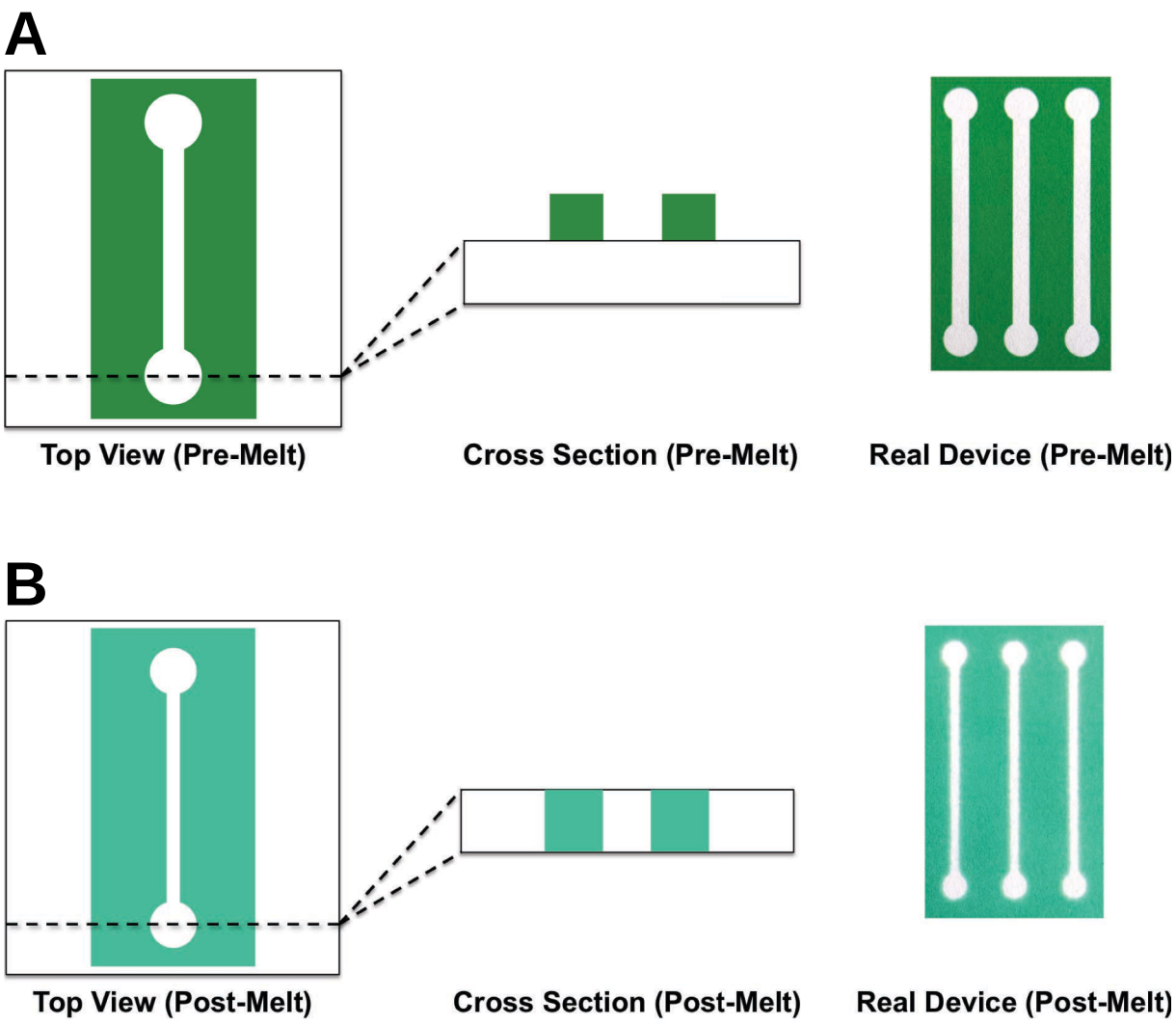

Figure 1.5. Fabrication of a wax printed μPAD. **A)** A hydrophobic wax design is deposited on a paper substrate via a specialized printer. The wax design resides atop the paper substrate. **B)** When the paper substrate is heated on a hotplate the wax design melts and migrates through the paper substrate forming a completed hydrophobic barrier. Migration of the melted wax causes shrinking of the originally deposited features and the color of the wax to appear as a different shade

Much like traditional microfluidics, μPADs can exist as a variety of different designs including components like simple spot tests, multiplexed channels, multiple layers, and various other components.[146,148] These complex geometries can be rapidly prototyped via wax printing by creating new designs in software applications that are then printed out. Besides rapid prototyping, μPADs possess additional advantages due

to the characteristics of the paper substrate and the μPAD itself. The unmodified paper substrate used to fabricate these devices is composed of hydrophilic cellulose fibers that possess the capacity to perform passive pumping: this occurs when an aqueous sample is introduced to the μPAD and flow occurs along the paper substrate due to capillary forces provided by the fibers and void space between fibers.[149,150] Passive pumping increases the portability of μPADs since no additional hardware, pump, or electrical power source is required to induce flow within the device. In addition to capillary forces, the void space between cellulose fibers can be used to store chemical reagents.[151] The effectiveness of μPADs at storing chemical reagents is largely dependent of the stability of the deposited chemical.[150,152] Passive pumping and chemical reagent storage allow μPADs to function as portable analytical tools, which are often described as a “lab-on-a-chip” due to their capacity to perform laboratory style experiments on a single device. Paper’s porous and lightweight nature also provides the ability of device layers to filter particulate matter from sample solutions and makes μPADs easy to transport. In addition to single layer μPADs, 3D multilayered devices that contain multiple layers of patterned paper substrate can be created by aligning and stacking designed layers together.[153] Multilayer devices contain separated layers, which can prevent stored chemical reagents from prematurely reacting, and pretreatment of sample solutions to occur before arriving in test regions.[154] Furthermore, μPADs are also relatively disposable due to the non-hazardous materials required to make the physical device, overall inexpensive fabrication cost, reduced quantity of deposited chemical reagents, and minimal sample volume required to perform experiments.[155] The

aspects of μPADs described above are what make these devices attractive for quantifying analyte species in environmental settings where resources are limited.

Akin to their traditional microfluidic cousins, various detection methods can be paired with μPADs for quantifying specific analytes. These methods include chemiluminescence,[156,157] electrochemiluminescence,[158] fluorescence,[159] surface-enhanced Raman spectroscopy,[160] separation,[161] preconcentration,[162] colorimetric,[163,164] and electrochemical techniques.[146,165,166] The latter two methods, colorimetric and electrochemical, are found most commonly in the literature. Although both electrochemical and colorimetric methods are often employed, colorimetric methods are preferred when designing μPADs to perform measurements in resource limited regions.

Colorimetric methods rely on a chemical color change that can be qualitatively interpreted using the naked-eye; thus, no additional power source or hardware is required to perform analysis unlike many quantitative methods (including electrochemical quantification). The colorimetric based μPADs that function the most qualitatively are colorimetric spot tests, these tests are simply fabricated by depositing sensing reagents on a paper substrate. Spot tests can be a variety of sizes and are designed to be a simple, usually circular, paper region surrounded by a hydrophobic barrier. Colorimetric spot tests are used by pipetting a controlled sample volume onto the top of the test spot where it will be contained by the hydrophobic barrier and hydrophobic material used to seal the back of the spot; packaging tape is commonly used to seal the back of wax printed devices. A color change will occur as sample analyte reacts with the stored sensing reagents found in the test spot. Increasing the concentration of analyte species found in sample solutions causes an increase in the

color change that occurs when a sample solution in introduced. In its most basic form, spot tests for specific analytes can be assessed by a simple “yes or no” depending on if a color change occurs or not.[167] Additionally, colorimetric spot tests can be qualitatively analyzed by comparing completed spot tests to color-coded concentration keys, which is analogous to the functionality of pH test strips.[168] Analysis using the naked eye is advantageous from a simplicity standpoint but observing the quality of color change without quantitative methodology restrictions the LOD. If more quantitative analysis is required, test spots can be digitally photographed and evaluated using image processing software to analyze the color change of completed tests. Digital analysis of the colorimetric tests increases analytical sensitivity and can decrease the observed LOD.[169-171] Calibration curves can be obtained from the digitally processed colorimetric data and used to determine the concentration of analyte in sample solutions. These qualitative and quantitative spot test methods have been used to determine the presence of illicit drugs,[172] explosive material residue,[173] microorganisms,[174,175] heavy metals,[176] and other specific analytes.[171] The wide variety of analytes and advantageous characteristics of colorimetric μPAD spot tests make them a strong candidate for use in resource limited regions but the constrained LOD is still a considerable disadvantage. While quantitative digital analysis improves the LOD, analytical techniques requiring additional infrastructure and power sources become problematic in resource limited regions. Improvement of colorimetric μPAD’s LOD without additional infrastructure has recently been made possible by applying colorimetric chemistry to distance-based microfluidic devices.[164,177]

Much like colorimetric spot tests, distance-based μPADs rely on a color change produced from a chemical reaction between sensing reagents and analyte species. Due to their functionality and appearance to that of thermometers, these distance-based μPADs are often referred to as "chemometers." Instead of analyzing changes to the quality of the color, like in colorimetric spot tests, the "distance" of color change along a paper-based microfluidic channel is observed for distance-based μPADs (Figure 1.6).[164,177,178] When an aqueous sample is introduced to the distance-based μPAD

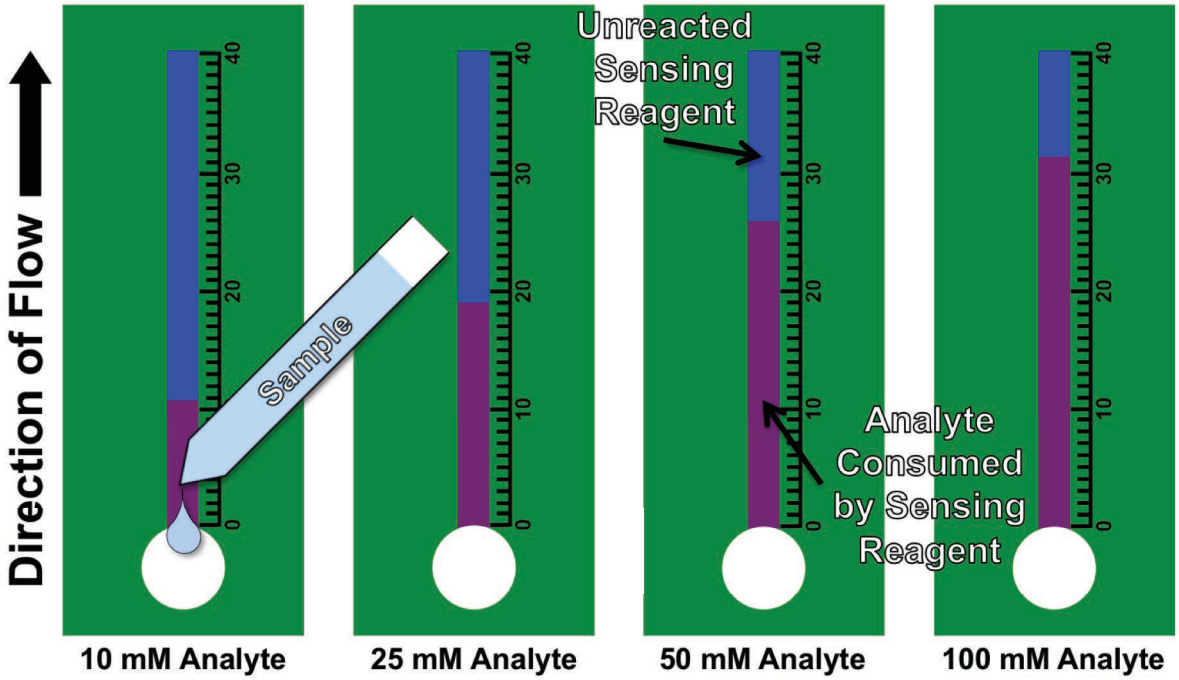

Figure 1.6. Simulation of distance-based μPADs tested with samples containing different concentrations of analyte. Samples are added to an inlet on the device. Sample will flow away from the inlet and the device's channel will change color from blue (unreacted sensing reagent) to reddish purple (sensing reagent that has reacted with the analyte) as analyte is consumed. Actual experimental color change can vary depending on the sensing reagents used. Increasing the concentration of analyte in sample solutions causes the length of the color change to increase. On-device rulers can be used to determine the length of the color change (typically mm scale)

capillary forces cause the sample to be passively pumped along the microfluidic channel. As sample solution is wicked along the device's paper channel the sensing

reagents previously deposited on the μPAD consume the analyte. The μPAD channel will change color where sensing reagents have reacted with the analyte, color change will radiate away from the sample inlet in the direction of flow. When the analyte is no longer accessible by the sensing reagents, the sample solution will continue to be wicked along the μPAD channel despite the lack of additional color change. The length or “distance” of the portion of the channel that has changed color can be measured to determine analyte concentration. Longer lengths of color change correlate to greater concentrations of analyte present in sample solutions. A collection of known sample analyte concentrations can be analyzed using replicated distance-based devices to acquire a calibration curve. With simplicity in mind, rulers can be printed parallel to the μPADs experimental channel for the end user to use to determine the distance of the color change. These paper-based analytical devices have been previously used to quantify metals,[164,178,179] small molecules,[164,180,181] proteins,[182,183] and other analytes.[177] The ability to perform relatively sensitive and quantitative measurements without the use of additional hardware, software, infrastructure, or off-device analysis provides motivation to researchers to further the development of distance-based μPADs.

Although traditional microfluidics and μPADs exhibit desirable characteristics like increased portability, chemical reagent storage, reduced financial cost, and the ability to be rapidly prototyped, they do display decreased LODs when compared to their traditional instrumental counterparts. If microfluidics are to be used for investigating environmental systems or quantifying specific analytes in complex environmental samples then the LOD of these devices must be assessed. Distance-based μPADs have been shown to detect Ni, Cu, and Fe in samples down to the 10^{-7} M range[179] while

methods using Inductively Coupled Plasma Mass Spectrometry (ICP-MS) are able to identify those same metals in the 10^{-11} M range.[184] When compared to distance-based μPADs, the four orders of magnitude lower LOD for LCP-MS shows a clear advantage in favor of the traditional method at quantifying trace amounts of metals in sample solutions. According to the Environmental Protection Agency (EPA), the acceptable concentrations of Ni, Cu, and Fe in drinking water are in the range of 10^{-6}, 10^{-5}, and 10^{-6} M respectively.[185-187] Although ICP-MS has an advantage over distance-based μPADs at quantifying amounts of trace metals, if the assessment of potable drinking water is the primary concern, the LODs expressed by distance-based μPADs are entirely acceptable.

While the LOD of colorimetric/distance-based μPADs is situationally acceptable, the inherent complexity of environmental samples suggests that the selectivity of μPADs is also an essential characteristic to gauge if these devices are to be employed for environmental analysis. To increase the selectivity of μPADs for specific analytes, researchers have considered eliminating or masking interfering species via sample pretreatment regions.[179,188-192] These pretreatment regions can bind interfering species, adjust characteristics of sample solutions like pH, or reductively alter sample species to adjust experimental selectivity. Furthermore, portions of devices can make use of the filtration properties of the paper substrate to physically filter out particulate matter if it is suspected to experimentally interfere.[191] The modifiable selectivity of μPADs along with their inexpensive nature, portability, and appropriate LODs make these devices highly effective for analytical measurements outside of a laboratory setting.

Summary of Ph.D. Candidate Research

My research career at CSU, under the advisement of Dr. Charles Henry, was associated with using microfluidic devices to investigate different aspects of environmental systems. My first project involved exploration of the fundamental surface chemistry related to oil recovery. The surface chemistry I was specifically interested in was the cation bridging phenomenon that had been observed by previous researchers but not entirely understood due to the lack of dynamic experimental evidence. By monitoring the μEOF using traditional PDMS microfluidic devices, I was able to observe the varying dynamic interactions that occurred at a charged surface when a like-surfactant species was introduced in the presence of mono/divalent metal ions. This research provided the scientific community with a better understanding of the cation bridging mechanisms governing oil recovery and surface fouling mediated by surfactants.

My second research project involved the design and fabrication of a traditional microfluidic device to act as a possible alternative to existing laboratory scale core flooding technology. While microfluidic devices capable of performing core flooding experiments do exist, their capacity to accurately replicate the complex physical and chemical characteristics of reservoirs is debatable. Instead of trying to replicate the reservoir properties in a microfluidic device, I fabricated the Flow On Rock Device (FORD) that incorporated actual reservoir rock samples. Fabrication of the FORD circumvented the requirement of having to recreate physical structures and allowed inclusion of the naturally occurring chemical properties found within the samples. This research intended to promote rapid prototyping of EOR strategies by allowing core

flooding experiments to occur more frequently at significantly reduced financial and resource cost.

Finally, my third research project deviated from chemistry related to oil recovery and involved development of a μPAD to quantify K^+ in complex environmental samples. Before my research was published there was a complete lack of any non-electrochemical method for quantifying alkali or alkaline earth metals using paper-based devices. This problem was likely a product of the unavailability of aqueous soluble sensing reagents. To thwart the lipophilicity of available sensing reagents, I employed optode nanosensors that were then coupled with a distance-based detection mode in μPADs. The resulting μPAD allowed sensitive and highly selective quantification of K^+ in real undiluted human serum samples. While the device was originally intended to be used for environmental sampling, the successful quantitation of K^+ in complex human serum suggested that the device would also be capable of processing environmental samples where selectivity is also pertinent.

REFERENCES

1. Ali, S. M. F.; Thomas, S. *J. Can. Pet. Technol.* **2000**, *39*, 7–11.

2. Alvarado, V.; Manrique, E. *Energies* **2010**, *3*, 1529–1575.

3. Cense, A. W. B., S. **2009**.

4. Mullins, O. C.; Zuo, J. Y.; Wang, K.; Hammond, P. S.; De Santos, R.; Dumont, H.; Mishra, V. K.; Chen, L.; Pomerantz, A. E.; Dong, C. L.; Elshahawf, H.; Seifert, D. J. *Petrophys.* **2014**, *55*, 96–112.

5. Fisher, Q. J. K., R.J. *Mar. Pet. Geol.* **2001**, *18*, 1063–1081.

6. Lucia, F. J. *Carbonate Reservoir Characterization*; Springer, 1999.

7. Morsea, J. W. A., R.S. *Earth-Sci. Rev.* **2002**, *58*, 51–84.

8. Nelson, P. H. *American Association of Petroleum Geologists Bulletin* **2009**, *93*, 329-340.

9. Elsaeh, A. E., Ramdzani, I.A.B.A. *Eur. Sci. J* **2014**, *10*, 102–113.

10. Bjørlykke, K. *Petroleum geoscience : from sedimentary environments to rock physics*; Berlin ; London : Springer, [2010] ©2010, 2010.

11. Carbonate Reservoirs. http://www.slb.com/services/technical_challenges/carbonates.aspx (accessed 4/7/16).

12. Gao, H.; Li, T.; Yang, L. *Journal of Petroleum Exploration and Production Technology* **2015**, 1-10.

13. Nobakht, M.; Moghadam, S.; Gu, Y. *Energy Fuels* **2007**, *21*, 3469–3476.

14. Zhang, C.; Oostrom, M.; Wietsma, T. W.; Grate, J. W.; Warner, M. G. *Energy Fuels* **2011**, *25*, 3493–3505.

15. Terry, R. E. In *Encyclopedia of Physical Science and Technology*; Academic Press: New York, 2001, pp 503–518.

16. Muggeridge, A.; Cockin, A.; Webb, K.; Frampton, H.; Collins, I.; Moulds, T.; Salino, P. *Philos Trans A Math Phys Eng Sci* **2014**, *372*, 20120320.

17. Melrose, J. C. *J. Can. Pet. Technol.* **2013**, *13*.

18. Gunda, N. S.; Bera, B.; Karadimitriou, N. K.; Mitra, S. K.; Hassanizadeh, S. M. *Lab Chip* **2011**, *11*, 3785–3792.

19. Zhou, D. S., E.H. *Transport in Porous Media* **1993**, *11*, 1–16.

20. Gong, B.; Liang, H.; Xin, S.; Li, K. In *Proceedings of 36th Workshop on Geothermal Reservoir Engineering, Stanford University, Stanford*, 2011.

21. EMEGWALU, C. C. *Norwegian University of Science and Technology* **2009**.

22. Badal, M. Y.; Wong, M.; Chiem, N.; Salimi-Moosavi, H.; Harrison, D. J. *J. Chromatogr. A.* **2002**, *947*, 277-286.

23. Kiani, M.; Kazemi, H.; Ozkan, E.; Wu, Y.-S. In *SPE Annual Technical Conference and Exhibition*; Society of Petroleum Engineers: Denver, CO, 2011.

24. Anderson, W. G. *Society of Petroleum Engineers* **1987**, *39*, 1605-1622.

25. Morrow, N. R. *Journal of Petroleum Technology* **2013**, *42*, 1476-1484.

26. Abdallah, W.; Buckley, J. S.; Carnegie, A.; Edwards, J.; Herold, B.; Fordham, E.; Graue, A.; Habashy, T.; Seleznev, N.; Signer, C.; Hussain, H.; Montaron, B.; Ziauddin, M. *Oilfield Rev.* **2007**, *19*, 44–63.

27. Roof, J. G. *Society of Petroleum Engineers* **1970**, *10*, 85-&.

28. Austad, T.; Rezaeidoust, A.; Puntervold, T.; *Soc. Pet. Eng. J.*, 2010.

29. Hilner, E.; Andersson, M. P.; Hassenkam, T.; Matthiesen, J.; Salino, P. A.; Stipp, S. L. S. *Sci. Rep.* **2015**, *5*, 9933.

30. Buckley, J. S.; Liu, Y. *Journal of Petroleum Science and Engineering* **1998**, *20*, 155-160.

31. Buckley, J. S.; Liu, Y.; Xie, X.; Morrow, N. R. *SPE journal* **1997**, *2*, 107-119.

32. Drummond, C.; Israelachvili, J. *Journal of Petroleum Science and Engineering* **2004**, *45*, 61-81.

33. Buckley, J. *Revue de l'Institut Français du Pétrole* **1998**, *53*, 303-312.

34. Anderson, W. G. *Society of Petroleum Engineers* **1986**, *38*, 1125-1144.

35. Culec, L. E.; Society of Petroleum Engineers, 1975.

36. Culec, L. **1977**, *16*.

37. Poteau, S.; Argillier, J.-F.; Langevin, D.; Pincet, F.; Perez, E. *Energy Fuels* **2005**, *19*, 1337-1341.

38. Daaou, M.; Bendedouch, D. *Journal of Saudi Chemical Society* **2012**, *16*, 333-337.

39. Eliseeva, O.; Besseling, N.; Koopal, L.; Stuart, C. *Croat. Chem. Acta* **2007**, *80*, 429-438.

40. Salathiel, R. A. *Journal of Petroleum Technology* **1972**, *25*, 1216-1224.

41. Smith, J. T.; Cobb, W. M.; Office, P. T. T. C. M. *Water Flooding*; Midwest Office of the Petroleum Technology Transfer Council, 1997.

42. Craig, F. F. *The reservoir engineering aspects of waterflooding*; H.L. Doherty Memorial Fund of AIME: New York, 1971.

43. Denekas, M. O.; Mattax, C. C.; Davis, G. T.; Society of Petroleum Engineers, 1959.

44. Lager, A.; Webb, K. J.; Collins, I. R. *Soc. Pet. Eng. J.* **2008**.

45. Song, W.; Kovscek, A. R. *Lab Chip* **2015**, *15*, 3314-3325.

46. Jadhunandan, P. P. *Effects of Brine Composition, Crude Oil, and Aging Conditions on Wettability and Oil Recovery*; Department of Petroleum Engineering, New Mexico Institute of Mining & Technology, 1990.

47. Bagci, S.; Kok, M. V.; Turksoy, U. *Pet. Sci. Technol.* **2001**, *19*, 359-372.

48. Yildiz, H. O.; Morrow, N. R. *Journal of Petroleum Science and Engineering* **1996**, *14*, 159-168.

49. Buckley, J.; Morrow, N. *Physical chemistry of colloids and interfaces in oil production* **1992**, 39-45.

50. Buckley, J. S.; Takamura, K.; Morrow, N. R. **1989**, *4*.

51. Enge, I. B. **2014**.

52. Zekri, A. A.-A., Z. *International Journal of Petroleum and Petrochemical Engineering* **2015**, *1*, 1-11.

53. Beal, J. H. L.; Bubendorfer, A.; Kemmitt, T.; Hoek, I.; Mike Arnold, W. *Biomicrofluidics* **2012**, *6*, 036503.

54. Martin, I. T.; Dressen, B.; Boggs, M.; Liu, Y.; Henry, C. S.; Fisher, E. R. *Plasma Processes and Polymers* **2007**, *4*, 414-424.

55. Buckley, J. S.; Liu, Y.; Monsterleet, S. **1998**.

56. McGuire, P. L.; Chatham, J. R.; Paskvan, F. K.; Sommer, D. M.; Carini, F. H. *Soc. Pet. Eng. J.* **2005**.

57. Nasralla, R. A.; Alotaibi, M. B.; Nasr-El-Din, H. A. *Soc. Pet. Eng. J.* **2011**.

58. Rivet, S. M.; Lake, L. W. *Soc. Pet. Eng. J.* **2010**.

59. Tarvin, J. A.; Gustavson, G.; Balkunas, S.; Sherwood, J. D. *J. Pet. Sci. Eng.* **2008**, *61*, 75–87.

60. Sevin, J.; Capron, B. *Energy Perspectives* **2013**.

61. Boussour, S.; Cissokho, M.; Cordier, P.; Bertin, H.; Hamon, G. *Soc. Pet. Eng. J.* **2009**.

62. Youn, S.-W.; Noguchi, T.; Takahashi, M.; Maeda, R. *Microelectron. Eng.* **2008**, *85*, 918-921.

63. Ogończyk, D.; Węgrzyn, J.; Jankowski, P.; Dąbrowski, B.; Garstecki, P. *Lab Chip* **2010**, *10*, 1324-1327.

64. Han, J.-H.; Yoon, J.-Y. *J. Biol. Eng.* **2009**, *3*, 6.

65. Klank, H.; Kutter, J. P.; Geschke, O. *Lab Chip* **2002**, *2*, 242-246.

66. Hong, T.-F.; Ju, W.-J.; Wu, M.-C.; Tai, C.-H.; Tsai, C.-H.; Fu, L.-M. *Microfluid. Nanofluid.* **2010**, *9*, 1125-1133.

67. Boone, T. D.; Fan, Z. H.; Hooper, H. H.; Ricco, A. J.; Tan, H.; Williams, S. J.; ACS Publications, 2002.

68. Chen, C.-S.; Breslauer, D. N.; Luna, J. I.; Grimes, A.; Chin, W.-c.; Lee, L. P.; Khine, M. *Lab Chip* **2008**, *8*, 622-624.

69. Young, E. W.; Berthier, E.; Guckenberger, D. J.; Sackmann, E.; Lamers, C.; Meyvantsson, I.; Huttenlocher, A.; Beebe, D. J. *Anal. Chem.* **2011**, *83*, 1408-1417.

70. Duffy, D. C.; McDonald, J. C.; Schueller, O. J.; Whitesides, G. M. *Anal. Chem.* **1998**, *70*, 4974-4984.

71. McDonald, J. C.; Duffy, D. C.; Anderson, J. R.; Chiu, D. T.; Wu, H.; Schueller, O. J.; Whitesides, G. M. *ELECTROPHORESIS: An International Journal* **2000**, *21*, 27-40.

72. McDonald, J. C.; Whitesides, G. M. *Acc. Chem. Res.* **2002**, *35*, 491-499.

73. Becker, H.; Gärtner, C. *ELECTROPHORESIS: An International Journal* **2000**, *21*, 12-26.

74. Attia, U. M.; Marson, S.; Alcock, J. R. *Microfluid. Nanofluid.* **2009**, *7*, 1.

75. Chiou, C.-H.; Lee, G.-B. *Journal of Micromechanics and Microengineering* **2004**, *14*, 1484.

76. Lin, C.-H.; Lee, G.-B.; Chang, B.-W.; Chang, G.-L. *Journal of Micromechanics and Microengineering* **2002**, *12*, 590.

77. Au, A. K.; Lee, W.; Folch, A. *Lab Chip* **2014**, *14*, 1294-1301.

78. Kim, P.; Kwon, K. W.; Park, M. C.; Lee, S. H.; Kim, S. M.; Suh, K. Y. *Biochip Journal* **2008**, *2*, 1-11.

79. Klasner, S. A.; Price, A. K.; Hoeman, K. W.; Wilson, R. S.; Bell, K. J.; Culbertson, C. T. *Anal. Bioanal. Chem.* **2010**, *397*, 1821-1829.

80. Buchegger, W.; Wagner, C.; Lendl, B.; Kraft, M.; Vellekoop, M. J. *Microfluid. Nanofluid.* **2011**, *10*, 889-897.

81. Chan, K. A.; Gulati, S.; Edel, J. B.; de Mello, A. J.; Kazarian, S. G. *Lab Chip* **2009**, *9*, 2909-2913.

82. Kulka, S.; Kaun, N.; Baena, J. R.; Frank, J.; Svasek, P.; Moss, D.; Vellekoop, M. J.; Lendl, B. *Anal. Bioanal. Chem.* **2004**, *378*, 1735-1740.

83. Pan, T.; Kelly, R. T.; Asplund, M. C.; Woolley, A. T. *J. Chromatogr. A* **2004**, *1027*, 231-235.

84. Floyd, T. M.; Schmidt, M. A.; Jensen, K. F. *Ind. Eng. Chem. Res.* **2005**, *44*, 2351-2358.

85. Barnes, S. E.; Cygan, Z. T.; Yates, J. K.; Beers, K. L.; Amis, E. J. *Analyst* **2006**, *131*, 1027-1033.

86. Connatser, R. M.; Riddle, L. A.; Sepaniak, M. J. *J. Sep. Sci.* **2004**, *27*, 1545-1550.

87. Park, T.; Lee, S.; Seong, G. H.; Choo, J.; Lee, E. K.; Kim, Y. S.; Ji, W. H.; Hwang, S. Y.; Gweon, D.-G.; Lee, S. *Lab Chip* **2005**, *5*, 437-442.

88. Massin, C.; Vincent, F.; Homsy, A.; Ehrmann, K.; Boero, G.; Besse, P.-A.; Daridon, A.; Verpoorte, E.; De Rooij, N.; Popovic, R. *J. Magn. Reson.* **2003**, *164*, 242-255.

89. Mompeán, M.; Sánchez-Donoso, R. M.; Hoz, A.; Saggiomo, V.; Velders, A. H.; Gomez, M. V. *Nature communications* **2018**, *9*, 108.

90. Walton, J.; De Ropp, J.; Shutov, M.; Goloshevsky, A.; McCarthy, M.; Smith, R.; Collins, S. *Anal. Chem.* **2003**, *75*, 5030-5036.

91. Wheeler, A. R.; Chah, S.; Whelan, R. J.; Zare, R. N. *Sensors Actuators B: Chem.* **2004**, *98*, 208-214.

92. Kanda, V.; Kariuki, J. K.; Harrison, D. J.; McDermott, M. T. *Anal. Chem.* **2004**, *76*, 7257-7262.

93. Hao, Z.; Li, G.; Fang-yan, X.; Wei-hong, Z.; Qiu-lan, C.; Jian, C. *SPECTROSCOPY AND SPECTRAL ANALYSIS* **2017**, *37*, 350-355.

94. Duggan, M. P.; McCreedy, T.; Aylott, J. W. *Analyst* **2003**, *128*, 1336-1340.

95. Hassan, S.-u.; Nightingale, A. M.; Niu, X. *Micromachines* **2017**, *8*, 58.

96. Ottevaere, H.; Van Overmeire, S.; Albero, J.; Nieradko, L.; Desmet, G.; Gorecki, C.; Thienpont, H. *Microfluid. Nanofluid.* **2015**, *18*, 559-568.

97. Pires, N. M. M.; Dong, T.; Hanke, U.; Hoivik, N. *Sensors* **2014**, *14*, 15458-15479.

98. Zhan, W.; Alvarez, J.; Crooks, R. M. *J. Am. Chem. Soc.* **2002**, *124*, 13265-13270.

99. Yakovleva, J.; Davidsson, R.; Bengtsson, M.; Laurell, T.; Emnéus, J. *Biosens. Bioelectron.* **2003**, *19*, 21-34.

100. Heyries, K. A.; Loughran, M. G.; Hoffmann, D.; Homsy, A.; Blum, L. J.; Marquette, C. A. *Biosens. Bioelectron.* **2008**, *23*, 1812-1818.

101. Sardesai, N. P.; Kadimisetty, K.; Faria, R.; Rusling, J. F. *Anal. Bioanal. Chem.* **2013**, *405*, 3831-3838.

102. Ohlsson, P. D.; Ordeig, O.; Mogensen, K. B.; Kutter, J. P. *Electrophoresis* **2009**, *30*, 4172-4178.

103. Kuijt, J.; Garcıa-Ruiz, C.; Stroomberg, G.; Marina, M.; Ariese, F.; Brinkman, U. T.; Gooijer, C. *J. Chromatogr. A* **2001**, *907*, 291-299.

104. Barat, D.; Benazzi, G.; Mowlem, M. C.; Ruano, J. M.; Morgan, H. *Opt. Commun.* **2010**, *283*, 1987-1992.

105. Dungchai, W.; Chailapakul, O.; Henry, C. S. *Anal. Chem.* **2009**, *81*, 5821-5826.

106. Hu, J.; Wang, S.; Wang, L.; Li, F.; Pingguan-Murphy, B.; Lu, T. J.; Xu, F. *Biosens. Bioelectron.* **2014**, *54*, 585-597.

107. Noiphung, J.; Songjaroen, T.; Dungchai, W.; Henry, C. S.; Chailapakul, O.; Laiwattanapaisal, W. *Anal. Chim. Acta* **2013**, *788*, 39-45.

108. Chikkaveeraiah, B. V.; Mani, V.; Patel, V.; Gutkind, J. S.; Rusling, J. F. *Biosens. Bioelectron.* **2011**, *26*, 4477-4483.

109. Pumera, M.; Merkoçi, A.; Alegret, S. *TrAC, Trends Anal. Chem.* **2006**, *25*, 219-235.

110. Zimmerman, W. B. *Chem. Eng. Sci.* **2011**, *66*, 1412-1425.

111. Lin, L.; Lin, J.-M. In *Cell Analysis on Microfluidics*; Springer, 2018, pp 291-311.

112. Pedde, R. D.; Li, H.; Borchers, C. H.; Akbari, M. *Trends Biotechnol.* **2017**, *35*, 954-970.

113. Jie, M.; Mao, S.; Li, H.; Lin, J.-M. *Chin. Chem. Lett.* **2017**, *28*, 1625-1630.

114. Kutter, J. P. *TrAC, Trends Anal. Chem.* **2000**, *19*, 352-363.

115. Sahore, V.; Kumar, S.; Rogers, C.; Jensen, J.; Sonker, M.; Woolley, A. *Anal. Bioanal. Chem.* **2016**, *408*, 599-607.

116. Fanguy, J. C.; Henry, C. S. *The Analyst* **2002**, *127*, 1021-1023.

117. Kenyon, S. M.; Meighan, M. M.; Hayes, M. A. *Electrophoresis* **2011**, *32*, 482-493.

118. Gerold, C. T.; Henry, C. S. *Langmuir* **2018**, *34*, 1550-1556.

119. Huang, X.; Gordon, M. J.; Zare, R. N. *Anal. Chem.* **1988**, *60*, 1837-1838.

120. Pittman, J. L.; Henry, C. S.; Gilman, S. D. *Anal. Chem.* **2003**, *75*, 361-370.

121. Akyazi, T.; Basabe-Desmonts, L.; Benito-Lopez, F. *Anal. Chim. Acta* **2018**, *1001*, 1-17.

122. Viskari, P. J.; Landers, J. P. *Electrophoresis* **2006**, *27*, 1797-1810.

123. Jokerst, J. C.; Emory, J. M.; Henry, C. S. *Analyst* **2012**, *137*, 24-34.

124. Guan, Q.; Henry, C. S. *Electrophoresis* **2009**, *30*, 3339-3346.

125. Noh, H. B.; Lee, K. S.; Lim, B. S.; Kim, S. J.; Shim, Y. B. *Electrophoresis* **2010**, *31*, 3053-3060.

126. Alves-Segundo, R.; Ibañez-Garcia, N.; Baeza, M.; Puyol, M.; Alonso-Chamarro, J. *Microchimica Acta* **2011**, *172*, 225-232.

127. Mashaghi, S.; Abbaspourrad, A.; Weitz, D. A.; van Oijen, A. M. *TrAC, Trends Anal. Chem.* **2016**, *82*, 118-125.

128. Jain, V.; Raj, T. P.; Deshmukh, R.; Patrikar, R. *Microsystem Technologies* **2017**, *23*, 389-397.

129. Wirdatmadja, S. A.; Moltchanov, D.; Balasubramaniam, S.; Koucheryavy, Y. *IEEE Access* **2017**, *5*, 2417-2429.

130. Miled, A.; Greener, J.; Multidisciplinary Digital Publishing Institute, 2017.

131. Xiong, B.; Ren, K.; Shu, Y.; Chen, Y.; Shen, B.; Wu, H. *Adv. Mater.* **2014**, *26*, 5525-5532.

132. Araci, I. E.; Brisk, P. *Curr. Opin. Biotechnol.* **2014**, *25*, 60-68.

133. Kim, M.; Sell, A.; Sinton, D. *Lab Chip* **2013**, *13*, 2508–2518.

134. Tanino, Y.; Akamairo, B.; Christensen, M.; Bowden, S. A. In *Proceedings of the International Symposium of the Society of Core Analysts*; Society of Core Analysis, 2015.

135. Martinez, A. W.; Phillips, S. T.; Butte, M. J.; Whitesides, G. M. *Angew. Chem. Int. Ed.* **2007**, *46*, 1318-1320.

136. Bruzewicz, D. A.; Reches, M.; Whitesides, G. M. *Anal. Chem.* **2008**, *80*, 3387-3392.

137. Abe, K.; Suzuki, K.; Citterio, D. *Anal. Chem.* **2008**, *80*, 6928-6934.

138. Li, X.; Tian, J.; Nguyen, T.; Shen, W. *Anal. Chem.* **2008**, *80*, 9131-9134.

139. Fenton, E. M.; Mascarenas, M. R.; López, G. P.; Sibbett, S. S. *ACS Appl. Mater. Interfaces* **2008**, *1*, 124-129.

140. Li, X.; Tian, J.; Shen, W. *Cellulose* **2010**, *17*, 649-659.

141. Olkkonen, J.; Lehtinen, K.; Erho, T. *Anal. Chem.* **2010**, *82*, 10246-10250.

142. Dungchai, W.; Chailapakul, O.; Henry, C. S. *Analyst* **2011**, *136*, 77-82.

143. Chitnis, G.; Ding, Z.; Chang, C.-L.; Savran, C. A.; Ziaie, B. *Lab Chip* **2011**, *11*, 1161-1165.

144. Carrilho, E.; Martinez, A. W.; Whitesides, G. M. *Anal. Chem.* **2009**, *81*, 7091-7095.

145. Li, X.; Ballerini, D. R.; Shen, W. *Biomicrofluidics* **2012**, *6*, 011301.

146. Yang, Y.; Noviana, E.; Nguyen, M. P.; Geiss, B. J.; Dandy, D. S.; Henry, C. S. *Anal. Chem.* **2016**, *89*, 71-91.

147. Martinez, A. W.; Phillips, S. T.; Wiley, B. J.; Gupta, M.; Whitesides, G. M. *Lab Chip* **2008**, *8*, 2146-2150.

148. Almeida, M. I. G.; Jayawardane, B. M.; Kolev, S. D.; McKelvie, I. D. *Talanta* **2018**, *177*, 176-190.

149. Lisowski, P.; Zarzycki, P. K. *Chromatographia* **2013**, *76*, 1201-1214.

150. Martinez, A. W.; Phillips, S. T.; Whitesides, G. M.; Carrilho, E.; ACS Publications, 2009.

151. Yamada, K.; Henares, T. G.; Suzuki, K.; Citterio, D. *Angew. Chem. Int. Ed.* **2015**, *54*, 5294-5310.

152. Bhakta, S. A.; Borba, R.; Taba Jr, M.; Garcia, C. D.; Carrilho, E. *Anal. Chim. Acta* **2014**, *809*, 117-122.

153. Ariza-Avidad, M.; Salinas-Castillo, A.; Capitán-Vallvey, L. F. *Biosens. Bioelectron.* **2016**, *77*, 51-55.

154. Jayawardane, B. M.; McKelvie, I. D.; Kolev, S. D. *Talanta* **2012**, *100*, 454-460.

155. Fiorini, G. S.; Chiu, D. T. *Biotechniques* **2005**, *38*, 429-450.

156. Lebiga, E.; Fernandez, R. E.; Beskok, A. *Analyst* **2015**, *140*, 5006-5011.

157. Liu, F.; Zhang, C. *Sensors Actuators B: Chem.* **2015**, *209*, 399-406.

158. Li, L.; Zhang, Y.; Liu, F.; Su, M.; Liang, L.; Ge, S.; Yu, J. *Chem. Commun.* **2015**, *51*, 14030-14033.

159. Kim, Y.; Jang, G.; Lee, T. S. *ACS Appl. Mater. Interfaces* **2015**, *7*, 15649-15657.

160. Shao, J.; Tong, L.; Tang, S.; Guo, Z.; Zhang, H.; Li, P.; Wang, H.; Du, C.; Yu, X.-F. *ACS Appl. Mater. Interfaces* **2015**, *7*, 5391-5399.

161. Chagas, C. L.; Costa Duarte, L.; Lobo‐Júnior, E. O.; Piccin, E.; Dossi, N.; Coltro, W. K. *Electrophoresis* **2015**, *36*, 1837-1844.

162. Gong, M. M.; Nosrati, R.; San Gabriel, M. C.; Zini, A.; Sinton, D. *J. Am. Chem. Soc.* **2015**, *137*, 13913-13919.

163. Sriram, G.; Bhat, M. P.; Patil, P.; Uthappa, U. T.; Jung, H.-Y.; Altalhi, T.; Kumeria, T.; Aminabhavi, T. M.; Pai, R. K.; Madhuprasad; Kurkuri, M. D. *TrAC, Trends Anal. Chem.* **2017**, *93*, 212-227.

164. Cate, D. M.; Dungchai, W.; Cunningham, J. C.; Volckens, J.; Henry, C. S. *Lab Chip* **2013**, *13*, 2397-2404.

165. Lee, V. B. C.; Mohd-Naim, N. F.; Tamiya, E.; Ahmed, M. U. *Anal. Sci.* **2018**, *34*, 7-18.

166. Arduini, F.; Cinti, S.; Scognamiglio, V.; Moscone, D. In *Comprehensive Analytical Chemistry*, Palchetti, I.; Hansen, P.-D.; Barceló, D., Eds.; Elsevier, 2017, pp 385-413.

167. Bisha, B.; Adkins, J. A.; Jokerst, J. C.; Chandler, J. C.; Pérez-Méndez, A.; Coleman, S. M.; Sbodio, A. O.; Suslow, T. V.; Danyluk, M. D.; Henry, C. S. *Journal of visualized experiments: JoVE* **2014**.

168. Koesdjojo, M. T.; Wu, Y.; Boonloed, A.; Dunfield, E. M.; Remcho, V. T. *Talanta* **2014**, *130*, 122-127.

169. Komatsu, T.; Mohammadi, S.; Busa, L. S. A.; Maeki, M.; Ishida, A.; Tani, H.; Tokeshi, M. *Analyst* **2016**, *141*, 6507-6509.

170. Jokerst, J.; Adkins, J.; Bisha, B.; Mentele, M.; Goodridge, L.; Henry, C. In *15th International Conference On Miniaturized Systems For Chemistry and Life Sciences 2011, Microtas 2011*, 2011, pp 2116-2118.

171. Busa, L. S. A.; Mohammadi, S.; Maeki, M.; Ishida, A.; Tani, H.; Tokeshi, M. *Micromachines* **2016**, *7*, 86.

172. Musile, G.; Wang, L.; Bottoms, J.; Tagliaro, F.; McCord, B. *Analytical Methods* **2015**, *7*, 8025-8033.

173. Pesenti, A.; Taudte, R. V.; McCord, B.; Doble, P.; Roux, C.; Blanes, L. *Anal. Chem.* **2014**, *86*, 4707-4714.

174. Kim, J.-Y.; Yeo, M.-K. *Molecular & Cellular Toxicology* **2016**, *12*, 101-109.

175. Jokerst, J. C.; Adkins, J. A.; Bisha, B.; Mentele, M. M.; Goodridge, L. D.; Henry, C. S. *Anal. Chem.* **2012**, *84*, 2900-2907.

176. Lin, Y.; Gritsenko, D.; Feng, S.; Teh, Y. C.; Lu, X.; Xu, J. *Biosens. Bioelectron.* **2016**, *83*, 256-266.

177. Tian, T.; Li, J.; Song, Y.; Zhou, L.; Zhu, Z.; Yang, C. J. *Lab Chip* **2016**, *16*, 1139-1151.

178. Gerold, C. T.; Bakker, E.; Henry, C. S. *Anal. Chem.* **2018**.

179. Cate, D. M.; Noblitt, S. D.; Volckens, J.; Henry, C. S. *Lab Chip* **2015**, *15*, 2808-2818.

180. Zuk, R.; Ginsberg, V.; Houts, T.; Rabbie, J.; Merrick, H.; Ullman, E.; Fischer, M.; Sizto, C. C.; Stiso, S.; Litman, D. *Clin. Chem.* **1985**, *31*, 1144-1150.

181. Allen, M. P.; Delizza, A.; Ramel, U.; Jeong, H.; Singh, P. *Clin. Chem.* **1990**, *36*, 1591-1597.

182. Chen, Y.-T.; Yang, J.-T. *Biomed. Microdevices* **2015**, *17*, 52.

183. Liu, V.; Lin, T.-Y.; Schrier, W.; Allen, M.; Singh, P. *Clin. Chem.* **1993**, *39*, 1948-1952.

184. Musharraf, S. G.; Shoaib, M.; Siddiqui, A. J.; Najam-ul-Haq, M.; Ahmed, A. *Chem. Cent. J.* **2012**, *6*, 56.

185. Public Health Statement for Nickel. https://www.atsdr.cdc.gov/PHS/PHS.asp?id=243&tid=44 (accessed April 25, 2018).

186. Lead and Copper Rule. https://www.epa.gov/dwreginfo/lead-and-copper-rule (accessed April 25, 2018).

187. Secondary Drinking Water Standards: Guidance for Nuisance Chemicals. https://www.epa.gov/dwstandardsregulations/secondary-drinking-water-standards-guidance-nuisance-chemicals (accessed April 25, 2018).

188. Rattanarat, P.; Dungchai, W.; Cate, D. M.; Siangproh, W.; Volckens, J.; Chailapakul, O.; Henry, C. S. *Anal. Chim. Acta* **2013**, *800*, 50-55.

189. Mentele, M. M.; Cunningham, J.; Koehler, K.; Volckens, J.; Henry, C. S. *Anal. Chem.* **2012**, *84*, 4474-4480.

190. Cate, D. M.; Nanthasurasak, P.; Riwkulkajorn, P.; L'Orange, C.; Henry, C. S.; Volckens, J. *Ann. Occup. Hyg.* **2014**, *58*, 413-423.

191. Jayawardane, B. M.; Wei, S.; McKelvie, I. D.; Kolev, S. D. *Anal. Chem.* **2014**, *86*, 7274-7279.

192. Ortiz-Gomez, I.; Ortega-Muñoz, M.; Salinas-Castillo, A.; Álvarez-Bermejo, J. A.; Ariza-Avidad, M.; de Orbe-Payá, I.; Santoyo-Gonzalez, F.; Capitan-Vallvey, L. F. *Talanta* **2016**, *160*, 721-728.

CHAPTER 2. OBSERVATION OF DYNAMIC SURFACTANT ADSORPTION FACILITATED BY DIVALENT CATION BRIDGING

Dynamic evidence of the mechanism for surfactant adsorption to surfaces of like charge has been observed. Additionally, removal and retention of surfactant molecules on the surface were observed as a function of time. A decrease in surface charge is observed when metal counter ions are introduced and is dependent on charge density as well as valency of the metal ion. When surfactant species are also present with the metals a dramatic increase in surface charge arises. We observed that the rate and quantity of surfactant adsorption can be controlled by the presence of divalent Ca^{2+}. Under isotonic conditions the introduction of Ca^{2+} is also easily distinguishable from that of monovalent Na^{+} and provides dynamic evidence of the divalent "cation bridging" phenomenon. Dynamic changes to surface charge are experimentally determined by utilizing current monitoring to quantify the zeta potential in a microfluidic device. This work was funded by BP plc and was published in the ACS journal *Langmuir* (**2018**, *34* (4), pp 1550–1556).

Overview

Charged surfactants give rise to complexities surrounding surface chemistry due to their propensity to interact via a variety of mechanisms with surfaces. Absorption of charged surfactants onto charged surfaces even when the surface has the same charge has been observed and is understood to contribute to surface modification and/or fouling.[1-3] Similarly, adsorption of mono/divalent cationic metals has also been shown to alter effective surface charge. Unfortunately, in systems where both charged surfactants

and cationic metals are present, the surface chemistry cannot be predicted by the behavior of the individually adsorbed species. Previous research has hypothesized that when a negatively charged surface is exposed to a like-charged surfactant and a divalent cation is present, a phenomenon called ion binding or “cation bridging” results; whereby the divalent species facilitates the interaction of a negatively charged surfactant with a negatively charged surface.[4-9] Although the mechanism and strength of the interactions possibly vary from that of divalent species, it should be noted that adsorption of a like-charged species has also been observed to occur in the presence of monovalent ions.[10,11] Evidence that currently supports the cation bridging phenomenon was acquired using methods that probed the surface minutes, or even hours, between alterations to surface chemistry and under static conditions.[4] Investigation of surfaces using large intervals between measurements prevents acquisition of intermediate data that could be critical for understanding dynamic systems.

To fully regulate surface chemistry, the specific interactions of charged surfactants and divalent species at a charged surface must be studied with a technique that provides time resolution. These interactions can be investigated by monitoring the mobility of the electroosmotic flow (μ_{EOF}, $cm^2 \bullet V^{-1} \bullet s^{-1}$), which describes the velocity of fluid flowing in response to an applied electric potential; μ_{EOF} data can be used to determine the effective surface charge, or zeta potential. Zeta potential can be used to describe the interactive electric potential of a surface relative to the bulk solution surrounding a charged surface. Understanding the importance of zeta potential, and its relevance to surface chemistry requires that the structure of the electric double layer (EDL) be considered (Figure 2.1).

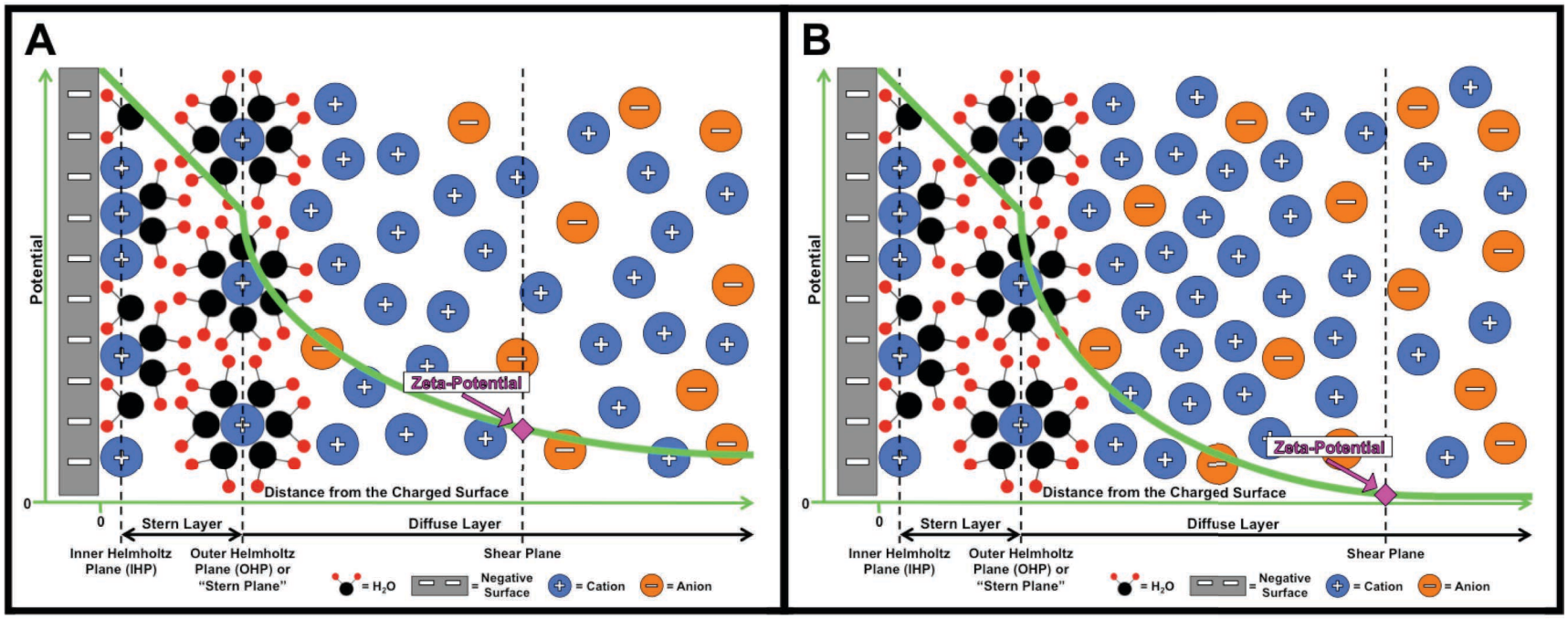

Figure 2.1. Illustration of the electric double layer (EDL) before **A)** and after **B)** an increase in ionic strength of counter ions. Note, all ions outside of the Stern layer have fully solvated shells and have been excluded in these diagrams

A charged surface, which will hereafter be assumed to be negatively charged, will specifically and non-specifically adsorb charged ion species. Specifically adsorbed ions can possess a chemical or specific affinity for the surface in addition to Coulomb interactions; non-specifically adsorbed ions are attracted to the surface by purely Coulombic attractions.[12] An imaginary plane runs through the center of the specifically adsorbed ions' charged spheres and is called the Inner Helmholtz Plane (IHP). Ions surrounded by a solvation shell are also attracted to the negatively charged surface and can be adsorbed. Another imaginary plane runs through the center of the adsorbed solvated ions' charged spheres and is called the Outer Helmholtz Plane (OHP) or Stern plane. The space between the IHP and OHP is called the Stern layer, which is the first layer of the EDL and is where ions are specifically and non-specifically adsorbed.[12] The second layer of the EDL is called the diffuse layer, which is located farther away from the charged surface than the Stern layer and starts after the OHP. The diffuse layer consists of a mobile and immobile portion with the mobile portion being located farther from the surface relative to the immobilized component. The thickness of the diffuse layer is dependent on concentration of counter and co-ions in the solution, which affects the magnitude of the charge density in the stern layer and thus the electric screening length (k^{-1}) of the negatively charged surface; as counter ion concentration increases, k^{-1} decreases and thickness of the diffuse layer decreases.[12] Co-ions would cause k^{-1} to increase and thickness of the diffuse layer to increase. The plane where the mobile and immobile portions of the diffuse layer meet is called the shear plane. Like the thickness of the diffuse layer, the distance of the shear plane from the negatively charged surface changes as a function of counter and co-ion concentrations; as counter ion

concentration increases, counter ion free mobility decreases, the distance from the surface that is required for a counter ion to move freely increases and the distance between the charged surface and the shear plane increases.[13]

The electric potential that exists between the charged surface and a point in the bulk solution is called the surface potential. Similarly, the electric potential at the OHP relative to a point in the bulk solution is called the Stern potential. Both the surface and Stern potentials have been suggested to be inappropriate for describing the electric potential that predicts the interactions that occur between charged surfaces and surrounding bulk solution, this is due to the immobile nature of the ions associated with those components of the EDL.[12,14] To accurately predict the interactions that occur between a charged surface and bulk solution, the electric potential at the shear plane must be used since the shear plane is the point in space where ions cease to remain immobilized on a surface and begin to move with the surrounding solution.[15] The electric potential at the shear plane, relative to a point in the bulk solution, is called the zeta potential. The importance of zeta potential can now be understood since it is describing the potential at the point on the charged surface's EDL where ions become mobile in the diffuse layer and can effectively interact with the surrounding mobile ions and bulk solution. Thus, measurement and quantification of a surface's zeta potential can be used to help describe representative changes to the structure of the surface's EDL. [16,17] Zeta potential measurements can consequentially allude to the effects that occur upon the addition of salts and surfactants to the solution surrounding the surface.

The presence of a cationic species, such as Na^{+} and Ca^{2+}, has been shown to decrease the magnitude of a negatively charged surface's zeta potential.[18-21] A

decrease in zeta potential by cations is a result of a decrease in k^{-1}, which is due to an increase in the positive charge density located at the stern layer (Figure 2.1). Similarly, cationic[22,23] and anionic[24,25] surfactants can affect a negatively charged surface's zeta potential by modifying the charge density at the surface. Herein, we observe that when a charged surface has been simultaneously exposed to both metal salts and surfactants, outcomes that represent exposure by solely a salt or a surfactant in solution are not evident and vary depending on the presence of either monovalent or divalent counter ions while being independent from ionic strength.

In this study, we present dynamic real-time evidence of the cation bridging phenomenon occurring at a polydimethylsiloxane (PDMS) surface between a 2-naphthoate (2NA, structure shown in Figure 2.8) surfactant and divalent Ca^{2+}. We have chosen PDMS to monitor effective surface charge since it is commercially available, possesses chemical functionalities and charge properties that are well studied, and is capable of being used to create inexpensive microfluidic devices.[26-29] It is important to considered that the negative functionality exhibited by the PDMS surface is due to –Si–OH (silanol) groups (pKa ≈ 4) that are exposed at the material's surface.[30,31] Quantifiable effective surface charge is described using zeta potential values that are acquired via the utilization of electroosmotic flow (EOF) techniques and the current monitoring method. The dynamic experimental results found within provide evidence and support the following hypotheses: a) decreases in zeta potential are dependent on the charge density and specific valence of counter ions, b) simultaneous presence of divalent counter ions and surfactants results in an increase in zeta potential values that is distinct from the presence of monovalent counter ions and is evidence of the divalent

bridging effect, and c) changes in ionic strength can cause unstable changes in zeta potential but are insignificant when effects imparted by specific cations are considered.

Experimental

Materials and Solutions

Reagents used for fabrication of microfluidic devices include SU-8 2050 photoresist (Microchem, Westborough, MA), Sylgard 184 elastomer and curing agent (PDMS) (Dow Corning, Midland, MI), and 100-mm silicon wafers (University Wafer, South Boston, MA). Aqueous solutions were prepared in 18.2 MΩ•cm water from a Millipore Milli-Q purification system (Millipore, Billerica, MA). Experimental stock solutions were prepared from 2-(N-Morpholino)ethanesulfonic acid (MES, ≥ 99.0% purity, Acros Organics, Figure 2.2.A), L-Histidine (His, 98.5% purity, Fisher Scientific, Figure 2.2.B), 2-Naphthoic acid (2NA, 98% purity, Aldrich), $CaCl_2$ (99% purity, Aldrich),

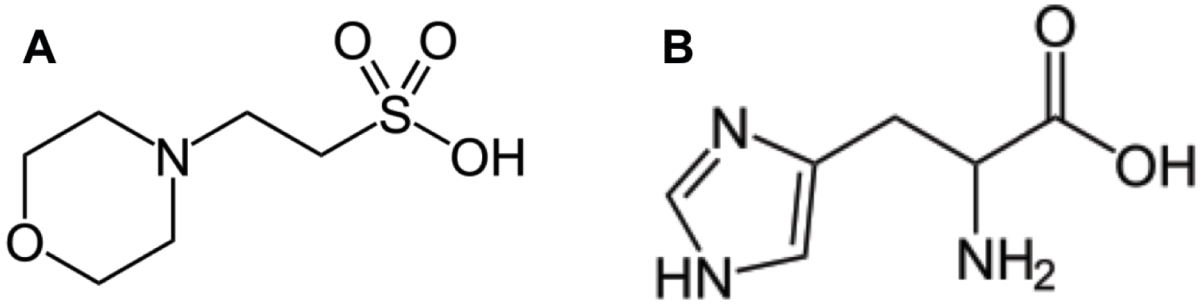

Figure 2.2. Structures for the buffer components of sample solutions. **A)** 2-(N-Morpholino)ethanesulfonic acid (MES) and **B)** Histidine (His)

$MgCl_2$ (98% purity, Fisher), NaCl (99% purity, Macron) and KCl (99.3% purity, Acros). Individual stock solutions were prepared as follows: MES 0.3824 g in 20.00 mL H_2O, His 0.1552 g in 20.00 mL H_2O and 2NA 0.3444 g in 10.00 mL HPLC grad ethanol, $CaCl_2$ 0.3329 g in 20.00 mL H_2O, $MgCl_2$ 0.1428 g in 20.00 mL H_2O, NaCl 0.1753 g in

20.00 mL H_2O and KCl 0.1118 in 20.00 mL H_2O. All experimental solutions contained 20.00 mM His and were made to have a pH of 6.0 ± 0.1 by adjusting the concentration of MES from 24.60–27.21 mM, which was required to maintain the desired pH when 2NA (1.00 mM) was added. To make two solutions of different ionic strengths, one portion of the solution was diluted to 90% of its original concentration; these solutions will hereafter be referred to as the “100%” and “90%” solutions. All chemicals were used as received without further purification.

Fabrication of Microfluidic PDMS Devices

Zeta potential values were acquired using straight-channeled microfluidic devices to collect experimental data and were fabricated using a previously described method.[32] A 4-in. silicon wafer was cleaned using isopropanol, methanol and H_2O followed by plasma cleaning at 150 W and 0.80 torr (atmosphere) for 5 min. The silicon wafer was then coated with SU-8 2050 negative photoresist using a spin coater with settings recommended by the photoresist manufacturer to achieve a 50 μm layer. The coated wafer was baked at 95 °C for 15 min. A digitally produced mask was then placed on the photoresist, and the system was exposed to a near-UV light source for 80 sec. After exposure and postbaking at 95 °C for 15 min, the wafer was developed in propylene glycol methyl ether acetate leaving a positive relief patten on the wafer and was followed by a final bake at 150 ºC for 30 min. Once the master was completed, replica molding was used to create channels in PDMS. A degassed mixture of PDMS and Sylgard 184 elastomer curing agent (10:1) was poured onto the silicon wafer and cured at 65 °C for 3 h. At that time, the PDMS was peeled off the silicon wafer, leaving a

negative relief of the channels and reservoirs in the PDMS. An 8-mm-diameter punch was used to open the reservoirs, and the PDMS was trimmed to size with a razor blade. Irreversible PDMS sealing was used for the assembly of the microfluidic devices. A PDMS replica and a microscope slide covered with a 25 μm layer of cured PDMS were placed simultaneously in an air plasma cleaner (Harrick plasma cleaner/sterilizer PDG-32G) and oxidized for 40 s using atmospheric air. The two pieces were then brought into conformal contact directly after removal from the plasma cleaner to form an irreversible seal and were put in a 65 ºC oven for 48 hr before use. Microfluidic devices contained a 4 cm long channel with cross sectional dimensions of 50 x 50 μm and solution reservoirs that were capable of holding 500 μL located on each end of the channel.

EOF Measurements

Zeta potential values were calculated using the μ_{EOF}, which was measured experimentally using the current monitoring method.[33,34] The current monitoring method relies on measuring changes in current as a function of time as solutions of different ionic strength move through the channel. Initially one reservoir was filled with 350 μL of 90% solution and then, using a syringe to create positive pressure, the channel was manually primed with the 90% solution and the other reservoir was filled with the 100% solution. A platinum electrode was placed in each of the wells before a constant electric potential was applied (typically 2400 V) using a two-channel (one positive and one negative) laboratory built high-voltage power supply. The total current flowing through the system was measured as a voltage drop across a 38.5 kΩ resistor using a

multifunctional I/O device (National Instruments, USB-6210) and monitored using a laboratory designed LabView program. A schematic of the flow cell and electrodes has been provided in Figure 2.3. The initial positive electric potential was applied for 40–50

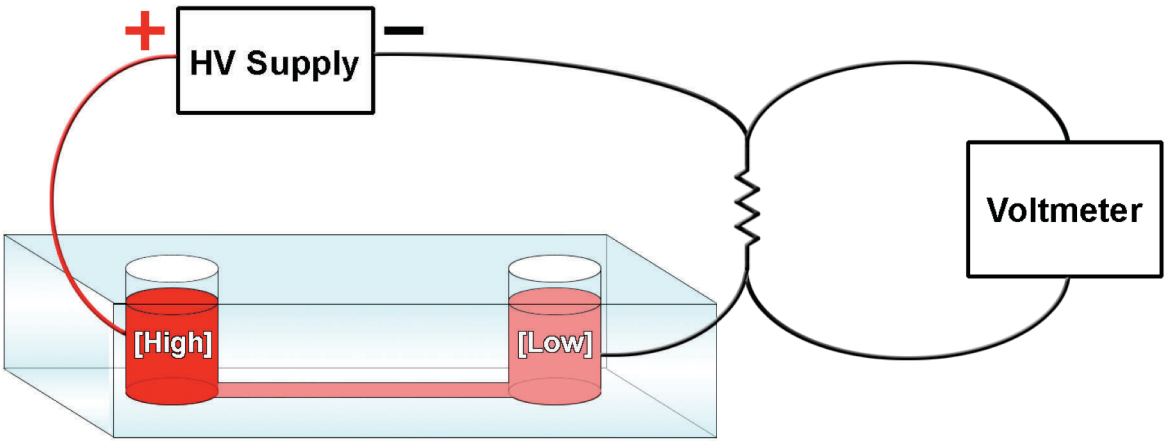

Figure 2.3. Schematic of the flow cell, high-voltage (HV) supply and voltmeter that was used to acquire EOF data. Pt electrodes (not shown) were attached to wire leads and positioned in sample wells from the top

s depending on the solution's observed mobility. At the end of 40–50 s a wait time of 15 s was instituted where no electric potential was applied allowing the solutions in the device to reach a steady state before changing the applied electric potential. A negative potential with a magnitude equal to the positive potential was then applied. The voltage cycling process was repeated for 80–170 cycles (one cycle being positive then negative potential).

Calculating μ_{EOF} and Zeta Potential

When an electric potential was applied, the time that was required for one solution to completely displace the other solution in the microfluidic channel was determined by taking the second derivative of the voltage data to determine the major

inflection point.[33] Values for the μ_{EOF} were calculated using the equation provided in Figure 2.4 for each voltage cycle by averaging the displacement times of a cycle.

$$\mu_{EOF} = \frac{L^2}{V \times time}$$

Figure 2.4

μ_{EOF} is mobility of the electroosmotic flow ($cm^2 \bullet V^{-1} \bullet s^{-1}$), L is length of channel (4 cm), V is the absolute value of the applied electric potential (most cases V = 2400 V) and time is the time required for a solution to travel from one end of the channel to the other (seconds). Once the μ_{EOF} was determined, it was converted to zeta potential using equation found in figure 2.5.

$$Z = \frac{-\mu_{EOF} \times \eta}{\varepsilon_r \times \varepsilon_0}$$

Figure 2.5

Z is zeta potential (mV), μ_{EOF} is electroosmotic mobility ($cm^2 \bullet V^{-1} \bullet s^{-1}$), η is the dynamic viscosity of water (8.9×10^{-4} Pa•s, 25 ºC), ε_r is the relative permittivity of water (78.3), and ε_0 is the permittivity of a vacuum (8.85×10^{-12} $C^2 \bullet J^{-1} \bullet m^{-1}$). Zeta potential measurements were made for a variety of surfactant and cation combinations as detailed below. Values for permittivity and viscosity were based on 25 ºC values although room temperatures fluctuated between 21–22 ºC. Herein, all true zeta potential values are negative, but will be described as relative absolute values to facilitate discussion.

Results and Discussion

Effects of Buffer

The impact of buffer on zeta potential was established first. Using a solution consisting of MES/His (27.60 mM/20.00 mM) buffer at pH 6 and NaCl (3.00 mM), the device was allowed to run for 100 voltage cycles and the relative zeta potential values as a function of cycle number were recorded in Figure 2.6. Zeta potential values

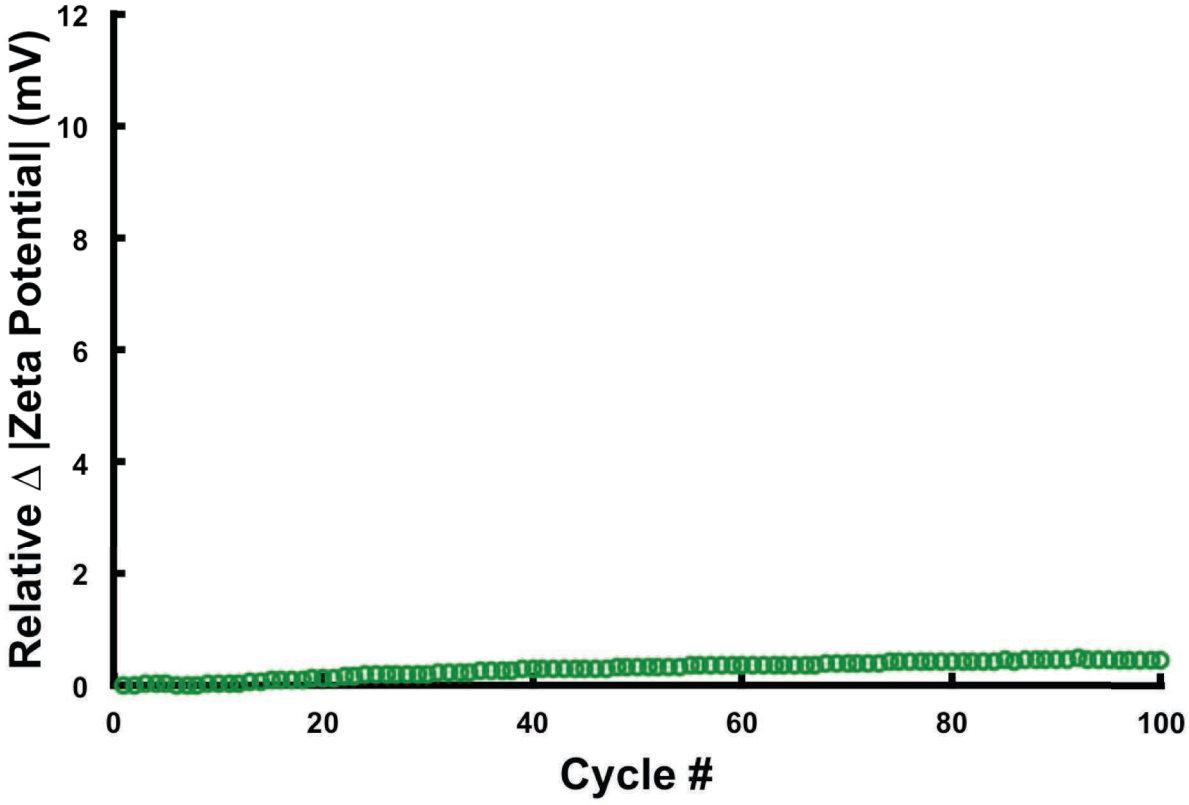

Figure 2.6. Changes in zeta potential of a PDMS microfluidic device due to a solution containing 2-(N-morpholino)ethanesulfonic acid (MES, 27.60 mM), L-Histidine (His, 20.00 mM) and NaCl (3.0 mM), monitored using the current monitoring method

increased less than 2% over the course of the experiment, an increase likely due to joule heating as a result of PDMS's low thermal conductivity (0.15 W/m).[35] Under the assumption that the increase in zeta potential values was due to joule heating, interactions that occur between the negatively charged PDMS device's surface and the

buffer/salt components are immediate and unchanging over time. It should be noted that 1) the scale on the y-axis (relative change in absolute zeta potential) is from 0–12 mV to allow comparison of y-axes across all graphs included within the publication, and 2) the real, non-absolute, zeta potential values herein are always negative and changes in zeta potential will be discussed as changes to the magnitude of the zeta potential.

Effects of Counter Ion Charge Density and Specific Valence

The impact of different metal cations was determined next. Initially, buffer was used to establish the zeta potential (5.49 ± 0.03 mV, n = 10) before adding different metals (Figure 2.7). After allowing the solutions to run in the device for 10 cycles, a solution containing the buffer and KCl (3.00 mM) was loaded into the device. Immediately a drop in zeta potential values to 2.76 ± 0.02 mV (n = 15) was observed and was due to an increase in ionic strength. As described above, increasing ionic strength and therefore the concentration of counter ions in solution causes a decrease in the k^{-1} as counter ions contribute to the neutralization of the surface potential and a decrease in zeta potential is observed. While keeping ionic strength constant KCl was replaced by NaCl (3.00 mM) and zeta potential values (2.3 ± 0.1 mV, n = 15) were observed to slightly decrease. A decrease in zeta potential values between solutions containing KCl and NaCl was attributed to an increase in charge density between the K^+ and Na^+ counter ions. While keeping ionic strength constant, NaCl was replaced with $CaCl_2$ (1.00 mM) while keeping the solution isotonic. Upon the addition of $CaCl_2$ zeta potential values immediately and significantly decreased to 0.59 ± 0.07 mV (n = 15).

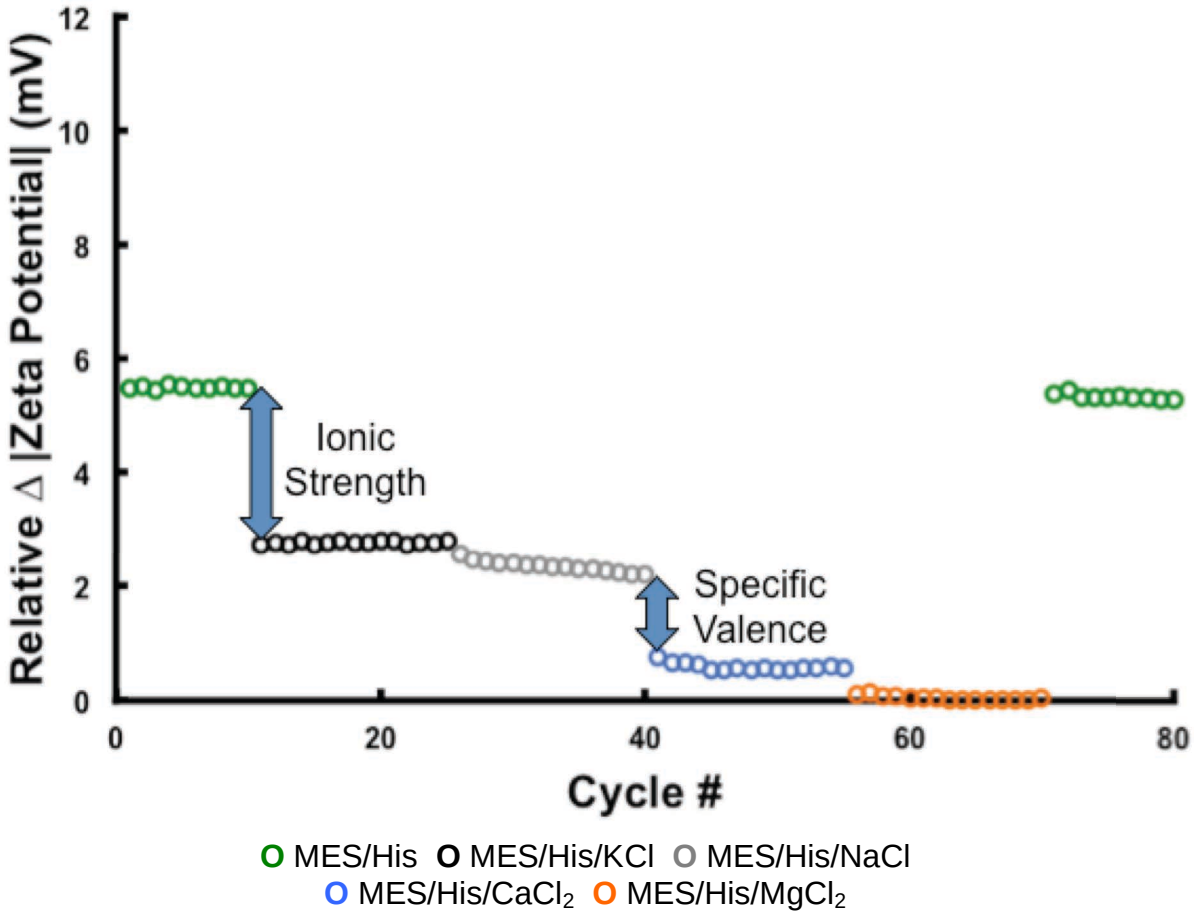

Figure 2.7. A solution containing a buffer (MES 27.60 mM, His 20.00 mM) is replaced with solutions that contain the same buffer and the addition of various ionic salts KCl (3.00 mM), NaCl (3.00 mM), $CaCl_2$ (1.00 mM) and $MgCl_2$ (1.00 mM)

The decrease in zeta potential values was again likely due to an increase in charge density going from Na^+ to Ca^{2+}. However, it is pertinent to recognize the change in valency that occurs when removing monovalent Na^+ and introducing divalent Ca^{2+}; as a consequence, the considerable drop in zeta potential between the solutions containing NaCl and $CaCl_2$ can be described as a result of the change in specific valence of the counter ions present. It should be noted that the changes in zeta potential are not likely due to the specific binding affinity of the PDMS surface for divalent cations since silanol functional groups are known to interact weakly with alkali/ne metals.[36] Effects of

changing the charge density of the counter ion present was seen again when $CaCl_2$ was removed and $MgCl_2$ was introduced resulting in a small decrease in zeta potential values to 0.04 ± 0.04 mV (n = 15). After the replacing the $MgCl_2$ solution with buffer containing no metal cations, an increase in zeta potential values to 5.33 ± 0.05 mV (n = 10) was observed. The increase in zeta potential following the removal of $MgCl_2$ occurred instantaneously and values differed by less than 3% of the original values. As described above, changes in effective surface charge that arise from the introduction or removal of a salt occur immediately and are relatively stabile over time as the solution undergoes concurrent voltage cycles. It is also important to note that the changes in zeta potential for all metals tested were immediate within the timeframe of data collection suggesting very fast kinetics for surface adsorption.

Effects of Anionic Surfactants on Zeta Potential

Dynamic interactions of surfactants with a charged surface have been previously documented.[37-39] Here, as depicted in Figure 2.8 when negatively charged 2-naphthoate (2NA) was added to solution, an increase in the zeta potential value to 9.7 ± 0.1 mV (n = 40) was observed over time. The increase in zeta potential in the case of 2NA is due to its negative charge at pH 6 (pKa = 4.17). Since the surface of PDMS is also negatively charged at pH 6, the adsorption of 2NA to the surface does not occur instantaneously. Conceptually, adsorption of negatively charged 2NA to a surface of like charge does not seem favorable or likely. For adsorption to occur, 2NA must overcome Coulombic repulsions via hydrophobic interactions or be facilitated by the screening of counter ions.[40] If attraction of 2NA to the surface overcomes repulsive forces then the

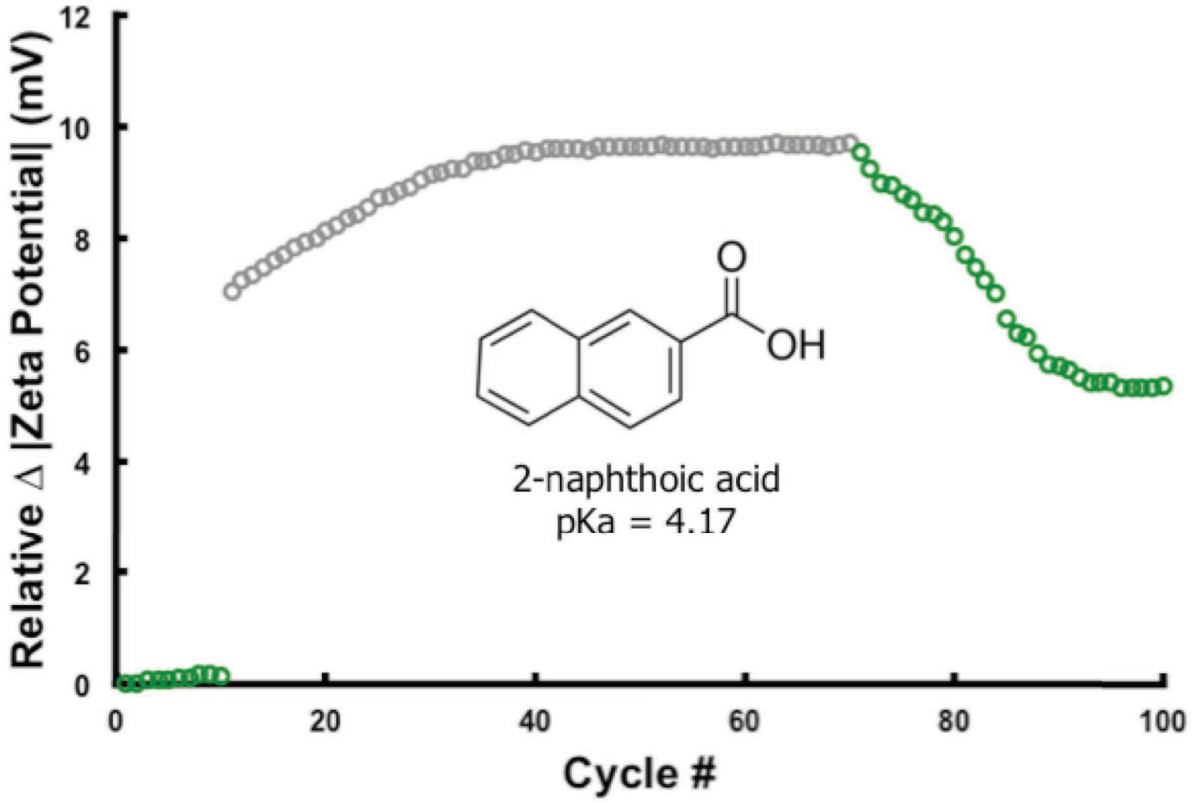

Figure 2.8. At constant ionic strength and pH, a solution containing 2-naphthoate (2NA) is introduced, an increase in zeta potential is observed and stabilization of values occurs at cycle 40. Upon the removal of 2NA, a decrease in zeta potential values over time is seen. Values do not return to pre-2NA values

adsorption of 2NA proceeds over time. Eventually repulsive forces overcome attraction of the surfactant to the like-charged surface and zeta potential values stabilize as no additional 2NA is permitted to adsorb.[41] Upon the removal of 2NA from solution, a decrease in zeta potential over time was observed. Ensuing stabilization of zeta potential values at levels higher than the starting values alludes to the retention of 2NA on the PDMS's negatively charged surface suggesting that simply removing the surfactant from solution does not effectively remove it from the surface.[41] Retention of

surfactant molecules on the surface has many implications where information regarding specific surface charge and chemistry is required.[42,43]

Effects of Divalent Counter Ions on Surfactant Adsorption

We next evaluated the impact of mixed surfactant-metal cation solutions on zeta potential. While keeping ionic strength constant, the zeta potentials for solutions containing 2NA and different concentrations of NaCl and $CaCl_2$ were determined. Data set A in Figure 2.9 had the lowest $CaCl_2$ concentration (0.25 mM) and the highest NaCl

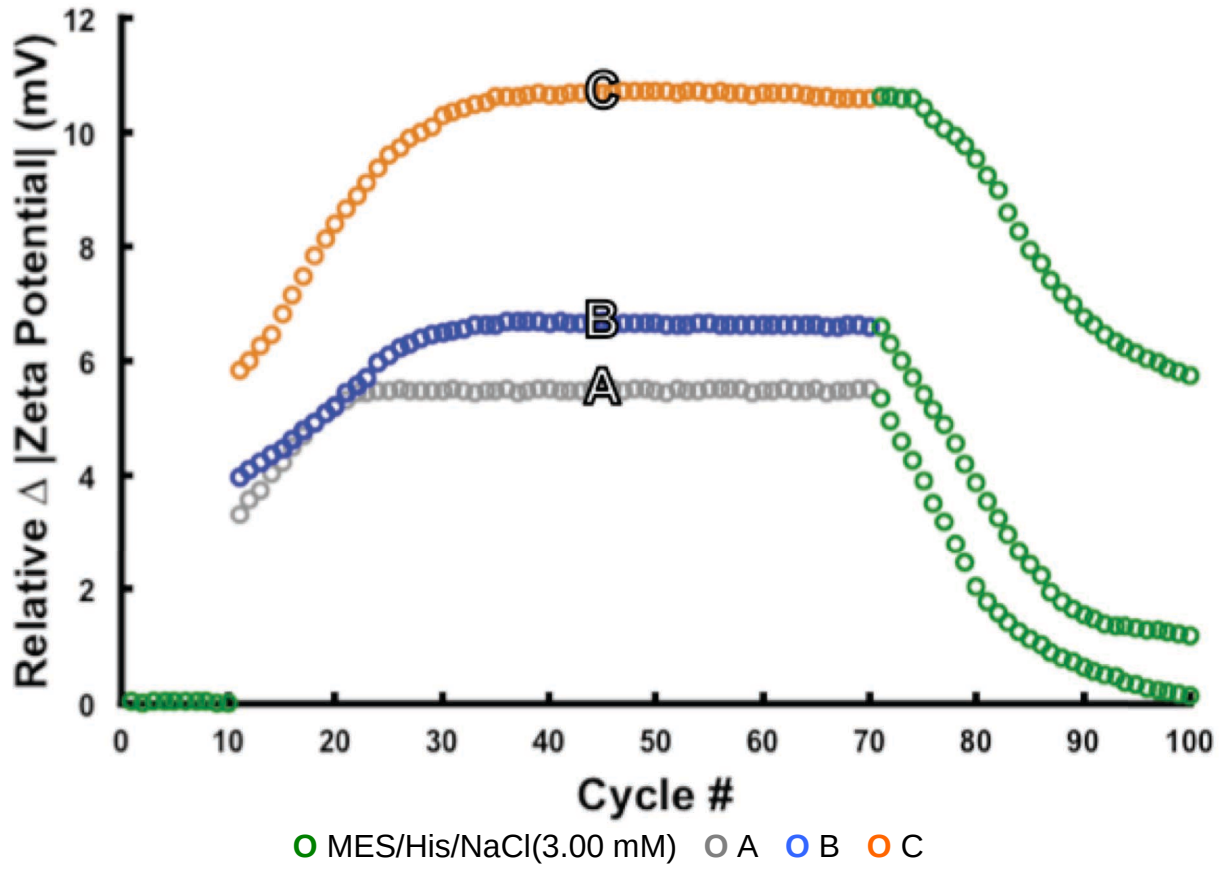

Figure 2.9. All solutions are kept at constant ionic strength and pH. All surfactant solutions contain 1.00 mM 2NA. **A)** 2.25 mM NaCl and 0.25 mM $CaCl_2$ **B)** 1.50 mM NaCl and 0.50 mM $CaCl_2$ **C)** 0.00 mM NaCl and 1.0 mM $CaCl_2$

concentration (2.25 mM). Data set B in Figure 2.9 contained 0.50 and 1.50 mM of $CaCl_2$ and NaCl respectfully. Data set C in Figure 2.9 contained the highest concentration of $CaCl_2$ (1.00 mM) and no NaCl. As shown in Figure 2.7, increasing the valency of counter ions present in solution in the absence of the surfactant causes a decrease in zeta potential. Figure 2.9 shows the opposite to be true when both surfactant and cation are present. It is important to note that at equal concentrations of $CaCl_2$ and 2NA (Figure 2.9.C) that the net effect on the absolute relative zeta potential is an increase over time. An overall increase in surface charge would mean that the effects of the surfactant on zeta potential outweigh that of the divalent Ca^{2+} species. Solutions that contained 0.25, 0.50 and 1.00 mM $CaCl_2$ caused overall increases of 5.49 ± 0.02, 6.64 ± 0.02 and 10.66 ± 0.04 mV (n = 30), respectfully, in the absolute values of zeta potential. This increase suggests that Ca^{2+} was facilitating the addition of 2NA to the surface and that we observed the dynamic effects of cation bridging on surface charge since monovalent species have been shown to minimally contribute to the bridging effect.[4] In addition, stabilization of zeta potential values occurs at an increasing number of cycles (22, 33 and 37 cycles) as $CaCl_2$ concentration increased (0.25, 0.50 and 1.00 mM, respectfully). A potential explanation for why values require more voltage cycles to stabilize, as $CaCl_2$ concentration increases, was due to the addition of bridging sites for 2NA. If $CaCl_2$ concentration increases, the availability of Ca^{2+} that can bridge 2NA to the negatively charged surface increases. Addition of 2NA to the surface has been shown to be a relatively slow process (Figure 2.8) and if adsorption to the surface were in part dictated by the presence of Ca^{2+}, increasing the quantity of divalent species would increase the time required for the surface to equilibrate with the surrounding solution.

Effects of Ionic Strength on Surfactant Adsorption

Investigation of ionic strength's effect on the adsorption of 2NA was investigated next (Figure 2.10). While keeping ionic strength constant, a solution containing 1.50 mM

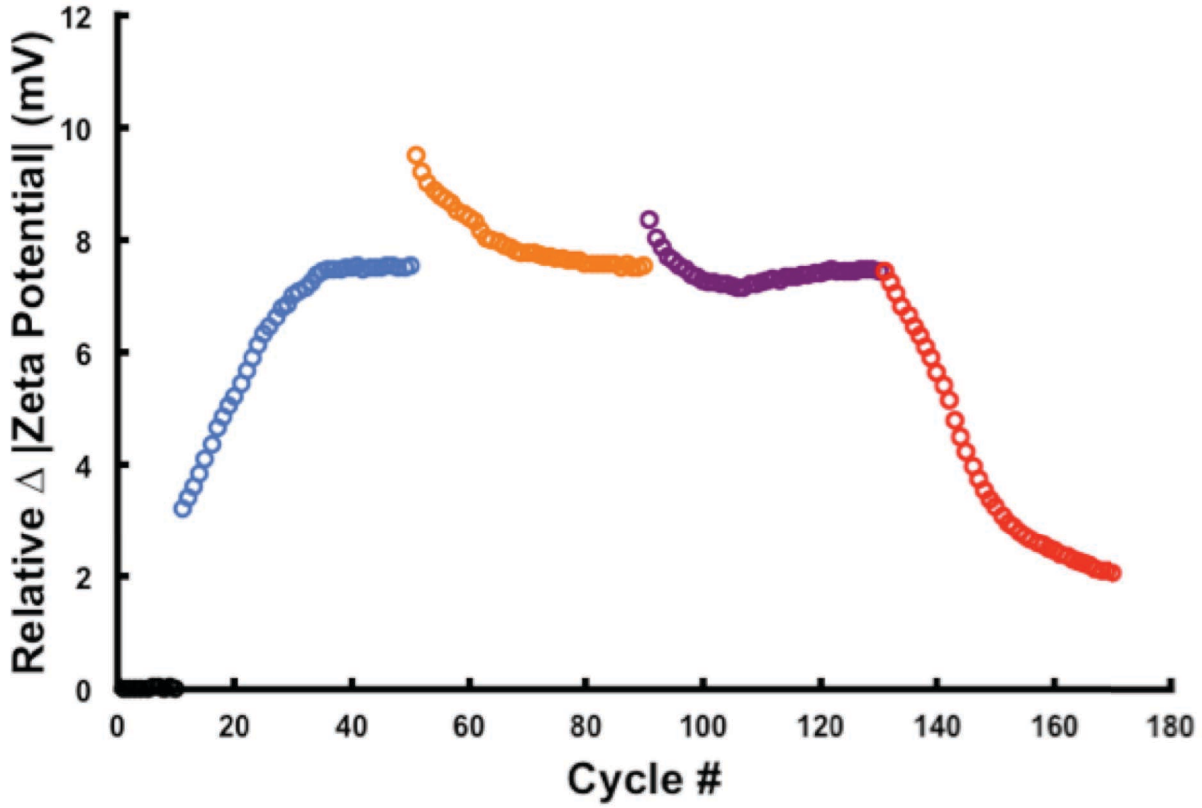

Figure 2.10. All surfactant solutions contain 1.00 mM 2NA. Ionic strength is not kept constant to illustrate variation in zeta potential due to counter ion concentration and ionic strength

NaCl is replaced with a solution containing both 0.50 mM $CaCl_2$ and 2NA (1.00 mM for all solutions that contain the surfactant); an expected increase in zeta potential is observed over time. The 0.50 mM $CaCl_2$ solution (I = 11.68 mM) is replaced with a 1.00 mM $CaCl_2$ solution (I = 13.22 mM) that has a higher ionic strength but same 2NA content. Upon addition of the higher ionic strength solution, an initial increase in zeta potential is observed and is followed by a decay in surface charge over time. Similar

results are again seen when a 1.50 mM $CaCl_2$ solution (I = 14.74 mM) replaced the solution containing 1.00 mM $CaCl_2$. Stabilized relative absolute zeta potential values for solutions containing 0.50, 1.00 and 1.50 mM $CaCl_2$ are 7.50 ± 0.02, 7.58 ± 0.05 and 7.43 ± 0.03 mV (n = 15), respectfully. Changes in ionic strength appeared to only briefly perturb the equilibrated adsorption of bridged 2NA to the negatively charged surface after initial stabilization of zeta potential values occurs. It is likely that the primary Ca^{2+}/2NA layer forms on top of the negatively charged surface and stabilizes as indicated by unchanging zeta potential values in the presence of the 0.50 mM $CaCl_2$/1.00 mM 2NA solution. Increasing the concentration of Ca^{2+} counter ions did not cause additional 2NA to be directly bridged to the surface but rather caused the formation of an unstable secondary Ca^{2+}/2NA layer on top of the primary layer (Figure 2.11). Instability of the secondary Ca^{2+}/2NA layer caused desorption of the secondary

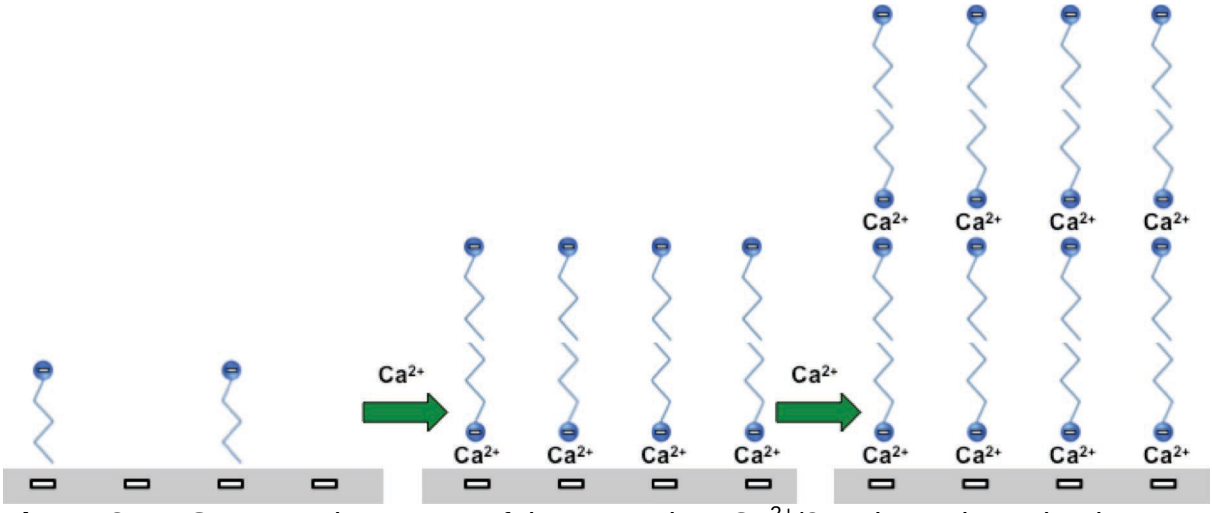

Figure 2.11. Suggested structure of the secondary Ca^{2+}/2NA layer that adsorbs following an increase in ionic strength of the sample solution

2NA molecules and a decrease in relative surface charge until insignificant quantities of secondary 2NA remain and zeta potential values return to that which were observed before the increase in ionic strength.

Conclusion

We have demonstrated that the effects of counter ions on surface charge correlate to the charge density and specific valence of cations. Decreases in relative absolute zeta potential values were shown to be greater as charge density increased ($K^+ < Na^+$; $Ca^{2+} < Mg^{2+}$) and as the valency of cations increased ($Na^+ < Ca^{2+}$). As expected, introduction of negatively charged 2NA caused a gradual increase in the surface charge of negatively charged PDMS that stabilized over time. Divalent Ca^{2+} has been previously suggested to partake in a bridging effect that facilitates the addition of surfactants to a negatively charged surface. We have observed dynamic changes in surface charge confirming that adsorption of 2NA to negatively charged PDMS is indeed partially controlled by the presence of Ca^{2+}. Following the formation of a stable Ca^{2+}/2NA layer on the surface additional adsorption of secondary Ca^{2+}/2NA, caused by an increase in ionic strength, is unstable and decays over time. The dynamic observations found within provide real-time evidence for the significance of cation bridging and also illuminate the potential mechanisms for controlling these interactions. These observations can be used to understand the fouling of surfaces by surfactants in the presence of divalent species. Future works should investigate the possibility of disrupting divalent cation bridging via competition of other cationic species that do not promote surfactant adsorption while having high affinity for the surface. Surfactant conjugation, functionalization and overall hydrophobicity should also be considered as possible characteristics for understanding the effectiveness of divalent cation bridging.

REFERENCES

1. Boussu, K.; Kindts, C.; Vandecasteele, C.; Van der Bruggen, B. *Chemphyschem* **2007**, *8*, 1836-1845.

2. Yu, S.; Zhang, X.; Li, F.; Zhao, X. *Colloids and Surfaces A.* **2017**, *518*, 130-138.

3. Kishimoto, N.; Kimura, H. *J. Water Reuse Desalin.* **2012**, *2*, 40-46.

4. Wang, X.; Lee, S. Y.; Miller, K.; Welbourn, R.; Stocker, I.; Clarke, S.; Casford, M.; Gutfreund, P.; Skoda, M. W. *Langmuir.* **2013**, *29*, 5520.

5. Austad, T.; Rezaeidoust, A.; Puntervold, T.; *Soc. Pet. Eng. J.*, 2010.

6. Lager, A.; Webb, K. J.; Collins, I. R. *Soc. Pet. Eng. J.* **2008**.

7. Li, Q.; Elimelech, M. *Environ. Sci. Technol.* **2004**, *38*, 4683-4693.

8. Mafi, A.; Hu, D.; Chou, K. C. *Langmuir* **2017**, *33*, 7940-7946.

9. Muneer, M.; Oades, J. *Soil Res.* **1989**, *27*, 411-423.

10. Allen, F. J.; Griffin, L. R.; Alloway, R. M.; Gutfreund, P.; Lee, S. Y.; Truscott, C. L.; Welbourn, R. J. L.; Wood, M. H.; Clarke, S. M. *Langmuir* **2017**, *33*, 7881-7888.

11. Pintea, S.; de Poel, W.; de Jong, A. E. F.; Vonk, V.; van der Asdonk, P.; Drnec, J.; Balmes, O.; Isern, H.; Dufrane, T.; Felici, R.; Vlieg, E. *Langmuir* **2016**, *32*, 12955-12965.

12. Delgado, A. V.; González-Caballero, F.; Hunter, R. J.; Koopal, L. K.; Lyklema, J. *Pure Appl. Chem.* **2005**, *77*.

13. Aveyard, R.; Haydon, D. A. *An Introduction to the Principles of Surface Chemistry*; *Cambridge University Press.*, 1973.

14. Parsons, R. *Chem. Rev.* **1990**, *90*, 813-826.

15. Carneiro-da-Cunha, M. G.; Cerqueira, M. A.; Souza, B. W. S.; Teixeira, J. A.; Vicente, A. A. *Carbohydr. Polym.* **2011**, *85*, 522-528.

16. Kirby, B. J.; Hasselbrink, E. F. *Electrophoresis.* **2004**, *25*, 187-202.

17. Tandon, V.; Bhagavatula, S. K.; Nelson, W. C.; Kirby, B. J. *Electrophoresis.* **2008**, *29*, 1092-1101.

18. Datta, S.; Conlisk, A. T.; Li, H. F.; Yoda, M. *Mech. Res. Commun.* **2009**, *36*, 65-74.

19. Pierre, A.; Lamarche, J. M.; Mercier, R.; Foissy, A.; Persello, J. *J. Dispersion Sci. Technol.* **1990**, *11*, 611-635.

20. Coreño, J.; Martínez, A.; Bolarín, A.; Sánchez, F. *J. Biomed. Mater. Res.* **2001**, *57*, 119-125.

21. Gustafsson, J.; Mikkola, P.; Jokinen, M.; Rosenholm, J. B. *Colloids Surf. A.* **2000**, *175*, 349-359.

22. Vrouwe, E. X.; Luttge, R.; Olthuis, W.; van den Berg, A. *J. Chromatogr. A.* **2006**, *1102*, 287-293.

23. Han, B.; Xu, Y.; Zhang, L.; Yang, X.; Wang, E. *Talanta.* **2009**, *79*, 959-962.

24. Ocvirk, G.; Munroe, M.; Tang, T.; Oleschuk, R.; Westra, K.; Harrison, D. J. *Electrophoresis.* **2000**, *21*, 107-115.

25. Berglund, K. D.; Przybycien, T. M.; Tilton, R. D. *Langmuir.* **2003**, *19*, 2714-2721.

26. Stroock, A. D.; Whitesides, G. M. *Electrophoresis.* **2002**, *23*, 3461-3473.

27. Abdallah, W.; Buckley, J. S.; Carnegie, A.; Edwards, J.; Herold, B.; Fordham, E.; Graue, A.; Habashy, T.; Seleznev, N.; Signer, C.; Hussain, H.; Montaron, B.; Ziauddin, M. *Oilfield Rev.* **2007**, *19*, 44–63.

28. Hilner, E.; Andersson, M. P.; Hassenkam, T.; Matthiesen, J.; Salino, P. A.; Stipp, S. L. S. *Sci. Rep.* **2015**, *5*, 9933.

29. Mampallil, D.; van den Ende, D.; Mugele, F. *Electrophoresis.* **2010**, *31*, 563-569.

30. Reyes, D. R.; Iossifidis, D.; Auroux, P.-A.; Manz, A. *Anal. Chem.* **2002**, *74*, 2623-2636.

31. Efimenko, K.; Wallace, W. E.; Genzer, J. *J. Colloid Interface Sci.* **2002**, *254*, 306-315.

32. Liu, Y.; Vickers, J. A.; Henry, C. S. *Anal. Chem.* **2004**, *76*, 1513-1517.

33. Huang, X.; Gordon, M. J.; Zare, R. N. *Anal. Chem.* **1988**, *60*, 1837-1838.

34. Pittman, J. L.; Henry, C. S.; Gilman, S. D. *Anal. Chem.* **2003**, *75*, 361-370.

35. Mark, J. E. *Polymer data handbook*; *Oxford University Press.*, 2009.

36. Kékicheff, P.; Marčelja, S.; Senden, T.; Shubin, V. *J. Chem. Phys.* **1993**, *99*, 6098-6113.

37. Guan, Q.; Noblitt, S. D.; Henry, C. S. *Electrophoresis.* **2012**, *33*, 2875-2883.

38. Badal, M. Y.; Wong, M.; Chiem, N.; Salimi-Moosavi, H.; Harrison, D. J. *J. Chromatogr. A.* **2002**, *947*, 277-286.

39. Garcia, C. D.; Dressen, B. M.; Henderson, A.; Henry, C. S. *Electrophoresis.* **2005**, *26*, 703-709.

40. Myers, D. *Surfactant science and technology*; John Wiley & Sons, 2005.

41. Guan, Q.; Noblitt, S. D.; Henry, C. S. *Electrophoresis.* **2012**, *33*, 379-387.

42. Negin, C.; Ali, S.; Xie, Q. *Petroleum.* **2016**.

43. Glenn, K. M.; Lucy, C. A. *Analyst.* **2008**, *133*, 1581-1586.

CHAPTER 3. MICROFLUIDIC DEVICES CONTAINING THIN ROCK SECTIONS FOR OIL RECOVERY STUDIES

While there has been a shift towards renewable energy sources, oil remains an important source of not only energy but also raw materials. Oil recovery is currently an inefficient process with as much as 50% of the original oil remaining in a field. Improvement of oil recovery techniques requires a model system that is both chemically and physically representative to achieve accurate results. Current large laboratory-scale systems use large cores drilled from target rock and large, high-pressure systems to recreate oil recovery systems. The cores and associated equipment required to accurately model oil recovery are expensive and time consuming to obtain and operate. As a result, there has been a continual quest to develop alternative solutions that are faster, less complicated, and less expensive while still providing accurate representation of reservoirs. An alternative to large-scale models are optically transparent two or three-dimensional microfluidic devices. Several examples of microfluidic devices used to study oil recovery processes have been published.[1-4] Unfortunately, most microfluidic devices require complicated fabrication techniques, inaccurately replicate the reservoir rock surface chemistry and geometry, and are made from materials not representative of surfaces found in oil reservoirs. Herein, the Flow On Rock Device (FORD) is described as an easy to fabricate microfluidic device that acts as a bridge between fully synthetic microfluidics and large laboratory models due to incorporation of reservoir rock samples directly into the microfluidic device. Results of flooding studies are presented on shale and sandstone models as an example of the potential for this system in

studying oil recovery. This project was funded by BP plc and has been accepted for publication pending minor revisions in *Microfluidics and Nanofluidics*.

Overview

The retrieval of crude oil from natural mineral deposits is a complex process, involving multiple recovery techniques. Fundamentally, oil recovery is controlled by a combination of the physical structures present in the rock (pore-throat geometries) as well as the chemistry of the rock and associated waters.[5,6] Oil recovery is achieved by displacing the oil with an immiscible fluid using primary and secondary recovery techniques. Primary recovery techniques utilize the naturally occurring pressure inherent to the reservoirs in combination with pumps to extract the crude oil. During the secondary oil recovery process, injections of water or gas are used to displace oil to force it from its reservoir. Despite the technological advances in primary and secondary recovery techniques, 50–60% of the original oil in place (OOIP) remains unrecovered in many reservoirs.[7,8] To improve OOIP recovery, enhanced oil recovery (EOR) techniques such as flooding with CO_2 and low salinity brine have been used.[7-10] EOR can significantly boost production and extend the production lifetime of a reservoir but increases the cost per barrel of oil produced and can take an upward of 10 yrs before a well location reaches full-scale deployment and productivity.[11,12] Despite the risks, well locations being targeted for EOR are distributed globally, and dissimilar geographical locations result in the variance of chemical and physical characteristics among oil reservoirs.[11] Improving the efficiency of EOR methods using accurate small-scale models would benefit production tremendously, reduce the risk of implementing these

strategies, and potentially allow for rapid investigation of more environmentally friendly methods of oil recovery.

To test EOR strategies, small-scale core flooding field studies have been performed.[7,12-16] In general, core flooding studies typically involve the injection of a displacement fluid into an oil-filled porous matrix. As displacement fluid is injected into the matrix it forces the oil out, which is now considered “recovered oil.” As the efficiency of the recovery strategy increases, the percentage of the OOIP that is recovered increases. Small-scale studies have shown the injection of CO_2 or diluted brine to be effective options for increasing the recovery of OOIP. Field studies offer the best predictability for the effectiveness of specific EOR strategies, but come at significant financial and time costs.[13,17]

Laboratory core flooding experiments, which inject fluid into cylindrical reservoir rock samples, are an important alternative to traditional field studies.[15,18] Conducting core flooding experiments in a laboratory reduces operational cost, decreases time required to obtain results and permits the testing of multiple EOR strategies. However, the large cores used in these experiments are expensive, require long equilibration times, and require specialized instrumentation for flow imaging due to the opaque nature of the rock cores. To further reduce the cost and time of developing an effective EOR strategy, alternative laboratory-based methods are needed.

Optically transparent microfluidic devices containing two-dimensional features that simulate the porous networks of oil reservoirs have been used to study oil recovery processes.[2-4,19-21] One of the most challenging aspects of generating these devices, however, is replicating the physical and chemical complexity found in natural rock. To

replicate the porous network, multiple approaches have been developed. One method involves digitally scanning the surface of a reservoir sample to produce a photomask for fabricating microstructures.[3] Other fabrication methods have utilized computational methods for channel design, followed by chemical etching, creation of packed beds of granular material or growing mineral crystals to replicate networks that resemble porous media.[3,22-24] Fabricating porous networks that simulate reservoir rock requires replication of the surface along with the use of materials that may not be chemically representative of real reservoir samples. Here, we report a microfluidic model to study oil recovery processes that incorporates reservoir rock directly into the device described herein as the Flow On Rock Device (FORD) as an alternative to previous methods. Design of the FORD and its fabrication method were developed with the goal of creating a simplistic, inexpensive and easy to produce microfluidic device capable of performing core flooding experiments using a variety of rock materials. Considering the desired characteristics of the FORD its fabrication method was designed to be carried out in a laboratory capable of soft lithography.

Experimental

FORD Fabrication

Semicircular sandstone and shale reservoir rock core samples with a diameter of 3 cm and thicknesses between 200–400 μm were provided by BP plc (Figure 3.1.A and 3.1.C). The varying surface morphologies of sandstone and shale were obtained using a ZeScope optical profilometer (Zygo, Middlefield, CT, US) and are shown in Figure 3.1.B and 3.1.D, respectively. Surface roughness values are given as Sq (root mean

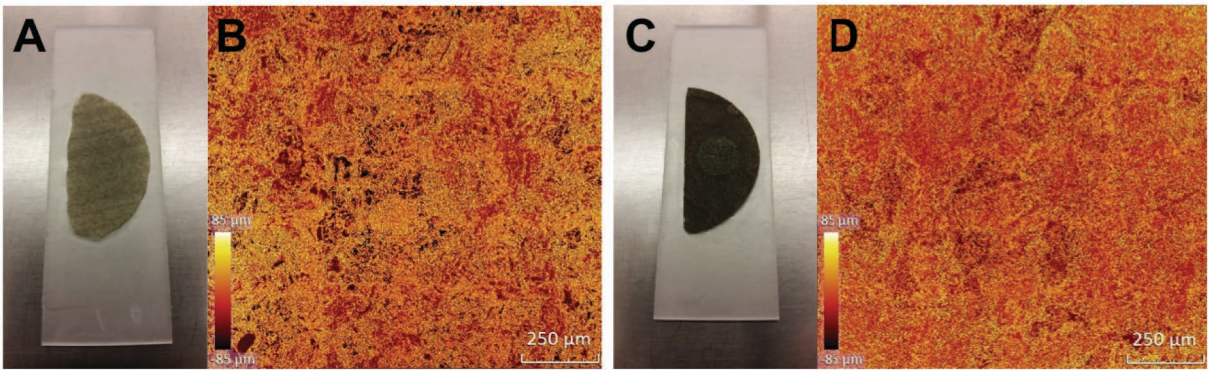

Figure 3.1 A and B) Sandstone sample mounted on a glass slide and an image of the sandstone sample's surface taken with optical profilometry. **C and D)** Shale sample mounted on a glass slide and an image of the sandstone sample's surface taken with optical profilometry

square height). Core samples received from BP plc arrived mounted on glass microscope slides using double-sided tape. To create the microfluidic device, a tape (Scotch Magic Tape™) well was built around a reservoir rock core sample (Figure 3.2.A). Next, a 10 mm diameter, 4 mm thick circular polydimethylsiloxane (PDMS) disk

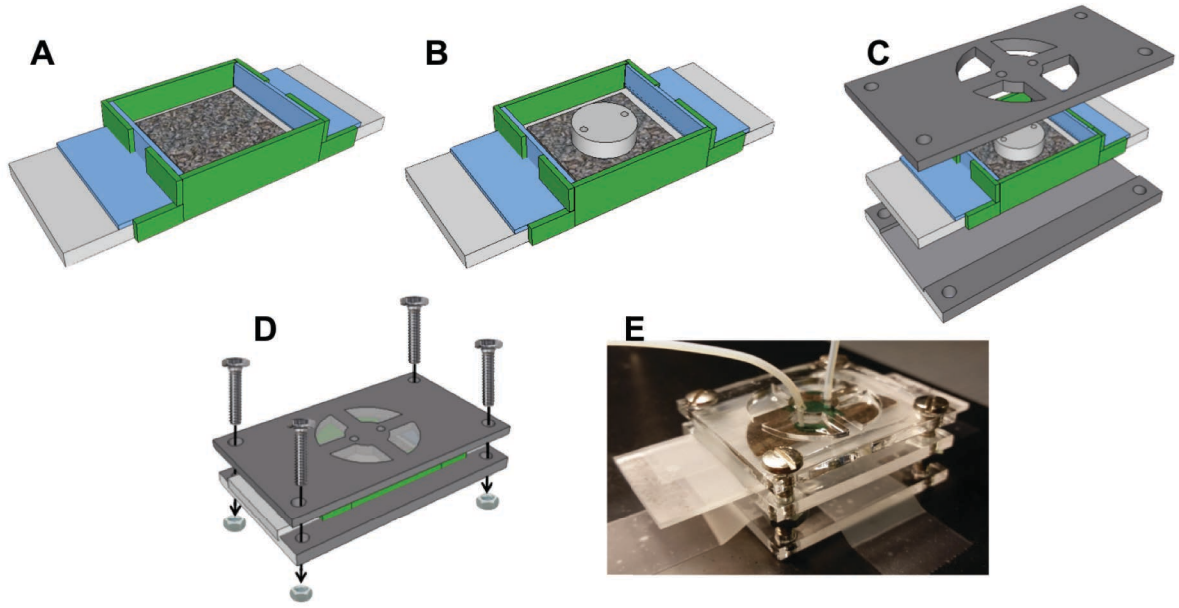

Figure 3.2 A–D) Illustration of the method to fabricate the FORD. **E)** Finished FORD

was generated from a sheet of cured PDMS using a biopsy punch (Robbins Instruments, Chatham, NJ). All PDMS was prepared with a prepolymer to curing agent

(Krayden Sylgard 184, Denver, CO) ratio of 10:1. Two 1.5 mm diameter inlet/outlet holes were punched 2 mm from the cylinder's outer edge using a biopsy punch (Figure 3.2.B). A laser cut (30 watt CO_2 Epilog Zing Laser, Golden, CO) holder used to position the glass slide during experiments and to hold the PDMS punch in place during core flooding experiments was cut from sheet polymethylmethacrylate (PMMA, Fort Collins Plastics) (Figure 3.2.C). Inlet/outlet tubing (Western Analytical Products, PTFE 0.020" ID x 1/16" O, Lake Elsinore, CA) was inserted by hand through the 1.5 mm diameter holes. 4 x 6-32 ¾" bolts were used to keep the holder together and were hand tightened. Next, 15 g of PDMS was prepared and partially cured for 14 min at 80 ˚C. The partially cured PDMS was poured around the PDMS cylinder and inlet/outlet tubing (Figure 3.2.D). The completed device was then allowed to cure for 24 hr at 60 ˚C before use (Figure 3.2.E).

Core Flooding

A 10 mL plastic syringe containing the aqueous green food dye (green food color, Great Value, Bentonville, AR) and a 10 mL glass syringe containing heavy mineral oil (Fisher Scientific, Fair Lawn, NJ) were attached to a three-way valve. The three-way valve was attached to the inlet tubing in the FORD. Two syringe pumps (New Era Pump Systems Inc, Farmingdale, NY) were used to control the flow rate of the syringes. To perform oil-wet experiments, mineral oil was pumped through device at 4 µL/min. Once the device was filled with mineral oil the pump was turned off and the device was allow to equilibrate for 1 hr. After equilibration, the pump for the green dye was started and the device was flooded with green dye at 4 µL/min. Typically, flow rates

stabilized after ~1 hr, which is about how long it took fluids to travel from the three-way valve to the device. Green dye was pumped through the device for 40 min after the breakthrough event occurred. Next, mineral oil was again pumped through device at 4 μL/min. For water-wet core flood experiments, aqueous green dye was used to initially flood the device, then mineral oil was pumped through the device followed lastly by green food dye again. Images illustrating fluids flowing in the FORD were abstracted from videos (15 frames/min) taken with a Dino-Lite handheld microscope (AM4112NT, Torrance, CA). All image analysis was performed using ImageJ software (National Institutes of Health). The dimensions of fingering events were assessed by randomly selecting 12 sets of fingers, followed by measuring the fingers using the ruler tool in ImageJ. The quantity of fingers per unit area was determined by manually counting the fingering events in 16 randomly selected areas.

It is important to mention that when core flooding experiments were carried out at 4 μL/min, flow occurred through the rock features and was easily observed. These flow rates are equivalent to superficial injection velocities as high as 4.01 ft/day in traditional core floods, which is considered within the normal flow rate range for core flooding experiments.[15,25,26] In contrast, when fluid was forcefully pumped through the FORDs at 1 mL/min, the flooding chamber bowed and fluid flowed over the rock surface (Figure 3.3).

Results and Discussion

Microfluidic devices capable of core flooding experiments currently involve recreation of a porous network to act as a matrix using materials common to

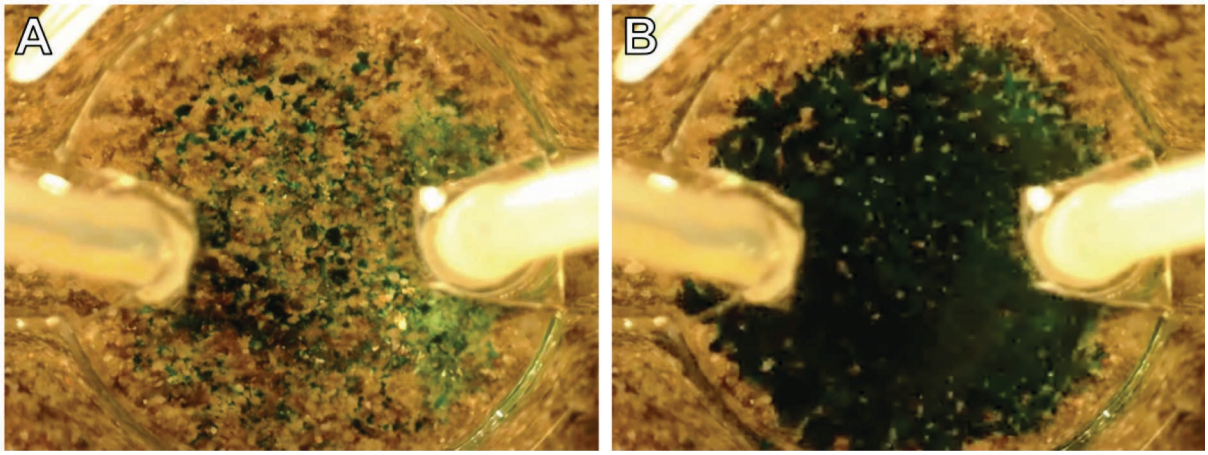

Fig 3.3 A) Aqueous green food dye flows through the rock sample in the device at 4 µL/min. **B)** Aqueous green food dye flows over the rock sample in the device when flow is increased to 1 mL/min

microfluidics. While these devices have been used for important studies of oil recovery processes, they have the potential to be chemically and/or physically dissimilar to actual reservoir rock.[22-24,27,28] Here, a straightforward fabrication method that integrates reservoir rock into a microfluidic as a bridge between fully synthetic microfluidic devices and core samples is presented. Figure 3.2 shows the steps involved in the fabrication process. Starting with reservoir rock thin sections mounted on a microscope slide, a tape well was built around the rock sample to contain the PDMS that would seal the flooding chamber (Figure 3.2.A). To act as the conformal layer of the FORD device, a PDMS disk containing fluidic ports was positioned on the rock and held in place using a laser cut compression device (Figure 3.2.B). PDMS is readily accessible in many laboratories and is easy to work with, making the method useful for broad adaptation. A laser cut portion of PMMA was then used to hold the PDMS cylinder on the surface of the rock sample (Figure 3.2.C). Uncured PDMS was poured around the PDMS cylinder to create the flooding chamber and seal the device without the use of high heat, plasma treatment, or chemical adhesives (Figure 3.2.D). Sealing the chamber in this manner

minimizes chemical alteration to the rock's surface. It should be noted that the FORD fabrication process requires instrumentation and materials found in many laboratories. The hands-on portion of the fabrication process requires approximately 45 min.

After developing the fabrication method, core flooding experiments were performed. By definition, two opposing states are defined in oil recovery studies, water-wet and oil-wet.[27] If an aqueous phase is in contact with the surface and the contact angle is small ($\theta < 60^{o}$), the surface is defined as water-wet. If the aqueous phase contacts the surface at a larger angle ($\theta > 120^{o}$) and/or oil is in contact with the surface, the surface is defined as oil-wet. Contact angles that exist between these two parameters define a wettability state defined as intermediate- or mixed-wet.[27,29,30] For the purposes of these proof-of-concept studies, water-wet and oil-wet samples were tested. Within the FORD, wettability was selected by exposing a surface first to either aqueous dye or mineral oil creating a water-wet or oil-wet surface, respectively [31]. By using mineral oil and aqueous dye fluids, differences in core floods due to initial wetting conditions can be observed.[6,30] Under water-wet conditions both sandstone and shale FORDs exhibited movement of a flat displacement front when mineral oil is pumped into the device (Figure 3.4). When aqueous dye is again pumped through the device to displace the oil, small fingering breakthrough events are observed with no evidence of a flat displacement front. The small fingering events could not be quantified in this work due to the magnification required to observe the entire flooding chamber during experimentation. In the future, alternative imaging methods that can quantify the fingering will be developed. The water fingers travel almost exclusively towards the flooding chamber's outlet and residual mineral oil can be observed in the rock's pores

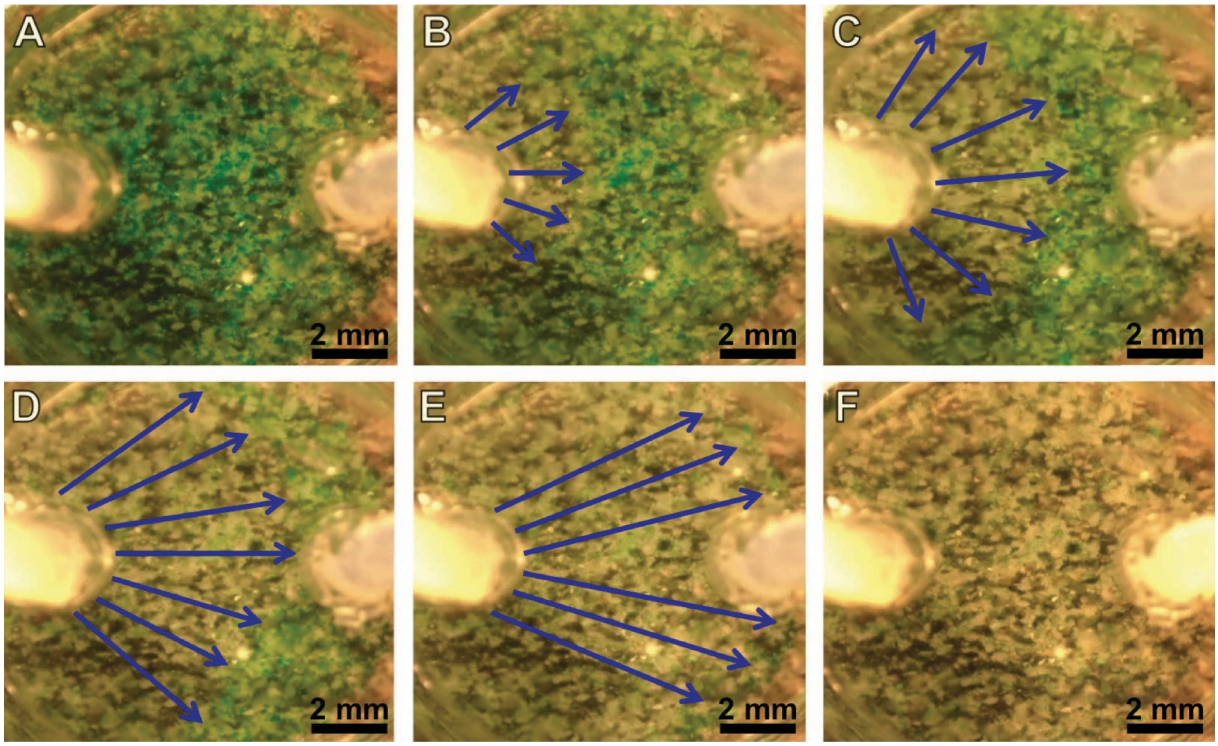

Figure 3.4 A) FORD is initially flooded with green food dye at 4μL/min. **B–E)** FORD is progressively flooded with mineral oil to displace green food dye. A flat displacement front is observed and indicated with blue arrows. **F)** The mineral oil phase has finished displacing the green food dye

(Figure 3.5). Under oil-wet conditions, both sandstone and shale FORDs display initial fingering events instead of a flat displacement front when aqueous dye is used for flooding (Figure 3.6). The higher surface roughness of the sandstone samples (sandstone, S_q = 25.86 ± 0.70 μm; shale, S_q = 18.65 ± 0.13 μm) result in pronounced fingers that are 84 ± 13 μm wide (n=12); drops of aqueous dye spanning multiple pores are also observed with diameters of 296 ± 85 μm (n=12) (Figure 3.7.B). Shale samples exhibit fingers that are 58 ± 11 μm (n=12) wide, as well as aqueous drops that are 170 ± 38 μm (n=12) in diameter. Not only does shale exhibit a decrease in the finger width compared to sandstone but also a visible increase (sandstone = 2.4 ± 0.5 fingers/mm^2,

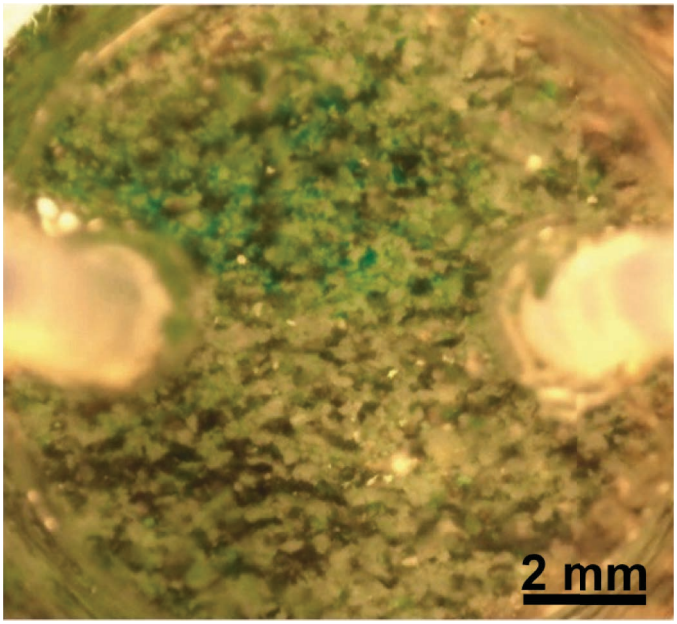

Figure 3.5 Under water-wet conditions aqueous green food dye is pumped through the FORD to displace mineral oil. Green food dye is observed to travel almost exclusively towards the outlet.

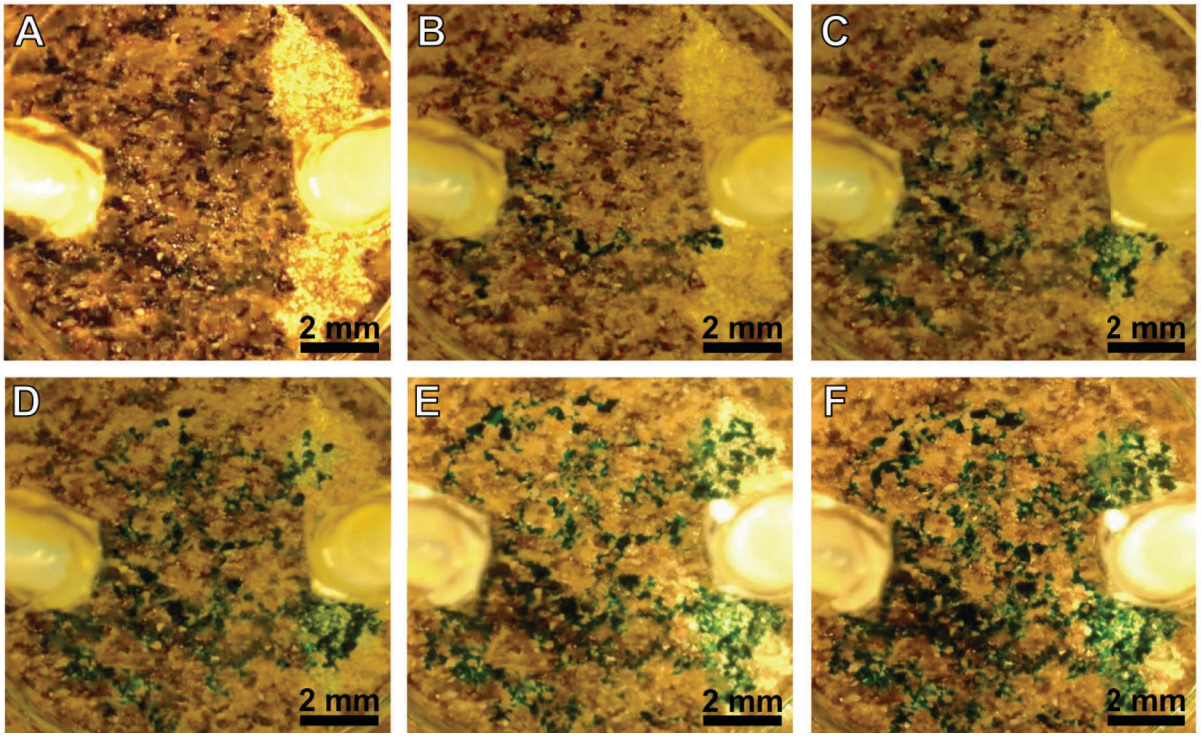

Figure 3.6 A) FORD is initially flooded with mineral oil at 4µL/min. **B–F)** FORD is progressively flooded with green food dye to displace mineral oil. Fingering events are observed

shale = 5.4 ± 0.7 fingers/mm^2, n = 16) in the relative number of fingering events (Figure 3.7.E).

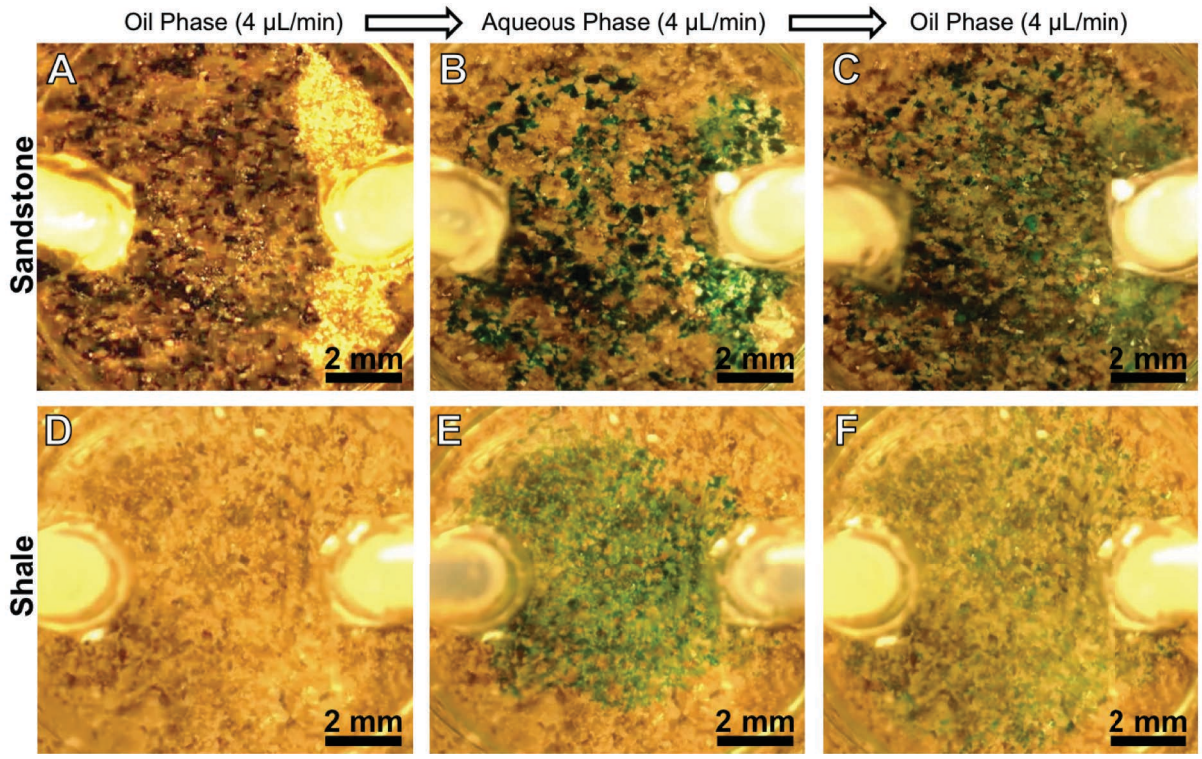

Figure 3.7 A and **D)** Initial flood with mineral oil at 4 µL/min. In 6a the right side of the flooding chamber has not been completely wetted with oil prior to displacement. **B** and **E)** Green food dye is pumped into device at 4 µL/min to displace mineral oil. **C** and **F)** Mineral oil is pumped into device at 4 µL/min to displace green food dye

It is important to note that only model fluids have been tested in the FORD. To fully assess the utility of the FORD, consideration should be given to the compatibility of the device with potential EOR strategies. Due to the chemical and solubility characteristics of PDMS, testing EOR strategies that involve caustic or organic solvent should be avoided [32]. While it is unfortunate that these fluids cannot be used within the FORD, fluids with these characteristics should also be avoided when using existing microfluidics capable of core flooding. If thermal EOR strategies are sought, heating of the FORD above 250 ˚C should be avoided to prevent thermal degradation.[33] Failure as a result of internal pressure within the FORD was not thoroughly investigated but fluid injection velocities of 1 mL/min were found to cause the PDMS layer to bow, which

resulted to fluid flowing over instead of along the rock sample's features. Because of this, it can be assumed that high internal pressures will likely cause undesirable flow above the rock sample before the device reaches an internal pressure that causes it to critically fail. With any analytical tool there are limitations to consider and the FORD is no exception. Despite the incompatibility of some EOR strategies with the FORD, there are still many core flooding methods that can be investigated.

Two-dimensional micromodels capable of carrying out immiscible visual and non-visual core flooding experiments can be found in the literature.[22-24,34-38] Similar to the FORD and naturally occurring reservoir rock, existing micromodels can contain diverse distributions of pore sizes between 100 and 1000 μm and have shown differences in flooding behavior due to initial wetting conditions.[23,24,35,37,38] Other phenomena like capillary fingering, trapped residual non-wetting fluid and variations in displacement fluid fronts occur in both current micromodels and the FORD.[15,21,23,24] Although similar results are seen, observations within the FORD potentially provide additional information and are more representative of flooding that occurs within a reservoir due to the use of actual reservoir rock and thus represents an important bridge between fully synthetic microfluidic devices and traditional core floods.

Conclusion

We have designed and fabricated a microfluidic device called the Flow On Rock Device (FORD) that incorporates naturally occurring reservoir rock core samples into microfluidic devices for studying oil recovery. Because the FORD utilizes reservoir rock samples, design and fabrication of complex porous two-dimensional networks using

microfabrication is unnecessary. Another benefit of the FORD lies in its simplistic fabrication process that involves three simple steps and less than 45 min of active labor. The FORD also requires no chemical, plasma or intense heat treatment to form a sealed microfluidic device, minimizing unintended chemical modifications to the rock. Core flooding experiments were successfully performed using both sandstone and shale to demonstrate the broad applicability. The FORD successfully illustrated the predictable differences in behavior due to initial wetting conditions in flooding experiments and exhibited common phenomena like capillary fingering, trapped residual non-wetting fluid and variations in displacement fluid fronts.[23,24] The difference of fingering events that occur on sandstone and shale illustrates the need to model core flooding using porous networks that are specific to the field sites targeted for EOR. Moving forward we will perform core flooding experiments that include fluids that are typically used in EOR and study the impact of the presence of ionic species with the goal of improving oil recovery efficiency.

REFERENCES

1. Song, W.; Kovscek, A. R. *Lab Chip* **2015**, *15*, 3314-3325.

2. Lee, H.; Lee, S. G.; Doyle, P. S. *Lab Chip* **2015**, *15*, 3047–3055.

3. Gunda, N. S.; Bera, B.; Karadimitriou, N. K.; Mitra, S. K.; Hassanizadeh, S. M. *Lab Chip* **2011**, *11*, 3785–3792.

4. Wang, W.; Chang, S.; Gizzatov, A. *ACS Appl. Mater. Interfaces* **2017**, *9*, 29380–29386.

5. Terry, R. E. In *Encyclopedia of Physical Science and Technology*; Academic Press: New York, 2001, pp 503–518.

6. Buckley, J. S., Office, N. P. T., Ed., 1998.

7. Ali, S. M. F.; Thomas, S. *J. Can. Pet. Technol.* **2000**, *39*, 7–11.

8. Alvarado, V.; Manrique, E. *Energies* **2010**, *3*, 1529–1575.

9. Nobakht, M.; Moghadam, S.; Gu, Y. *Energy Fuels* **2007**, *21*, 3469–3476.

10. Zekri, A.; Jerbi, K. K. *Oil Gas Sci. Technol.* **2002**, *57*, 259–267.

11. Mullins, O. C.; Zuo, J. Y.; Wang, K.; Hammond, P. S.; De Santos, R.; Dumont, H.; Mishra, V. K.; Chen, L.; Pomerantz, A. E.; Dong, C. L.; Elshahawf, H.; Seifert, D. J. *Petrophys.* **2014**, *55*, 96–112.

12. Lager, A.; Webb, K. J.; Collins, I. R. *Soc. Pet. Eng. J.* **2008**.

13. McGuire, P. L.; Chatham, J. R.; Paskvan, F. K.; Sommer, D. M.; Carini, F. H. *Soc. Pet. Eng. J.* **2005**.

14. Nasralla, R. A.; Alotaibi, M. B.; Nasr-El-Din, H. A. *Soc. Pet. Eng. J.* **2011**.

15. Rivet, S. M.; Lake, L. W. *Soc. Pet. Eng. J.* **2010**.

16. Tarvin, J. A.; Gustavson, G.; Balkunas, S.; Sherwood, J. D. *J. Pet. Sci. Eng.* **2008**, *61*, 75–87.

17. Sevin, J.; Capron, B. *Energy Perspectives* **2013**.

18. Boussour, S.; Cissokho, M.; Cordier, P.; Bertin, H.; Hamon, G. *Soc. Pet. Eng. J.* **2009**.

19. Berejnov, V.; Djilali, N.; Sinton, D. *Lab Chip* **2008**, *8*, 689–693.

20. Berejnov, V.; Bazylak, A.; Sinton, D.; Djilali, N. *J. Electrochem. Soc.* **2010**, *157*, B760.

21. Ng, K. M.; Davis, H. T.; Scriven, L. E. *Chem. Eng. Sci.* **1978**, *33*, 1009–1017.

22. Kim, M.; Sell, A.; Sinton, D. *Lab Chip* **2013**, *13*, 2508–2518.

23. Zhang, C.; Oostrom, M.; Wietsma, T. W.; Grate, J. W.; Warner, M. G. *Energy Fuels* **2011**, *25*, 3493–3505.

24. Tanino, Y.; Akamairo, B.; Christensen, M.; Bowden, S. A. In *Proceedings of the International Symposium of the Society of Core Analysts*; Society of Core Analysis, 2015.

25. Pope, G. A. *Center for Petroleum and Geosystems Engineering* **2007**.

26. McCool, C. S.; Green, D. W.; Willhite, G. P.; Soc. Pet. Eng., 2000.

27. Abdallah, W.; Buckley, J. S.; Carnegie, A.; Edwards, J.; Herold, B.; Fordham, E.; Graue, A.; Habashy, T.; Seleznev, N.; Signer, C.; Hussain, H.; Montaron, B.; Ziauddin, M. *Oilfield Rev.* **2007**, *19*, 44–63.

28. Grate, J. W.; Dehoff, K. J.; Warner, M. G.; Pittman, J. W.; Wietsma, T. W.; Zhang, C.; Oostrom, M. *Langmuir* **2012**, *28*, 7182–7188.

29. Lenormand, R. *J. Phys. Condens. Matter* **1990**, *2*.

30. Schneider, M.; Osselin, F.; Andrews, B.; Rezgui, F.; Tabeling, P. *J. Pet. Sci. Eng.* **2011**, *78*, 476–485.

31. Buckley, J. S.; Liu, Y.; Monsterleet, S. **1998**.

32. Lee, J. N.; Park, C.; Whitesides, G. M. *Anal. Chem.* **2003**, *75*, 6544-6554.

33. Camino, G.; Lomakin, S. M.; Lazzari, M. *Polymer* **2001**, *42*, 2395-2402.

34. Keller, A. A.; Blunt, M. J.; Roberts, A. P. V. *Transp. Porous Media* **1997**, *26*, 277–297.

35. Sayegh, S. G.; Fisher, D. B.; Petroleum Society of Canada, 2009.

36. Sohrabi, M.; Danesh, A.; Jamiolahmady, M. *Transp. Porous Media* **2008**, *74*, 239–257.

37. Li, W.; Vigil, R. D.; Beresnev, I. A.; Iassonov, P.; Ewing, R. *J. Colloid Interface Sci.* **2005**, *289*, 193–199.

38. Corapcioglu, Y. M.; Chowdhury, S.; Roosevelt, S. E. *Water Resour. Res.* **1997**, *33*, 2547–2558.

CHAPTER 4. SELECTIVE DISTANCE-BASED K^+ QUANTIFICATION ON PAPER-BASED MICROFLUIDICS

In this study, paper-based microfluidic devices (μPADs) capable of K^+ quantification in aqueous samples, as well as in human serum, using both colorimetric and distance-based methods are described. A lipophilic phase containing potassium ionophore I (valinomycin) was utilized to achieve highly selective quantification of K^+ in the presence of Na^+, Li^+ and Mg^{2+} ions. Successful addition of a suspended lipophilic phase to a wax printed paper-based device is described and offers a solution to current approaches that rely on organic solvents which damage wax barriers. The approach provides an avenue for future alkali/alkaline quantification utilizing μPADs. Colorimetric spot tests allowed for K^+ quantification from 0.1–5.0 mM using only 3.00 μL of sample solution. Selective distance-based quantification required small sample volumes (6.00 μL) and gave responses sensitive enough to distinguish between 1.0 and 2.5 mM of sample K^+. μPADs using distance-based methods were also capable of differentiating between 4.3 and 6.9 mM K^+ in human serum samples. Distance-based methods required no digital analysis, electronic hardware or pumps; any steps required for quantification could be carried out using a naked eye. This work has been published in the ACS journal *Analytical Chemistry* (**2018**, *90* (7), pp 4894–4900).

Overview

Alkali and alkaline earth metals like K^+, Na^+ and Ca^{2+} ions are known to impact human and crop health.[1,2] Prolonged inadequate biological availability of these elements in food and drinking water can lead to many complications involving the

neurological, metabolic, and skeletal systems in animals.[3,4] Crops grown in soils without sufficient quantities of K^+ give rise to plants with poor health and decreased production.[5] A portion of a population's ability to function as a healthy society is dependent on food production, potable water availability, and adequate nutrition. Beyond food and water, precise measurement of these metals is also pertinent for human health and can be critical for successful recovery in medical settings.[6,7] Considering that alkali/alkaline earth metals contribute significantly to both human and plant health, the quantification of these metals can be considered essential to maintaining a healthy population.

Current systems for quantifying alkali/alkaline metals involve colorimetric or electrochemical methods. Unfortunately, performing analysis using electrochemical methods necessitates instrumentation that requires a power source. Electrochemical methods also often require trained professionals to successfully quantify ion concentrations. Microfluidic paper-based analytical devices (μPADs) capable of electrochemical detection have been employed to partially circumvent the limitations of traditional electrochemical systems;[8,9] these devices can be disposable, are less expensive, possess reasonable portability, ease of usability, reasonably low detection limits and even passive solution pumping. However, μPADs utilizing electrochemical methods are also limited by the requirements of traditional electrochemical instrumentation that include the need for trained professionals and powered hardware. μPADs designed for use in developing regions would ideally be simple and electronic free to increase portability and ease-of-use. Paper-based quantification methods utilizing colorimetry offer an instrument free approach that cannot be achieved with traditional quantification techniques.[10-12]

Recent publications have shown that colorimetric and distance-based methods have the capacity to successfully quantify metals using μPADs.[13,14] Colorimetric methods rely on color changes that occur because sensing molecules react with the analyte in question; generally, more color change is equated to more analyte. Some devices exhibit color changes that are capable of being monitored using the naked eye which increases portability but at the cost of limiting assay sensitivity.[15] The full capability of colorimetric devices is realized when the color change is digitally scanned/photographed then analyzed using image processing software but this approach requires hardware and electronics.[12,16]

Distance-based μPADs depend on changes in color or fluorescence along a channel that contains sensing molecules.[14,17-19] As sample travels along the channel, the sensing molecules on the channel consume analyte causing a color change. After the analyte has been consumed no more color change occurs even though the sample solution continues to travel along the channel. The distance at which the color/fluorescence change ends can be correlated to analyte concentration. Distance-based methods offer the ability to perform single step analysis since quantification of analyte in samples does not require any additional image analysis or external analysis equipment like in the case of colorimetric-based devices or electrochemical methods. Both colorimetric and distance-based detection methods for alkali/alkaline metals in μPADs exhibit the advantages of paper-based devices while not containing components that would require advanced training to operate. However, distance-based quantification requires no additional hardware or instrumentation thus increasing portability and facilitating deployment to regions without access to additional technologies.

Many examples involving the quantification of transition metals on μPADs have been published,[14,20] however, there are few reports involving the colorimetric or distance based-detection of alkali/alkaline metals on paper. Given that alkali/alkaline metals affect human and environmental health, there is certainly a desire for portable, inexpensive quantification methods but a lack of μPAD compatible sensing materials has thwarted development of these devices. Sensing materials like potassium ionophore I, sodium ionophore IV and calcium ionophore IV have been shown to be highly selective for their respective metal ions.[21-24] Some of these ionophores are naturally occurring compounds with specific ion binding motifs that provide high specificity but are limited in applications due to their hydrophobicity and required lipophilic solvents. Addition of lipophilic sensing reagents to μPADs requires that the interactions between the lipophilic phase and the hydrophobic barrier be minimized due to the lipophilic solvent's ability to dissolve the hydrophobic wax barrier that is commonly utilized to fabricate μPADs.[25,26] Additionally, sensing components that require a lipophilic solvent like THF cannot be used due to the quantity of sensing component that is lost to the hydrophobic barrier. For these reasons, ionophores can normally not be used to directly quantify species of interest in aqueous samples using μPADs. However, publications involving optode nanosensors have provided a functional method to bypass the hydrophobic characteristics of ionophores by suspending a lipophilic organic phase that contains ionophores and other sensing components in H_2O as microemulsions.[27-30]

Optode nanosensors are classified as organic spheres that are suspended in an aqueous solution and act as optical sensors.[27] The nanosphere-sized organic phase

droplets function as a reaction vessel containing sensing species that would not normally dissolve in an aqueous phase. Instead of trying to bring the lipophilic sensing components into the aqueous phase where the metal ion analyte is present, the optode transports the analyte into the organic phase interior of the nanosphere. Transportation of the ionic analyte from the aqueous to the organic phase is performed by the ionophore species giving rise to high selectivity.[31] To balance the positively charged metal ions that are brought into the optode, an ion exchanger is employed that will transfer cations to the surrounding aqueous phase to retain electrical neutrality. Continued consumption of the metal ion analyte results in the depletion of the ion exchanger and a positively charged species must still be removed for the organic phase to retain its net charge of zero. A chromoionophore present in the optode becomes deprotonated to accommodate for the sustained consumption of the metal ion analyte and depleted ion exchanger. Upon deprotonation, this chromoionophore will visually change color. The resulting color change in solution indicates a titration endpoint that is largely dictated by the ion exchanger loaded into the organic phase. Aqueous solutions containing suspended optodes have been shown to selectively quantify alkali/alkaline metals in biologically and environmentally relevant concentrations.[32-35]

Optodes offer a unique functionality that takes advantage of the selectivity of ionophores while circumventing their hydrophobicity. With this in mind, we have created μPADs that utilize the organic nanospheres as a tool to deposit the sensing components during fabrication while retaining the lipophilic phase's ability to selectively quantify K^+ metal ions. Wang *et al.* demonstrated that lipophilic solutions, based on chemistry previously explored by Xie *et al*., containing ionophores can be added to portions of

paper and possess the ability to colorimetrically quantify Na^+ in sample solutions.[27,33] However, the requirement of using THF as the lipophilic solvent instead of suspending the organic phase as nanospheres in H_2O prevented the ionophores from being used in μPADs. We have found that suspension of the organic phase in H_2O allows for the evaporation of incompatible THF before depositing the spheres on paper and circumvents the lipophilic solvent requirement. To the best of our knowledge, optode materials have not been utilized in μPADs that operate using distance-based methods to quantify alkali/alkaline metals. Herein we have described wax printed μPADs that employ colorimetric and distance-based methods to selectively quantify relevant K^+ concentrations in aqueous solutions.

Experimental

Materials and Equipment

Potassium ionophore I, chromoionophore I (CH1), sodium tetrakis[3,5-bis(trifluoromethyl) phenyl]borate (NaTFPB), Pluronic F-127, bis(2-ethylhexyl)sebacate (dioctyl sebacate, DOS, ≥97% purity), tetrahydrofuran (THF, anhydrous, ≥99.9% purity), potassium chloride (≥99.0% purity), sodium chloride (≥99.5% purity), lithium chloride (≥99.0% purity), magnesium chloride hexahydrate (99% purity), sodium hydroxide (≥97% purity), tris(hydroxymethyl)aminomethane and concentrated hydrochloric acid (HCl) were acquired from Sigma-Aldrich® (St. Louis, MO) and used without further purification. Level 1 and level 2 control serum was acquired from Pointe Scientific, Inc. (Canton, MI), was reconstituted using 5 mL of 18.2 MΩ*cm water, and used without further purification. Pointe Scientific, Inc. provided values for K^+ concentration in serum

samples. Aqueous solutions were prepared in 18.2 MΩ*cm water from a Millipore Milli-Q® purification system (Millipore, Billerica, MA). Whatman™ No. 4 qualitative-grade filter paper was purchased from GE Healthcare UK Limited (Buckinghamshire, UK). CorelDraw® software was used to design the hydrophobic wax barrier for all fabricated devices. Hydrophobic wax barriers were printed on filter paper using a commercial wax printer (Xerox Colorqube® 8870). Devices were sealed using Scotch™ heavy duty packaging tape purchased from 3M® (St. Paul, MN). Photographs for colorimetric analysis were taken using a Motorola Z Play cellphone and homemade light box. ImageJ software (National Institutes of Health) was used for image analysis.

Nanosphere synthesis

Potassium ionophore I (7.85 mg), NaTFPB (1.78 mg), CH1 (0.75 mg), Pluronic F-127 (5.0 mg) and DOS (6–8 mg) were dissolved in 3.0 mL of THF; this solution will hereafter be referred to as the "cocktail." 1.5 mL of H_2O was vortexed at 1000 rpm and 0.5 mL of the cocktail solution was injected into the H_2O via pipette. Compressed air (~ 8 psi) was blown into the vial containing the nanosphere suspension for 70–80 mins to evaporate THF and concentrate the suspension until the remaining solution weighed 60% of the initial injected cocktail's mass.

Dynamic Light Scattering

Dynamic light scattering (DLS) measurements were performed with a ZetaNano ZS (Malvern Instruments Ltd., Worcestershire, UK) device equipped with a He/Ne laser operating at 633 nm as a light source and an avalanche photodiode as a detector. The

experiments were carried out at a scattering angle of 173° in standard plastic cuvettes. The hydrodynamic radii were calculated from the average of 5 individual measurements for which each correlation function was accumulated for 20 s. The translational diffusion coefficients were obtained from the correlation functions using the second order cumulant fit.[36] Concentrated optode suspensions contained nanosphere particles 178 ± 3 nm in diameter with a polydispersity index of 0.071.

μPAD Fabrication

To create a hydrophobic barrier, pieces of Whatman™ No. 4 filter paper containing a wax printed design were placed design side down on a 150 ˚C hotplate for 90 s. A single 4” x 5” x 1/8” piece of aluminum was placed on top of the filter paper to ensure the paper kept conformal contact with the hotplate. For distance-based devices, portions of the devices designated to be reservoirs were removed using a 4 mm punch. The nanosphere suspension used for detection was pipetted onto colorimetric and distance-based devices using 6 x 0.75 μL and 5 x 5 μL aliquots respectively. Devices were dried for 90 s between applied aliquots using compressed air. For distance-based devices a single piece of packing tape was used to seal the top of the device followed by one reservoir space being removed using a 4 mm punch to allow for sample injection. Three layers of packing tape were applied to the backs of both colorimetric and distance-based devices to seal the device and provide rigidity.

K^+ Quantification and Metal/pH Interference Studies

Colorimetric and distance-based K^+ detection was carried out using 3.00 and 6.00 µL of sample respectively. Colorimetric-based devices were photographed after having been exposed to sample solutions for 5 min. The length of region that changed color in distance-based devices was measured 5 min after injection of sample using a standard metric ruler. Metal interference studies using Na^+, Li^+ and Mg^{2+} were all performed using 100.0 mM concentrations that were present concurrently with the K^+ sample. pH interference studies were carried out using solutions containing 5.0 mM KCl, 10.0 mM Tris and HCl to adjust the pH to 6, 7 and 8 (9.9, 9.3 and 5.6 mM HCl, respectively).

Image Analysis

All image analysis was carried out using ImageJ software. Images were processed by separating the color channels into red, green and blue. The red channel was used to quantify the colorimetric changes that resulted from the addition of sample solutions. The mean pixel intensity of device spots was determined using ImageJ software tools to create analysis zones that were perfectly circular and 150 image pixels in diameter. Mean pixel intensities were imported into Excel (14.6.0, Microsoft®) for analysis. The colorimetric titration curve in Figure 4.3 was acquired by smoothing data using GRAMS/AI™ software (Thermo Fisher® Scientific).

Results and Discussion

Colorimetric-Based Detection

A few recent examples of detection and quantification of alkali earth metals in aqueous samples have been published using colorimetric methods;[32,33] however, these recent methods are either incompatible with μPADs or involve a multilayered μPAD. With simplicity in mind, addition of nanosphere suspensions to wax printed paper-based spot devices was initially accomplished using one 5.00 μL aliquot followed by allowing the H_2O to evaporate until the device was dry. Although the organic nanospheres are present in the H_2O solution, evaporation of the H_2O causes the organic phase to deposit on the paper as a bulk phase. Wang *et al*. previously showed that the bulk organic phase is capable of K^+ quantification suggesting that suspended nanospheres act purely as a vehicle that facilitates deposition of the organic phase onto a μPADs.[33] The resulting device, which contained the organic sensing phase, allowed for K^+ detection in the range of 0.1–5.0 mM using 3.00 μL of solution sample and a logarithmic fit was applied which gave a R^2 value of 0.986 (Figure 4.1.A, n = 5). 10.0 mM K^+ was also tested in these devices but there was no color change between 5.0 and 10.0 mM suggesting that the device was saturated beyond 5.0 mM K^+, which is common with colorimetric μPADs.[37,38] Detection spots exhibited the “coffee ring” effect (Figure 4.1.B) making naked-eye detection difficult due to non-homogeneous color change.[19,39] To minimize the coffee ring effect, 6 x 0.75 μL (4.50 μL total) aliquots of the nanosphere suspension were pipetted on to the spots and were allowed to dry between suspension applications (Figure 4.1.C). Total drying time was increased to 9 mins from 5 mins when using the multiple aliquot method instead of a single aliquot method. Multiple low

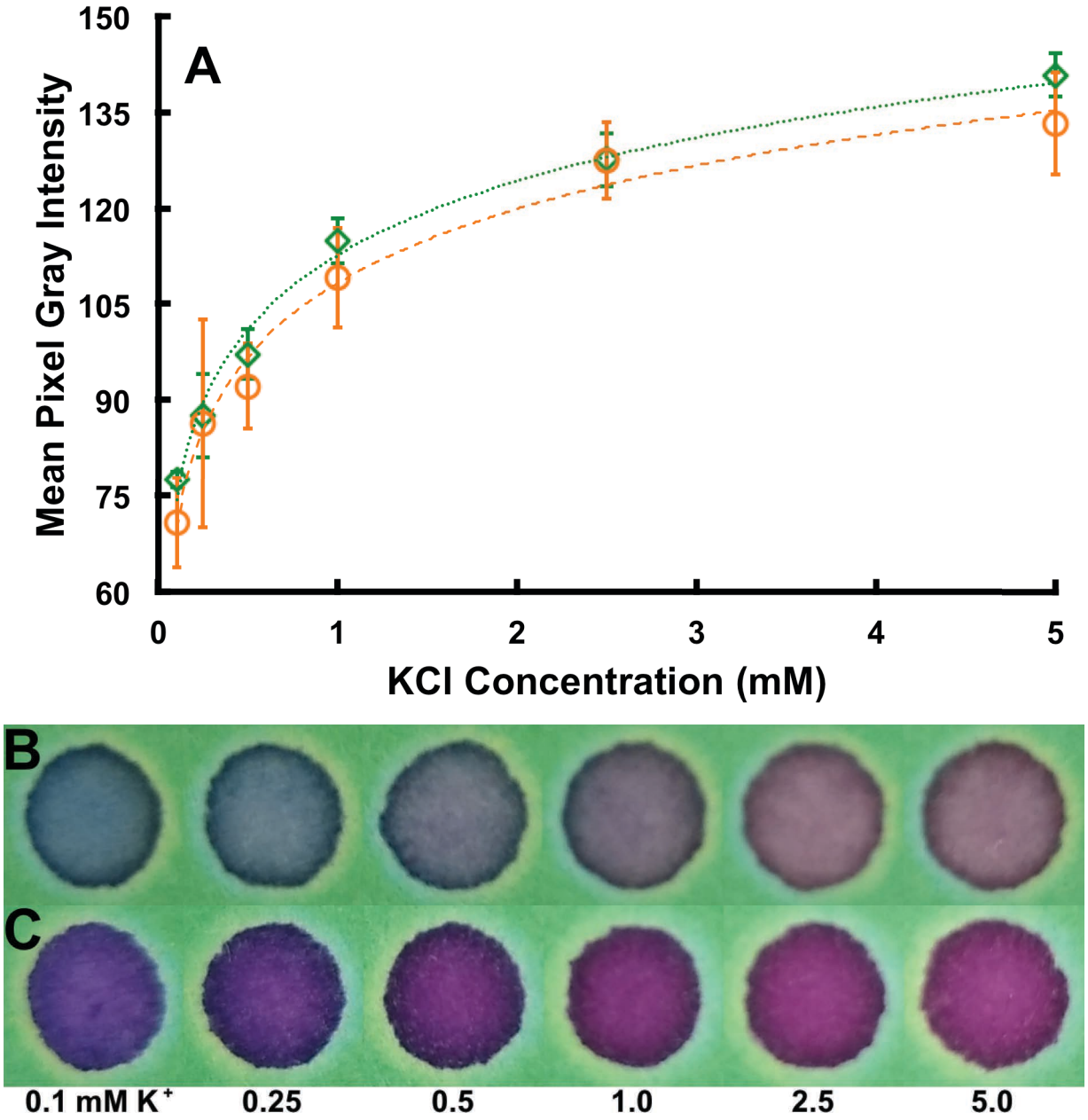

Figure 4.1. A) Calibration curve for spots with the coffee ring effect (orange) and spots without rings (green). **B)** Colorimetric spot tests that exhibit the "coffee ring" effect and were fabricated using a single aliquot of the sensing phase suspension. **C)** Colorimetric spot tests exhibiting homogeneous sensing phase distribution via multiple applied aliquots

volume aliquots provided detection spots with a seemingly homogeneous distribution of the lipophilic phase on the surface. K^+ detection performed using spots that did not have the coffee ring effect gave smaller error bars when compared to spots that possessed

the rings (Figure 4.1.A, R^2 = 0.988, n = 5). It should be noted that K^+ concentrations are quantified using only 3.00 µL of sample solution meaning that relatively small sample volumes are required to analysis.

Distance-Based Detection

Quantification of alkali/alkaline earth metals in µPADs has been previously reported via the use of colorimetric methods but require an external camera and software for analysis that limit portability and simplicity.[40-42] To further increase portability, minimalism, and usability in regions with limited infrastructure a distance-based µPAD was designed that costs ~$0.70 (plus fabrication labor) per assay. Our distance-based devices were shown to be effective at quantifying 1.0–10.0 mM of K^+ using 6.00 µL of aqueous sample (Figure 4.2). Quantification of K^+ was carried out using distance-based devices designed to have channels that were 30 mm long and 1 mm wide; paper portions of the device on either end of the channel were also removed so the channel ended at hydrophobic regions created using packaging tape. Removing the channel ends allowed for complete injection of aqueous samples and the ability to quantify the concentration of sensing molecules per unit area since no reagents or sample are lost to sample loading or waste regions. Before adding sample solutions, the channels are a distinctive blue and change to a reddish-purple color upon the addition of samples containing K^+. The color transition from the region exposed to K^+ (reddish-purple) to the region where K^+ is no longer present (blue) due to consumption by the lipophilic phase is sharp and easily identified by eye. Color transitions occurred at 5.5 ± 0.5, 9.5 ± 0.4, 13.6 ± 0.5 and 18.8 ± 0.8 for 1.0, 2.5, 5.0 and 10.0 mM K^+ respectively

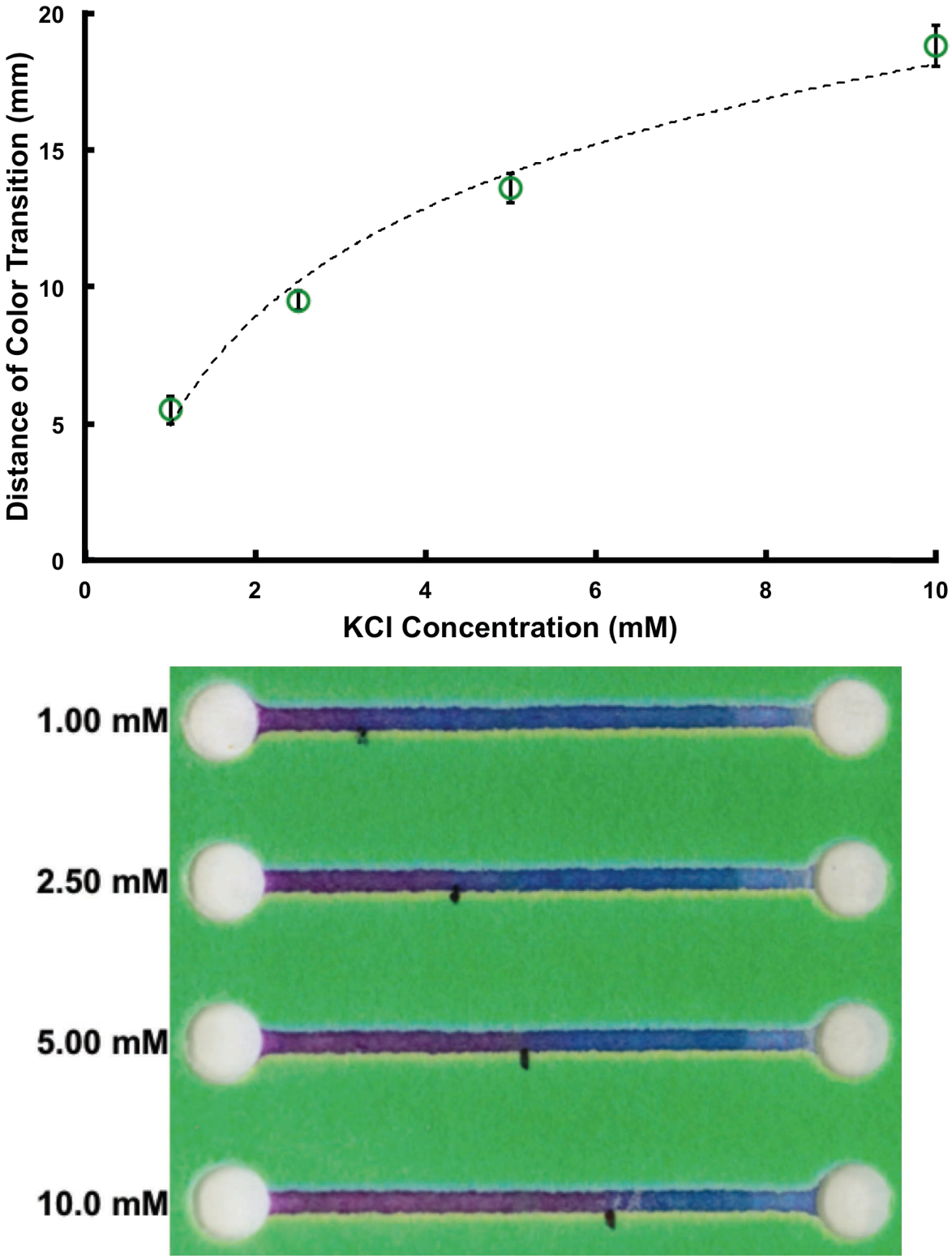

Figure 4.2. Quantification of K^+ using a distance-based μPAD. The sample K^+ concentrations analyzed were 1.00, 2.50, 5.00 and 10.0 mM. Each device was testing using 6.00 μL of aqueous sample

(RSD: 9.1, 4.2, 3.7 and 4.3%, n = 5). Even in the case of the largest standard deviations acquired for distance-based tests showed that the devices possessed the sensitivity to successfully quantify and identify 1.0 mM versus 2.5 mM K^+ in a 6.00 µL sample. Limiting the sample volume required to perform quantification tests provides a significant advantage when compared to other methods that may require larger sample volumes. It should also be noted that devices were used immediately following fabrication to acquire experimental results but devices stored in a cool dark place for 7 days did not show any additional varience.

As with most titration methods, the color transition (endpoint) that is identified by the device's user was hypothesized to occur at a distance different than the actual equivalence point. Comparison of the color transition and equivalence point were compared by collecting pixel data from one device tested with 10 mM K^+. A single line of pixels along the device was analyzed, graphed and smoothed for interpretation (Figure 4.3). Finding the equivalence point of the graph required that the maximum slope of the curve be determined by taking the second derivative of the smoothed data. A graph of the second derivative will give a major inflection point at the position of maximum slope. After the second derivative was taken, a major inflection point at 21.3 mm was found suggesting that the equivalence point exhibited by the device does indeed occur after the color transition (18.8 mm) that is used to quantify sample solutions. Although the observed color transition and true equivalence of the device do not agree, the ability of the device to quantify K^+ in aqueous sample is unaffected as long as the devices are calibrated and used consistently.

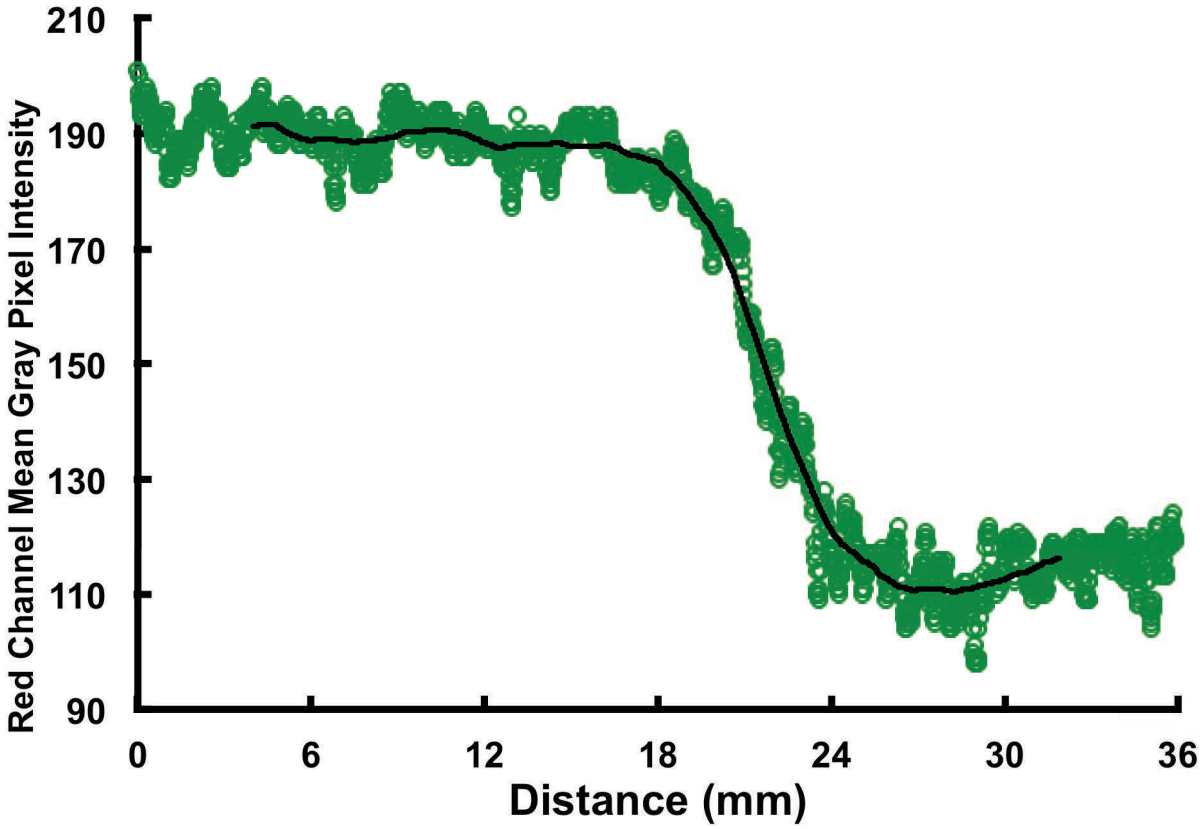

Figure 4.3. Red channel mean gray pixel intensities were collected along a straight line from a device tested with 10 mm KCl (green). Data were then smoothed using GRAMS/AI software and plotted (black). The smoothed data are representative of a titration curve that provides an equivalence point at 21.3 mm

Device Selectivity

Potassium ionophore I (valinomycin) is well studied and well known for its K^+ binding constant that is 100,000 times larger than its Na^+ binding constant.[21,22,43] The ionophore's high selectivity makes it an excellent choice for quantifying K^+ especially when dealing with aqueous samples that likely contain other ion sources. To test the colorimetric devices for K^+ selectivity 1.0, 10.0 or 100.0 mM of NaCl was added to sample solutions. Table 4.1 illustrates the differences in colorimetric responses for K^+ as a function of [Na^+]. It is clear from these results that the introduction of Na^+ does not

Table 4.1. Colorimetric quantification of K^+ in the presence of Na^+. All values are the mean gray pixel intensity for the isolated red channel

	0.1 mM K^+	1.0 mM K^+	10.0 mM K^+
0.1 mM Na^+	40.03	53.72	91.30
1.0 mM Na^+	40.60	53.34	91.74
10.0 mM Na^+	41.20	54.30	91.28
100.0 mM Na^+	41.33	54.55	91.93

affect the colorimetric results significantly. Quantification of 0.1, 1.0 and 10.0 mM K^+ is still able to be colorimetrically determined even in the presence of 100.0 mM Na^+.

Interestingly, when 100.0 mM Na^+ is present while performing distance-based experiments the color transition occurs 1.5–3.0 mm farther down the channel than when just K^+ is present. To determine if the increased distance of the color transition was a selectivity issue, LiCl and $MgCl_2$ (100.0 mM) were both added to sample solutions since potassium ionophore I is known to have inconsequential or zero binding affinity for Li^+ and Mg^{2+}.[44] Samples containing Li^+ and Mg^{2+} were found to increase the distance of the color transition by 1.5-3.0 mm like Na^+ (Figure 4.4, n = 3). Considering the increased distance of the color transition in the presence of Li^+ or Mg^{2+}, and lack of significant selectivity of potassium ionophore I for either ion, the change in the distance of the color transition due to Na^+ is believed not to be a selectivity issue but more likely the result of changes in activity coefficient and flow rate as a result of the increased ionic strength. A solution containing 10 mM KCl, and a solution containing both 10 mM KCl and 100 mM NaCl exhibit activity coefficients of 0.800 and 0.811 respectively. Increasing the ionic strength decreased the flow rate. Sample solutions containing 10 mM KCl + 100 mM

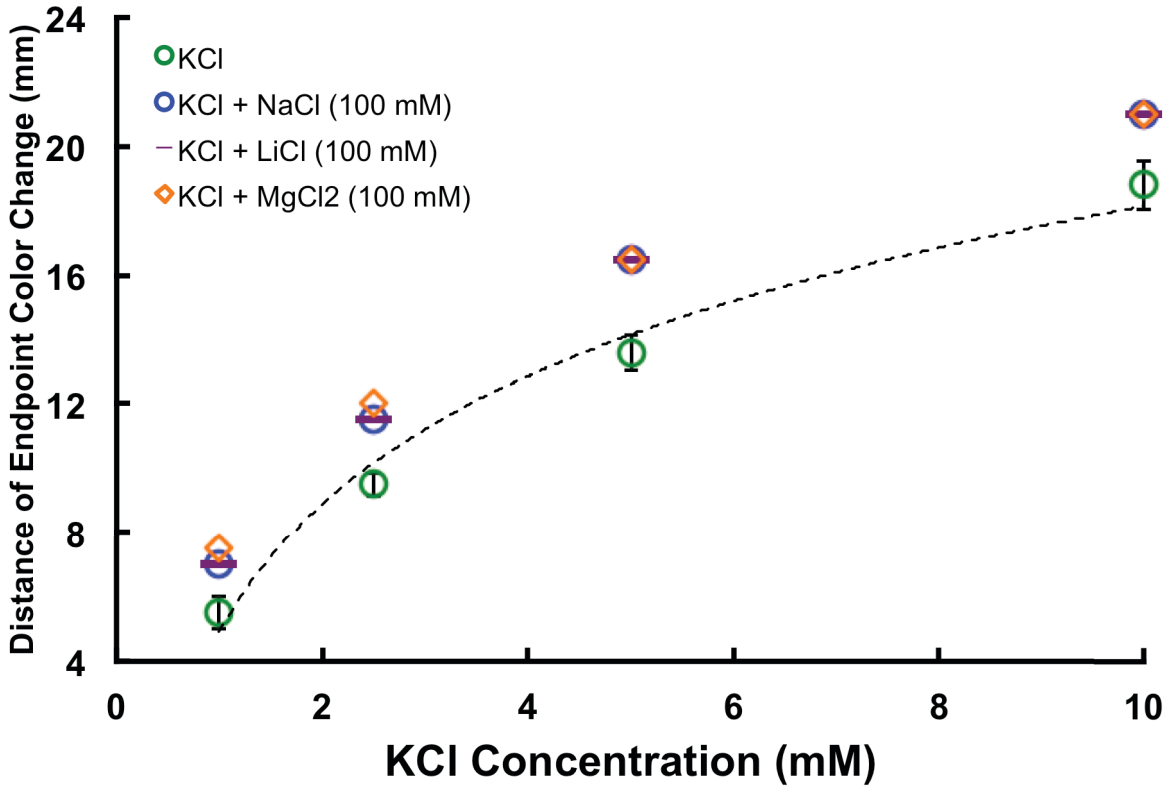

Figure 4.4. Distance-based quantification of K^+ in the presence of 100 mM Na^+, Li^+ and Mg^{2+}

NaCl required 220 ± 5 s (n = 3) to travel 20 mm while a sample solution containing only 10 mM KCl required 202 ± 2 s (n = 3) to travel the same distance. This decrease in flow rate combined with the moderate increase in activity coefficient is likely the source of the change in distance of the color transition. In μPADs a decrease in flow rate has been previously observed to correlate to an increase in signal.[45] Due to the null binding affinity of potassium ionophore I for Li^+/Mg^{2+}, it is reasonable to assume that a significant increase in signal when these species are present is due to a decrease in flow rate. The cause of the change in flow rate is still under investigation.

Distance-based devices were also tested using undiluted human control serum samples to determine the effectiveness of the distance-based μPADs at quantifying

potassium in real biological samples. Interestingly, the color change resulting from the serum samples was redder when compared to the color change of aqueous K^+ samples and made determination of the color transition relatively more difficult but still attainable. Human control serum samples containing 4.3 ± 0.5 (level 1 serum) and 6.9 ± 0.5 mM K^+ (level 2 serum) gave distance-based responses of 14.6 ± 0.9 and 16.9 ± 0.6 mm, respectively (Figure 4.5, n = 4). According to the calibration curve, the level 1 and 2

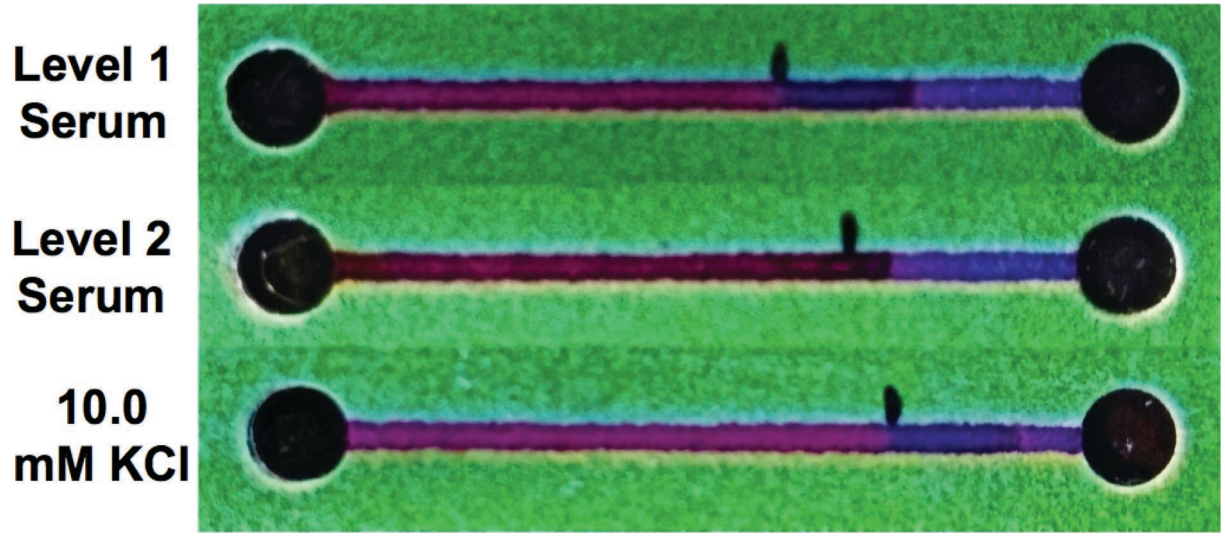

Figure 4.5. Distance-based quantification of K^+ in level 1 and 2 human serum compared to an aqueous sample containing 10.0 mM K^+

serum samples should have given responses of 13.3 and 16.0 mm. The increase in distance response was again likely due to a decrease in flow rate but this time caused by an increase is viscosity. Levels 1 and 2 serums required 320 ± 20 and 520 ± 20 s, respectively, to travel 20 mm within the μPAD channel, which is a considerable decrease in flow rate compared to values discussed above. It should also be noted that serum samples traveled a shorter total distance when compared to aqueous samples containing only K^+; this is again likely due to an increase in viscosity of the serum samples. For the level 2 serum samples the channel changed from blue to a darker red

color instead of reddish-purple making it more difficult to identify the color transition, which was likely due to the naturally occurring yellow color exhibited by that serum sample. Although the flow rate decreased dramatically, the distance-based μPAD was capable of distinguishing between 4.3 and 6.9 mM K^+ in real serum samples. An increase in the distance of the color transition due to flow rate suggests that selectivity of the organic sensing phase is retained when applied to paper-based microfluidics. Since flow rate can be accounted for during device calibration, these devices illustrate the capability of ion quantification in complex/multi analyte systems as well as in real biological samples.

pH Independence

Given that devices employed in medical diagnostics or environmental analysis operate under a wide range of conditions we tested our distance-based devices in a range of pH values. To test for pH dependency of our devices, we used 5.0 mM KCl in all sample solutions along with 10.0 mM Tris and varying quantities of HCl to adjust the pH to 6, 7 and 8 (9.9, 9.3 and 5.6 mM HCl respectively). Upon addition of sample solutions at pH 6, 7 and 8, color transitions occurred at 17.2 ± 0.3, 16.8 ± 0.3 and 15.5 ± 0.5 mm (n = 3) respectively. Color transition for the sample containing 5.0 mM KCl and no buffer occurred at 13.6 ± 0.5 mm. A shift in the distance of the color transition using samples that contain a buffer is expected due to the buffer's previously observed propensity to interfere with the CH1 sensing component.[46] Sample solutions at pH 6 and 8 provided the greatest difference at which the color transition occurred (17.2 and 15.5 mm); this 2 orders of magnitude change in $[H^+]$ still only resulted in less than a 10%

increase in the distance of color transition. Previous literature has shown that the response of CH1 is highly pH dependent but pH effects can be minimized by carrying out the measurement in an exhaustive mode, that is the analyte is completely consumed by the sensing components.[47,48] Nanospheres suspended in an aqueous solution have the capacity to perform titrations using an exhaustive mode since solutions can be continually mixed until all K^+ is consumed and equilibrium is reached. Unfortunately, the bulk sensing phase loaded on to the μPADs does not possess the surface area of the suspended nanospheres and consumption of K^+ occurs slower as sample solution flows along the channel. Due to these inherent disadvantages of μPADs it is difficult to exhaustively consume the K^+ analyte. However, a <10% shift in the distance of color transition can easily be accounted for either during the device's fabrication or in a calibration curve even if an exhaustive titration mode is not plausible. It could also be possible to increase the consumption of K^+ by reducing the flow rate within the device; using a pore filler such as sugar would reduce the rate of capillary flow and possibly shift the device towards more of an exhaustive mode.[49]

Conclusion

The ability to selectively quantify alkali/alkaline metals in aqueous solutions is critical to both human and environmental health. Unfortunately, there are currently no electronic free and portable quantification methods with the ability to measure alkali/alkaline metals. Paper-based microfluidics offer a platform to minimize equipment required to make sophisticated chemical measurements. Highly selective lipophilic ionophores located in organic nanospheres provide the capacity to colorimetrically

quantify specific alkali/alkaline metals but these methods still require that devices be digitally recorded and processed with software. μPADs utilizing distance-based methods possess portability, disposability and cost effectiveness while requiring no additional electronic equipment. Herein, we have demonstrated for the first time μPADs capable of both colorimetric and distance-based methods using a wax printed paper-based device for the quantification of alkali earth metals. Although the μPAD described herein was fabricated using a wax-printing method, the method used for depositing the sensing reagents should be compatible with all paper-based devices regardless of fabrication method. Our devices can selectively, and with minimal pH dependency, quantify K^+ ions in aqueous solutions while also being sensitive enough to distinguish between 1.0 and 2.5 mM K^+ in aqueous samples as well as 4.3 and 6.9 mM K^+ in human serum samples.

REFERENCES

1. Afridi, H. I.; Kazi, T. G.; Kazi, N.; Kandhro, G. A.; Baig, J. A.; Shah, A. Q.; Khan, S.; Kolachi, N. F.; Wadhwa, S. K.; Shah, F. *Clin. Lab.* **2010**, *57*, 559-574.

2. Buelow, M. C.; Steenwerth, K.; Parikh, S. J. *Agric. Water Manage.* **2015**, *152*, 277-285.

3. , WHO/HSE/WSH/09.01/7, Ed.; World Health Organization: WHO: Geneva, Switzerland, **2009**.

4. Fujita, Y.; Goto, S.; Ichikawa, M.; Hamaguchi, A.; Maki, K. *Arch. Oral Biol.* **2016**, *72*, 200-210.

5. Mengel, K.; Kirkby, E. A. In *Adv. Agron.*, Brady, N. C., Ed.; Academic Press, 1980, pp 59-110.

6. Shea, A. M.; Hammill, B. G.; Curtis, L. H.; Szczech, L. A.; Schulman, K. A. *J. Am. Soc. Nephrol.* **2008**, *19*, 764-770.

7. Leiba, A.; Vald, A.; Peleg, E.; Shamiss, A.; Grossman, E. *Nutrition* **2005**, *21*, 462-466.

8. Liu, B.; Du, D.; Hua, X.; Yu, X. Y.; Lin, Y. *Electroanalysis* **2014**, *26*, 1214-1223.

9. Adkins, J.; Boehle, K.; Henry, C. *Electrophoresis* **2015**, *36*, 1811-1824.

10. Yang, Y.; Noviana, E.; Nguyen, M. P.; Geiss, B. J.; Dandy, D. S.; Henry, C. S. *Anal. Chem.* **2016**, *89*, 71-91.

11. Gong, M. M.; Sinton, D. *Chem. Rev.* **2017**, *117*, 8447-8480.

12. Akyazi, T.; Basabe-Desmonts, L.; Benito-Lopez, F. *Anal. Chim. Acta* **2018**, *1001*, 1-17.

13. Cai, L.; Fang, Y.; Mo, Y.; Huang, Y.; Xu, C.; Zhang, Z.; Wang, M. *AIP Adv.* **2017**, *7*, 085214.

14. Cate, D. M.; Noblitt, S. D.; Volckens, J.; Henry, C. S. *Lab Chip* **2015**, *15*, 2808-2818.

15. Yamada, K.; Shibata, H.; Suzuki, K.; Citterio, D. *Lab Chip* **2017**, *17*, 1206-1249.

16. Sriram, G.; Bhat, M. P.; Patil, P.; Uthappa, U. T.; Jung, H.-Y.; Altalhi, T.; Kumeria, T.; Aminabhavi, T. M.; Pai, R. K.; Madhuprasad; Kurkuri, M. D. *TrAC, Trends Anal. Chem.* **2017**, *93*, 212-227.

17. Pratiwi, R.; Nguyen, M. P.; Ibrahim, S.; Yoshioka, N.; Henry, C. S.; Tjahjono, D. H. *Talanta* **2017**, *174*, 493-499.

18. Meredith, N. A.; Quinn, C.; Cate, D. M.; Reilly, T. H.; Volckens, J.; Henry, C. S. *Analyst* **2016**, *141*, 1874-1887.

19. Zhang, D.; Ma, B.; Tang, L.; Liu, H. *Anal. Chem.* **2018**, *90*, 1482-1486.

20. Jia, Y.; Dong, H.; Zheng, J.; Sun, H. *Biomicrofluidics* **2017**, *11*, 064101.

21. Kim, I.; Allen, T. W. *Proc. Natl. Acad. Sci. U. S. A.* **2011**, *108*, 17963-17968.

22. Rose, M. C.; Henkens, R. W. *Biochim. Biophys. Acta, Gen. Subj.* **1974**, *372*, 426-435.

23. Kumpf, R. A.; Dougherty, D. A. *Science* **1993**, *261*, 1708-1710.

24. Liu, C.; Hermann, T. E. *J. Biol. Chem.* **1978**, *253*, 5892-5894.

25. Chen, B.; Kwong, P.; Gupta, M. *ACS Appl. Mater. Interfaces* **2013**, *5*, 12701-12707.

26. You, I.; Yun, N.; Lee, H. *Chemphyschem* **2013**, *14*, 471-481.

27. Xie, X.; Bakker, E. *Anal. Bioanal. Chem.* **2015**, *407*, 3899-3910.

28. Rosatzin, T.; Holy, P.; Seiler, K.; Rusterholz, B.; Simon, W. *Anal. Chem.* **1992**, *64*, 2029-2035.

29. Morf, W. E.; Seiler, K.; Lehmann, B.; Behringer, C.; Hartman, K.; Simon, W. *Pure Appl. Chem.* **1989**, *61*, 1613-1618.

30. Ferris, M. S.; Katageri, A. G.; Gohring, G. M.; Cash, K. J. *Sens. Actuators, B* **2018**, *256*, 674-681.

31. Pressman, B. C. *Annu. Rev. Biochem* **1976**, *45*, 501-530.

32. Shibata, H.; Henares, T. G.; Yamada, K.; Suzuki, K.; Citterio, D. *Analyst* **2018**.

33. Wang, X.; Qin, Y.; Meyerhoff, M. E. *Chem. Commun.* **2015**, *51*, 15176-15179.

34. Lee, Y. E. K.; Kopelman, R. *Wiley Interdiscip. Rev.: Nanomed. Nanobiotechnol.* **2009**, *1*, 98-110.

35. Ruckh, T. T.; Mehta, A. A.; Dubach, J. M.; Clark, H. A. *Sci. Rep.* **2013**, *3*.

36. Pavlovic, M.; Li, L.; Dits, F.; Gu, Z.; Adok-Sipiczki, M.; Szilagyi, I. *RSC Advances* **2016**, *6*, 16159-16167.

37. Li, B.; Fu, L.; Zhang, W.; Feng, W.; Chen, L. *Electrophoresis* **2014**, *35*, 1152-1159.

38. Morbioli, G. G.; Mazzu-Nascimento, T.; Stockton, A. M.; Carrilho, E. *Anal. Chim. Acta* **2017**, *970*, 1-22.

39. Nilghaz, A.; Zhang, L.; Shen, W. *Chem. Eng. Sci.* **2015**, *129*, 34-41.

40. Martinez, A. W.; Phillips, S. T.; Carrilho, E.; Thomas, S. W.; Sindi, H.; Whitesides, G. M. *Anal. Chem.* **2008**, *80*, 3699-3707.

41. Lopez-Ruiz, N.; Curto, V. F.; Erenas, M. M.; Benito-Lopez, F.; Diamond, D.; Palma, A. J.; Capitan-Vallvey, L. F. *Anal. Chem.* **2014**, *86*, 9554-9562.

42. Sicard, C.; Glen, C.; Aubie, B.; Wallace, D.; Jahanshahi-Anbuhi, S.; Pennings, K.; Daigger, G. T.; Pelton, R.; Brennan, J. D.; Filipe, C. D. *Water Res.* **2015**, *70*, 360-369.

43. Varma, S.; Sabo, D.; Rempe, S. B. *J. Mol. Biol.* **2008**, *376*, 13-22.

44. Štěpánová, S.; Kašička, V. *Methods Mol. Biol.* **2016**, 219-232.

45. Nguyen, M. P.; Meredith, N. A.; Kelly, S. P.; Henry, C. S. *Anal. Chim. Acta* **2018**.

46. Wang, L.; Xie, X.; Zhai, J.; Bakker, E. *Chem. Commun.* **2016**, *52*, 14254-14257.

47. Xie, X.; Zhai, J.; Bakker, E. *Anal. Chem.* **2014**, *86*, 2853-2856.

48. Xie, X.; Zhai, J.; Crespo, G. A.; Bakker, E. *Anal. Chem.* **2014**, *86*, 8770-8775.

49. Lutz, B.; Liang, T.; Fu, E.; Ramachandran, S.; Kauffman, P.; Yager, P. *Lab Chip* **2013**, *13*, 2840-2847.

CHAPTER 5. CONCLUSION

As the global population continues to grow and resources continue to be consumed, there is an increased demand for the ability to rapidly assess environmental systems using robust, inexpensive, and portable analytical tools. These tools are sought by all kinds of groups: from industrial entities that want to accurately develop more efficient processes, to people in living resource limited regions that desire the ability to inexpensively assess their environment to prevent exposure and improve crop yields. Due to recent technological advances and fulfillment of the aforementioned criteria, many researchers have suggested the use of microfluidics to fulfill this growing need. Throughout my graduate career I have utilized microfluidics as an analytical tool in a variety ways that pertain to the environment. Within this dissertation I have discussed 1) the usage of traditional polymeric microfluidic devices to study fundamental properties of surface chemistry 2) the design and fabrication of a microfluidic device to study fluid dynamics within convoluted media and 3) the development of a microfluidic paper-based analytical device (μPAD) to selectively quantify K^+ in complex samples.

During my first project, we used the current monitoring method paired with a traditional polymeric microfluidic device to observe relative changes to zeta potential.[1] This was done to dynamically investigate the hypothesized cation bridging phenomenon that was suggested by the existing literature to be the limiting factor for the efficiency at which oil recover could occur.[2,3] Beyond oil recovery, the impacts of cation bridging can also be understood as a contributing factor for surfactant surface fouling.[4,5] Cation bridging involves the interaction of a negatively charged surface with a like-charged

surfactant species that is facilitated by divalent metal ions. Specifically, researchers found that systems containing Ca^{2+} reproducibly increased adsorption of surfactants to like-charged surfaces.[3,6] While the effect of cation bridging had been previously observed by other researchers, the actual mechanism by which Ca^{2+} facilitates surfactant adsorption was not entirely understood due to the lack of time resolved binding studies. By using the current monitoring method paired with microfluidics we were able to observe relative changes to the surface binding environment as a function of time. When performing our experiments we found that adsorption of negatively charged 2-napthoate to a negatively charged surface increased as the concentration of Ca^{2+} increased. Interestingly, we also observed that increasing system Ca^{2+} caused equilibration time of surfactant adsorption to increase. Another experiment alluded to the effects of metal ion charge density. When two metal ions of the same formal charge (K^+/Na^+ or Ca^{2+}/Mg^{2+}) were introduced, the metal ion with the greatest charge density caused a greatest change to the surface charge. These observations provide important time-resolved evidence for the cation bridging effect and contribute to the scientific community's understanding of this phenomenon. Future research pertaining to cation bridging must investigate how divalent metal ions' charge density contributes to the adsorption of surfactants. Other topics pertaining to the structure of the surfactant (conjugation, functionalization, hydrophobicity, etc.) could provide further insight into cation bridging. Combination of the methods we used with surface selective sum frequency generation (SFG) spectroscopy could also provide information on the orientation of adsorbed surfactant molecules in the presence and absence of divalent metal ions.

My next project involved the design and fabrication of a microfluidic device to model fluid interactions within an oil reservoir. During the oil recovery process the natural pressure of an oil reservoir is initially used to recover oil. As that pressure diminishes aqueous fluids must be pumped into the reservoir to displace/recover additional oil, this process is called “core flooding”.[7,8] Development of more efficient core flooding strategies will allow oil recovery to continue in mature reservoirs where infrastructure is already in place, which minimizes further environmental impact.[9] Current large-scale methods for testing core flooding strategies are expensive and can take years to acquire experimental results.[10,11] In an effort to reduce operational cost and experimental times, small-scale methods taking place in a laboratory setting have also been used to model core flooding.[12] However, these methods utilize large reservoir rock core samples that are expensive, require long equilibration times, and require specialized instrumentation for flow imaging due to the opaque nature of the rock cores.[13,14] To avoid the disadvantages of both large and small-scale core flooding methods researchers have proposed using specifically designed and commercially available microfluidic devices to carry out core flooding experiments. Unfortunately these devices have their own disadvantages: the accuracy at which they replicate the chemical and physical properties of the reservoir rock.[15-17] To improve on the micromodels available, we developed the polymeric-based microfluidic Flow On Rock Device (FORD) that incorporated thin slices of real reservoir rock core samples. By incorporating reservoir rock samples directly into the device we avoided the need to physically recreate the reservoir rock sample’s physical characteristics. Furthermore, the chemical properties of the reservoir rock sample are inherently present within the

sample and do not need to be simulated during core flooding experiments. While using the FORD we observed predictable fluid-fluid interactions and variation in the quantity of unrecoverable oil when controlling the initial wetting conditions of the rock sample. When samples of different morphologies (sandstone vs. shale) were used, the physical variance of the reservoir rock samples was also observed. The FORD is important to oil recovery research because it is a chemically and physically representative device that is inexpensive, does not require specialized instrumentation, and can be used to rapidly test different oil recovery strategies designed for specific reservoirs.

Lastly, my third project involved the creation of a μPAD capable of quantifying K^+ in aqueous samples. Human and crop health are both effected by alkali and alkaline earth metals found in the environment.[18-20] Typically, electrochemical methodologies are used to quantify these metals.[21-23] While effective, these methods require the use of an electrical power source that increases their cost and complexity, reduces their portability and limits experimental quantification to laboratory settings. If experimental quantification of alkali/ne earth metals is to occur outside of the laboratory, then portable power-free analytical tools must be developed. Colorimetric μPADs have been suggested for portable field quantification due to their capacity to store experimental sensing reagents and ability to process aqueous sample volumes without the need for external pumps. Until the research described in this dissertation, there has not been an power-free μPAD available to selectively and quantitatively measure alkali/ne earth metals.[24] The lack of μPADs to quantify these metals is largely due to the absence of corresponding aqueous soluble colorimetric sensing reagents. Recently, researchers have found that the lipophilicity of sensing reagents can be circumvented by the use of

spherical lipophilic reaction vessels called “optode nanosensors” that are suspended in aqueous solutions.[25] To create colorimetric μPADs capable of detecting K^+ we deposited K^+ sensing optodes on a filter paper substrate. By using optodes paired with colorimetric μPAD spot tests we found that we were able to increase the sensitivity and quantifiable range of K^+ exhibited by existing devices. Additionally, and were also able to develop the first μPAD capable of quantitatively assessing the concentration of K^+ using a distance-based analysis mode. This distance-based μPAD was observed to be highly selective and capable of differentiating between 4.3 and 6.9 mM K^+ in real undiluted human serum. Successful analysis using complex human serum alludes to the high selectivity and sensitivity of the distance-based μPAD and suggests that this device would also be appropriate for analyzing highly complex environmental samples. The development of this μPAD technology provides a foundation for new inexpensive, selective, and portable devices to quantify alkali/ne earth metals in environmental and biological samples. Multiplexed μPADs capable of simultaneously quantifying multiple alkali/ne earth metal analytes are now possible due to the highly selective nature of optode nanosensors. Optodes can also be used to create “elimination zones” within μPADs to selectively remove interfering ions that would otherwise hinder a specific assay. Optimized variations of this distance-based device could also be used as a point-of-care analytical tool to assess human health.

REFERENCES

1. Gerold, C. T.; Henry, C. S. *Langmuir* **2018**, *34*, 1550-1556.

2. Lager, A.; Webb, K. J.; Collins, I. R. *Soc. Pet. Eng. J.* **2008**.

3. Austad, T.; Rezaeidoust, A.; Puntervold, T.; *Soc. Pet. Eng. J.*, 2010.

4. Boussu, K.; Kindts, C.; Vandecasteele, C.; Van der Bruggen, B. *Chemphyschem* **2007**, *8*, 1836-1845.

5. Yu, S.; Zhang, X.; Li, F.; Zhao, X. *Colloids and Surfaces A.* **2017**, *518*, 130-138.

6. Wang, X.; Lee, S. Y.; Miller, K.; Welbourn, R.; Stocker, I.; Clarke, S.; Casford, M.; Gutfreund, P.; Skoda, M. W. *Langmuir.* **2013**, *29*, 5520.

7. Alvarado, V.; Manrique, E. *Energies* **2010**, *3*, 1529–1575.

8. Ali, S. M. F.; Thomas, S. *J. Can. Pet. Technol.* **2000**, *39*, 7–11.

9. Zekri, A. Y.; Jerbi, K. K.; El-Honi, M.; Society of Petroleum Engineers.

10. McGuire, P. L.; Chatham, J. R.; Paskvan, F. K.; Sommer, D. M.; Carini, F. H. *Soc. Pet. Eng. J.* **2005**.

11. Sevin, J.; Capron, B. *Energy Perspectives* **2013**.

12. Rivet, S. M.; Lake, L. W. *Soc. Pet. Eng. J.* **2010**.

13. Li, M.; Xiao, D.; Shakerian, M.; Afrough, A.; Goora, F.; Marica, F.; Romero-Zerón, L.; Balcom, B. In *The proceedings of the 32st International Symposium of the Society of Core Analysts, Snowmass, Colorado, 21–26 August 2016*, 2016, pp 1-12.

14. Ramskill, N. P.; Bush, I.; Sederman, A. J.; Mantle, M. D.; Benning, M.; Anger, B.; Appel, M.; Gladden, L. F. *J. Magn. Reson.* **2016**, *270*, 187-197.

15. Gunda, N. S.; Bera, B.; Karadimitriou, N. K.; Mitra, S. K.; Hassanizadeh, S. M. *Lab Chip* **2011**, *11*, 3785–3792.

16. Song, W.; Kovscek, A. R. *Lab Chip* **2015**, *15*, 3314-3325.

17. Lee, H.; Lee, S. G.; Doyle, P. S. *Lab Chip* **2015**, *15*, 3047–3055.

18. Afridi, H. I.; Kazi, T. G.; Kazi, N.; Jamali, M. K.; Arain, M. B.; Jalbani, N.; Sarfaraz, R. A.; Shah, A.; Kandhro, G. A.; Shah, A. Q. *Biol. Trace Elem. Res.* **2008**, *124*, 206.

19. Afridi, H. I.; Kazi, T. G.; Kazi, N.; Kandhro, G. A.; Baig, J. A.; Shah, A. Q.; Khan, S.; Kolachi, N. F.; Wadhwa, S. K.; Shah, F. *Clin. Lab.* **2010**, *57*, 559-574.

20. Buelow, M. C.; Steenwerth, K.; Parikh, S. J. *Agric. Water Manage.* **2015**, *152*, 277-285.

21. Sameenoi, Y.; Mensack, M. M.; Boonsong, K.; Ewing, R.; Dungchai, W.; Chailapakul, O.; Cropek, D. M.; Henry, C. S. *Analyst* **2011**, *136*, 3177-3184.

22. Kappes, T.; Hauser, P. C. *Anal. Chem.* **1998**, *70*, 2487-2492.

23. Gupta, V. K.; Ganjali, M.; Norouzi, P.; Khani, H.; Nayak, A.; Agarwal, S. *Crit. Rev. Anal. Chem.* **2011**, *41*, 282-313.

24. Gerold, C. T.; Bakker, E.; Henry, C. S. *Anal. Chem.* **2018**.

25. Xie, X.; Bakker, E. *Anal. Bioanal. Chem.* **2015**, *407*, 3899-3910.

APPENDIX 1. QUANTIFICATION OF ENVIRONMENTAL PHOSPHATE USING MICROFLUIDIC PAPER-BASED ANALYTICAL DEVICES

In this appendix, the quantification of environmental phosphate using microfluidic paper-based analytical devices (μPADs) will be discussed. The objective of the following discussion is to provide a foundation for future research using the author's preliminary experimental observations combined with recent advances found in the literature to ultimately create an integrated sensor for phosphate and potassium. Complications and challenges performing phosphate quantification will be presented. It should be mentioned that Mr. Kieran Simske (SBME undergrad) helped with development of the diameter-based phosphate quantification and that his efforts were greatly appreciated.

Overview

Phosphate contributes significantly to plant biological processes and is associated with agricultural crop health and yield. Plants acquire phosphate by absorbing the essential nutrient from soil and water through roots.[1,2] All kinds of living organisms require phosphate to perform crucial biological processes including oxidative phosphorylation that forms adenosine triphosphate (ATP), which is used to transport cellular energy.[3] In plants failed formation of ATP causes reduced seasonal yields and undesirable effects on reproductive health.[3] Although its presence is essential, excessive biological phosphate concentrations can result in well documented phosphate toxicity that causes cellular damage and health complications.[4,5] In general, plant species are more likely to experience insufficient phosphate concentrations than

toxicity. Low phosphate concentrations in plants can occur when soil/water sources are depleted and/or when not enough phosphate is applied to agricultural soil/water via fertilizer. Since inappropriate phosphate concentrations can lead to biological complications in agricultural plants, quantification of environmental phosphate is critical for optimizing the crop health.

Phosphate is typically quantified using methods requiring bulky and expensive instrumentation that includes: 1 and 2D Nuclear Magnetic Resonance, Infrared and Raman Spectroscopy, Quadrupole-Time of Flight MS/MS, High Resolution-MS, Nanoscale Secondary Ion Mass Spectrometry, X-ray Fluorescence, X-ray Photoelectron Spectroscopy, X-ray Absorption Spectroscopy, and Ultraviolet–visible spectroscopy, the later of which is the most common.[6] While these methods are effective, they are not portable and limit quantification to a laboratory setting. Unfortunately, this lack of portability prevents people living in resource limited regions from assessing the phosphate content found in their agricultural soil/water. In an attempt to provide disadvantaged peoples with the capacity to quantify phosphate, highly portable microfluidic paper-based analytical devices (μPADs) have been suggested as an alternative to typical instrumentation.

To quantify phosphate using colorimetric μPAD spot tests, researchers have relied on a colorimetric reaction that forms a blue-colored phosphoantimonyl-molybdenum complex (PMB). Under acidic conditions, the reaction of uncolored potassium antimony (III) - tartrate hydrate, ammonium molybdate tetrahydrate, and orthophosphate first produce an intermediate antimony-phosphomolybdate complex. Reduction of this intermediate complex results in blue-colored PMB.[6] Unfortunately, the

potassium antimony (III) - tartrate hydrate and ammonium molybdate tetrahydrate species will undergo reaction in a sufficiently acidic environment even in the absence of phosphate. To help avoid premature reactivity and implement this chemistry in μPADS, Jayawardane et al. proposed separation of the inorganic reaction species from the reducing component using multiple layers within their device that was shown to be effective for quantifying 0.2–10.0 ppm phosphate in water samples.[7,8] Using Jayawardane et al.'s research as a starting point, we attempted to widen the range of quantifiable sample phosphate concentrations and improve the device's stability.

Experimental

Potassium antimony (III) - tartrate hydrate was acquired from Alfa Aesar (Ward Hill, MA). Ammonium molybdate tetrahydrate was acquired from Fisher Scientific (Fair Lawn, NJ). p-toluenesulfonic acid was acquired from Sigma-Aldrich (St. Louis, MO). Ascorbic acid was acquired from Mallinckrodt Baker Inc. (Paris, KY). Potassium Phosphate was acquired from EMD Chemicals Inc. (Gibbstown, NJ). All chemical species were acquired from their respective manufacturer and used without further purification. Aqueous solutions were prepared in 18.2 MΩ*cm water from a Millipore Milli-Q® purification system (Millipore, Billerica, MA). Whatman™ No. 4 qualitative-grade filter paper was purchased from GE Healthcare UK Limited (Buckinghamshire, UK). CorelDraw® software was used to design the hydrophobic wax barrier for all fabricated devices. Hydrophobic wax barriers were printed on filter paper using a commercial wax printer (Xerox Colorqube® 8870). Devices were sealed using hot lamination pouches (0.3 mm thick) from 3M® (St. Paul, MN). Photographs for

colorimetric analysis were taken using a Motorola Z Play cellphone. ImageJ software (National Institutes of Health) was used for image analysis.

To fabricate the μPAD, pieces of Whatman™ No. 4 filter paper containing a wax printed design were placed design side down on a 150 ˚C hotplate for 90 s. A single 4” x 5” x 1/8” piece of aluminum was placed on top of the filter paper to ensure the paper kept conformal contact with the hotplate. After the paper was removed from the hotplate and allowed to cool to room temperature (~1 min), reagents were added to two separate layers of paper. 10 μL of an acidic reagent solution containing 2.0 M p-toluenesulfonic acid and 11.4 mM ascorbic acid was added to one paper layer and 10 μL of an inorganic reagent solution containing 0.6 mM potassium antimony (III) - tartrate hydrate and 0.1 M ammonium molybdate tetrahydrate (solution was saturated with the molybdate species) was added to the other layer of the device. Layers of the device were allowed to dry under flowing compressed air (~8 psi) for ~5 minutes before being used. While the paper layers dried, 8 mm holes were punched in one side of the hot lamination pouches to act as a sample inlet; this was accomplished using a disposable biopsy punch. Once the device layers were dried and the lamination pouches were prepared, the two device layers were stacked and aligned under the 8 mm holes in a hot lamination pouch, which was then all inserted into a hot laminator at 350 ˚C and cut to size (Figure A1.1). Diameter-based devices were prepared using the same methodology except that inorganic solutions were deposited in analysis regions by briefly submerging the layer of paper in the stock “inorganic solution.”

To use the μPAD and acquire experimental results, 50 μL of sample solution was added to the sample inlet. The sample solution remained on the device for 4 min to

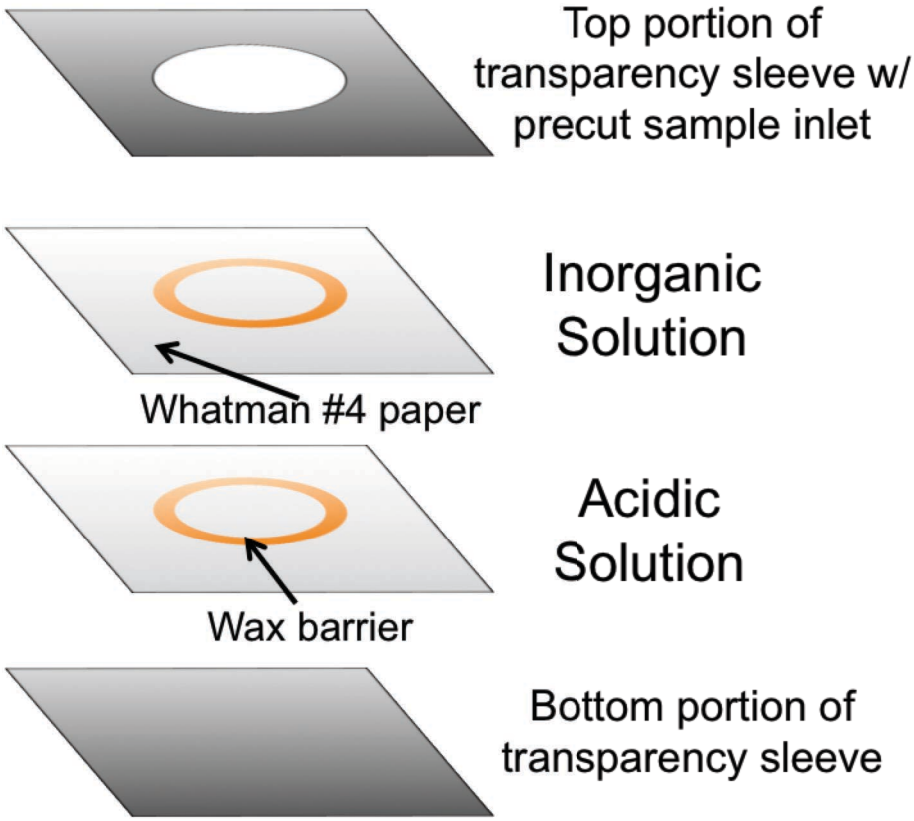

Figure A1.1. Assembly of the layers for the colorimetric phosphate μPAD. The inorganic solution contains 0.6 mM potassium antimony (III) - tartrate hydrate and 0.1 M ammonium molybdate tetrahydrate. The acidic solutions contains 2.0 M p-toluenesulfonic acid and 11.4 mM ascorbic acid

observe the colorless to blue color change. After 4 min of reaction time, excess sample was removed by gently blotting the sample inlet with an absorbent tissue. A smart phone was then used to take a photo of the front face of the device. The camera was positioned ~10 cm directly above the device while glare was kept to a minimum (no flash was used). Images were then processed using ImageJ software by isolating the blue color channel and determining the mean gray pixel intensity within the experimental spot region. Mean gray pixel intensities were collected then imported into Excel (Microsoft) to calculate calibration curves and experimental standard deviations.

Results and Observations

Effective Concentration Range

We were able to replicate and improve on colorimetric spot test results originally obtained by Jayawardane et al.[7] Since many people living in resource limited regions need to know if their crops are receiving adequate phosphate concentrations, the initial objective of this project was to create a colorimetric μPAD capable of quantifying a wider range of sample phosphate concentrations than the existing devices. The device put forth by Jayawardane et al. was shown to be effective for 0.2–10 ppm but our device was effective for 1–1000 ppm (Figure A1.2). We were able to widen the effective range

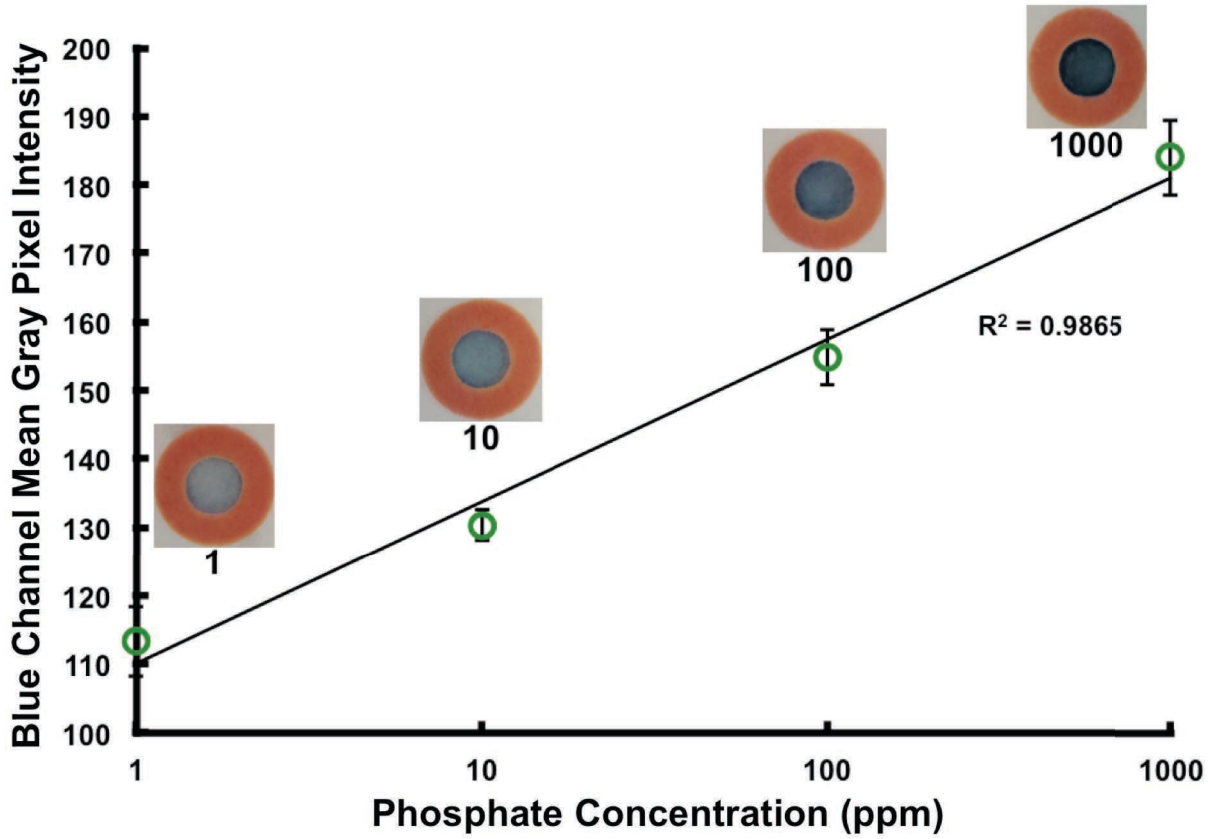

Figure A1.2. A calibration curve accompanied by correlating experimental spot tests for sample solutions containing 1–1000 ppm phosphate

by simply depositing ~20 times more reagent in detection zones when compared to Jarawardane et al. It should be noted that our detection zones were 8 mm in diameter while Jayawardane used 3 mm diameter detection zones. Despite increasing the surface area of our detection zones, the concentration of reagent species per unit area was still a relative increase when compared to the previous paper.

Stability

Stability of these devices is also a concern due to the reactivity of the reagents in an acidic environment and their ability to be readily reduced. Jayawardane et al. partially increased their device's stability by separating their reducing agent (ascorbic acid) from the rest of the reagents (antimony/molybdate species). However, they ended up sacrificing their device's stability while trying to increase the solubility of ammonium molybdate tetrahydrate by dissolving both inorganic species in sulfuric acid before deposition. As previously mentioned, the antimony and molybdate species will undergo premature reactivity in the presence of a sufficiently acidic environment. To increase stability in our device we used 18.2 MΩ*cm water (no additional acidic or basic component) to make the inorganic solution that was used to fabricate the device. However, a sufficiently acidic environment is still required for the desired reaction to occur so we added our chosen acid component (p-toluenesulfonic acid) to the solution containing the reducing agent (ascorbic acid). This new "acidic solution" was deposited on one layer of the device while the "inorganic solution" was added to a separate layer (Figure A1.1). Our preliminary test results showed that the colorimetric phosphate tests were stable for 14 days but the time at which the devices are no longer effective was

not thoroughly investigated. Jayawardane et al.'s initial device was shown to be stable for 48 hours but that could be extended to up to 20 days if entire device was sealed and not open to environmental air. They found that sealing their device prevented oxidation of the reducing agent (ascorbic acid), which was why their unsealed device was only stable for 48 hours. An easy way to prevent ascorbic acid's oxidation without having to seal the device is by lowering the pH of its surroundings.[7] By combining our acidic component (p-toluenesulfonic acid, used to decrease toxicity) and reducing agent (ascorbic acid) we were able to 1.) prevent premature reactivity of the inorganic species and 2.) prevent the oxidation of ascorbic acid. Jayawardane et al.'s completely sealed device does express stability up to 20 days, a sample inlet needs to be punched before being able to use the device; this decreases design simplicity and requires the device's user to provide means of opening the device.

Diameter-Based µPAD

In an attempt to design a µPAD capable of more quantitative phosphate analysis, a diameter-based µPAD was investigated (Figure A1.3). It is worth mentioning that the possibility of using diameter-based devices was not thoroughly explored but the initial experimental results that were obtained are discussed below. Colorimetric diameter-based quantification in µPADs relies on outward radial flow of aqueous samples and the resulting colorimetric color change between sensing components and the analyte. Sample solutions flow outward from the injection site positioned in the center of the device and, much like in colorimetric methods, a color change occurs when sensing components chemically react with the analyte. Sample solutions continue to flow

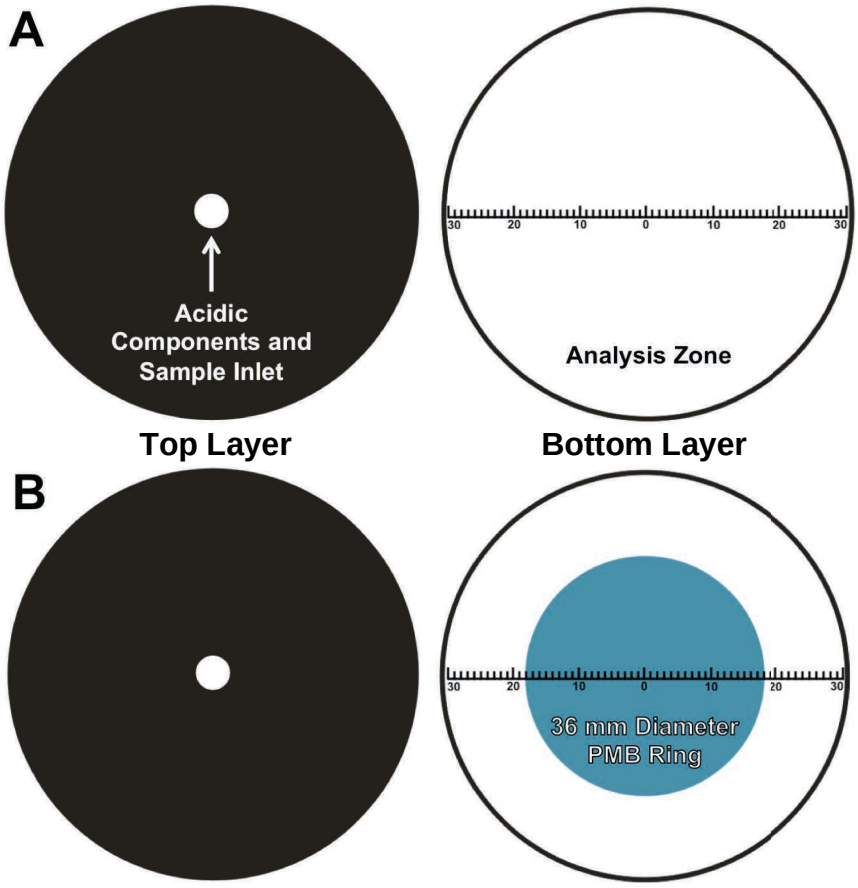

Figure A1.3. Acidic components of the phosphate test are deposited in the small inner region of the large black ring and the inorganic species are deposited in the "Analysis Zone." No color change will be observed before the sample solution is added. **B.)** Following the addition of a sample solution, a blue PMB ring appears in the "Analysis Zone." The diameter of the PMB ring is measured by determining the numbers located at the edge of the ring. The diameter of the simulated ring in 3.B would be determined to be 36 mm

outward, even after all the analyte has been consumed, but there will be no additional color change. Instead of analyzing the intensity of the color change, diameter-based devices are analyzed through measurement of the diameter of the colored ring, which is then correlated to specific analyte concentrations. It should be noted that the top layer of the device is designed to be a large black wax "donut," which prevents the sample solution from laterally wicking anywhere besides the analysis zone in the bottom layer.

When diameter-based devices were tested there did not appear to be an observable difference in the blue-colored PMB ring that formed. However, after the devices were completely dried (~8 hrs) a purple-colored ring was observed (Figure A1.4). Although this purple-colored ring was difficult to observe, it did express

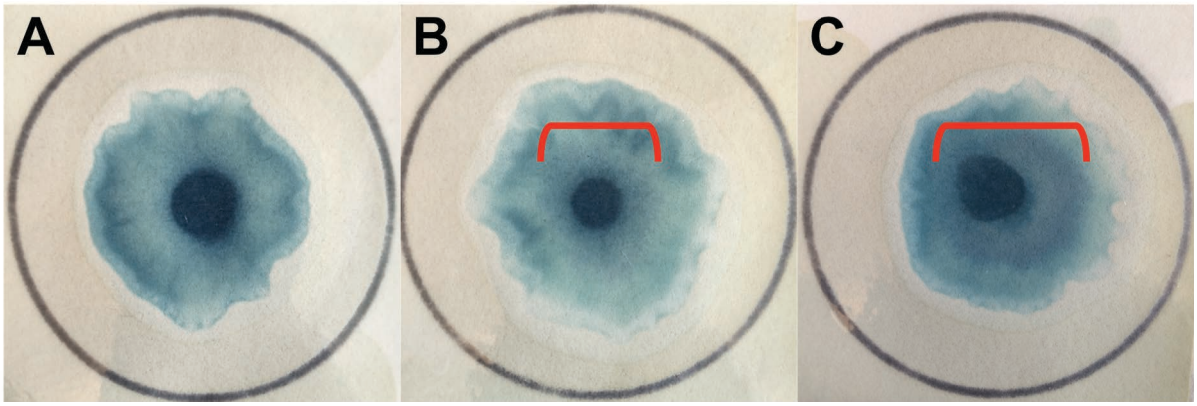

Figure A1.4. Diameter-based experimental results using aqueous samples containing 10, 100, and 1000 ppm phosphate (A, B, and C respectively). Devices were allowed to completely dry before images were taken. The red bracket found in B and C depict the width of a purple-colored ring that appears to increase in width as sample phosphate concentration increases

an increase in diameter as the sample phosphate concentration increased. It is possible that the purple-colored ring took 8 hrs to form or that it was just not observable until the device had completely dried due to the color contrast of the wetted paper substrate. If future research does indicate that the purple-colored ring can be used to quantitatively measure sample phosphate concentrations, changes to the device that could give a more pronounced ring should be investigated. Broadly, a more stark appearance of this ring could be obtained by modifying the specific quantities of each inorganic species or control of the acid/reducing agent components concentration. Due to the complexity of the PMB reaction, the purple ring could be the product of a side reaction or a species that underwent further reduction as the device sat for prolonged times. Due to the lack of experimental observations using the diameter-based device it is difficult to draw

specific conclusions; however, the appearance of a colored ring that changes with analyte concentration could be exploited in future research to develop a more quantitative method for measure phosphate in μPADs.

Future Directions

Since we were able to simply increase the effective analyte detection range of the colorimetric test by increasing the reagent concentration, attempts to further modify the range should start with this aspect. If the naked-eye method is to be used instead of digitally processing experimental results, an increase to the test spots' diameters might be considered to facilitate qualitative analysis. Changes to the diameter of the colorimetric detection zone can be easily made but the reagent to area ratio must be controlled for the device to remain effective; furthermore, this ratio should be optimized to create the most effective μPAD. Stability of devices can be improved by depositing the inorganics species in a neutral environment and by investigating the possible usage of alternative acidic components. Future attempts at developing a phosphate detecting μPAD should be made by combining the acidic component with the reducing agent even if ascorbic acid is not used. By combining these two components, the probability of premature reactivity occurring is reduced while oxidation of the reducing agent is minimized. The minimum quantity of the acidic component required to cause desirable reactivity should also be determined since minimizing the concentration of acid in the device reduces the device's toxicity/corrosiveness. If more quantitative analysis is desired, diameter-based methods should continue to be developed possibly by increasing the observable color of the purple-colored ring.

Conclusion

Improvement to the colorimetric detection of phosphate on μPADs must be made so that disadvantaged people around that globe can assess their agricultural soil/water, which could lead to more successful crops. Herein, improvements to existing colorimetric μPAD methods capable of phosphate quantification have been made. Eliminating acidic components from layers of the device where inorganic species were deposited increased stability. Storing the acidic component with the reducing agent (ascorbic acid) prevented oxidation of the ascorbic acid caused by atmospheric air. Diameter-based methods, while not heavily developed so far, offer the potential to be more quantitative than their purely colorimetric counterparts without the need for digital image processing.

REFERENCES

1. Lopez-Arredondo, D. L.; Leyva-González, M. A.; González-Morales, S. I.; López-Bucio, J.; Herrera-Estrella, L. *Annu. Rev. Plant Biol.* **2014**, *65*, 95-123.

2. Smith, F. W.; Mudge, S. R.; Rae, A. L.; Glassop, D. *Plant Soil* **2003**, *248*, 71-83.

3. Razzaque, M. S. *Clin. Sci.* **2011**, *120*, 91-97.

4. Ozanne, P.; Shaw, T. *Aust. J. Agric. Res.* **1967**, *18*, 601-612.

5. Jones Jr, J. B. *Commun. Soil Sci. Plant Anal.* **1998**, *29*, 1779-1784.

6. Kruse, J.; Abraham, M.; Amelung, W.; Baum, C.; Bol, R.; Kühn, O.; Lewandowski, H.; Niederberger, J.; Oelmann, Y.; Rüger, C. *J. Plant Nutr. Soil Sci.* **2015**, *178*, 43-88.

7. Jayawardane, B. M.; McKelvie, I. D.; Kolev, S. D. *Talanta* **2012**, *100*, 454-460.

8. Crouch, S. R.; Malmstadt, H. V. *Anal. Chem.* **1967**, *39*, 1084-1089.